PH.D. DISSERTATION / TESIS DOCTORAL

DEVELOPMENT OF A SKY IMAGER FOR CLOUD CLASSIFICATION AND AEROSOL CHARACTERIZATION

DESARROLLO DE UN SISTEMA DE CÁMARA DE CIELO PARA LA CLASIFICACIÓN DE NUBES Y LA CARACTERIZACIÓN DEL AEROSOL

ALBERTO CAZORLA CABRERA

Universidad
de
Granada

Centro Andaluz
de
Medio Ambiente

Grupo Física
de la
Atmósfera

Editor: Editorial de la Universidad de Granada
Autor: Alberto Cazorla Cabrera
D.L.: GR 3084-2010
ISBN: 978-84-693-3307-5

UNIVERSIDAD DE GRANADA

DEPARTAMENTO DE FÍSICA APLICADA

GRUPO DE FÍSICA DE LA ATMÓSFERA

PH.D. DISSERTATION / TESIS DOCTORAL

DEVELOPMENT OF A SKY IMAGER FOR CLOUD CLASSIFICATION AND AEROSOL CHARACTERIZATION

DESARROLLO DE UN SISTEMA DE CÁMARA DE CIELO PARA LA CLASIFICACIÓN DE NUBES Y LA CARACTERIZACIÓN DEL AEROSOL

Tesis presentada por Alberto Cazorla Cabrera para optar al grado de Doctor.

Directores de la Tesis:

Dr. Francisco José Olmo Reyes
Catedrático de la Universidad de Granada
Departamento de Física Aplicada
Universidad de Granada

Dr. Lucas Alados Arboledas
Catedrático de la Universidad de Granada
Departamento de Física Aplicada
Universidad de Granada

Granada, Mayo de 2010

El trabajo de investigación que se expone en la presente memoria, titulada: *Development of a Sky Imager for Cloud Classification and Aerosol Characterization (Desarrollo de un Sistema de Cámara de Cielo para la Clasificación de Nubes y la Caracterización del Aerosol)*, que para aspirar al grado de Doctor en Física presenta Alberto Cazorla Cabrera, ha sido realizado en la Universidad de Granada gracias a la beca concedida por la Junta de Andalucía (Consejería de Innovación, Ciencia y Empresa) "Formación de doctores en centros de investigación y universidades andaluzas (convocatoria 2004)", bajo la dirección de:

VºBº

Los Directores:

Dr. FRANCISCO JOSÉ OLMO REYES

Dr. LUCAS ALADOS ARBOLEDAS

El aspirante a grado de Doctor:

ALBERTO CAZORLA CABRERA

Agradecimientos

Han pasado ya seis años y muchas han sido las personas que me han acompañando en esta etapa del camino. A todas ellas, las que mencione y las que quizá olvide, va mi agradecimiento.

En primer lugar quiero expresar mi más sincero agradecimiento a mis directores de tesis, el catedrático Franciso José Olmo Reyes y el catedrático Lucas Alados Arboledas, por su dedicación, apoyo y experiencia que ha hecho posible la realización de este trabajo. Mucho ha sido el trabajo conjunto que ha hecho posible que llegue este día, pero también hubo momentos fuera del ámbito profesional que hemos compartido y que los convierten en algo más que en mis directores.

También son muchas las personas que han pasado por el Grupo de Física de la Atmósfera que me han acompañado en todo o parte del camino. Gracias a Ana Isabel, Antonio Alcántara, Antonio Valenzuela, Enrique, Hassan, Inma Alados, Inma Foyo, Juan Alfredo, Juan Antonio, Juan Luis y Penélope. Mención especial tiene Andy, por sus correcciones desinteresadas en mis primeros años y su interés en mi carrera a lo largo de todo este tiempo. No me he olvidado de aquellos con los que he pasado más tiempo también fuera del CEAMA: Borja, Dani y Fran, que los convierte en mucho más que compañeros de trabajo. Gracias a todos ellos por los buenos momentos.

Tampoco he olvidado de expresar mi agradecimiento a Jaime, al que me unió un proyecto común y con el que, a lo largo de los años, me ha llegado a unir una profunda amistad. Él formó parte indispensable en el diseño y el montaje de nuestra cámara de cielo y sin su ayuda mi trabajo habría sido mucho más dificil. También han sido muchas las charas que hemos tenido que me han sido de gran ayuda, y por supuesto tengo un buen recuerdo de los buenos momentos que hemos pasado juntos dentro y fuera del CEAMA.

También quiero expresar mi agradecimiento a aquellas personas e instituciones que han hecho posible este trabajo. En primer lugar a Guillermo Ballester, meteorólogo de la base aerea de Armilla, y a la Agencia Estatal de Meteorología por los registros METAR usados

para la evaluación de la caracterización de cubierta nubosa. En segundo lugar mi agradecimiento a la Universidad de California San Diego, al 'Scripps Institution of Oceanograpy' y, por supuesto, a Janet Shield directora del 'Atmospheric Optics Group' por acojerme durante mis 5 meses de estancia en San Diego, así como al resto de componentes del grupo: Monette, Art y Rick, sin los que no habría sido posible la caracterización de propiedades ópticas del aerosol atmosférico. En tercer lugar, a la colaboración del Departamento de Energía de los EEUU como parte de la 'Atmospheric Radiation Program Climate Research Facility' y al investigador principal del CIMEL de AERONET de dicho sitio el Dr. Richard Wagener por los datos para la caracterización del aerosol y por acojerme durante mi estancia en el 'Brookhaven National Laboratory' al que también extiendo mis agradecimientos. Por último agradecer al Ministerio de Ciencia y Tecnología y la Consejería de Innovación, Ciencia y Empresa de la Junta de Andalucía por el soporte económico ya fuera en forma de proyectos, becas o ayudas.

Finalmente, quiero agradecer a mis amigos y mi familia que siempre me han acompañando y apoyado, y mi más profundo agradecimiento a mis padres. Mi padre solía decir que el único legado que me podían dejar era mi formación y, desgraciadamente, él ya no está aquí para poder leer estas líneas o ver el día en que, gracias a ellos, alcance esta meta. Todo este esfuerzo y trabajo está dedicado a él y a mi madre.

Contents

Resumen

La cobertura nubosa es una medida meteorológica que se registra por inspección visual en todas las estaciones meteorológicas de forma sistemática, con periodicidades de una a tres horas. Las nubes afectan al tiempo atmosférico y ejercen un papel fundamental en el balance radiativo del planeta en general y de la superficie terrestre en particular. La cobertura nubosa puede llegar a reducir la radiación solar hasta en un 99%, y los diferentes tipos de nubes ejercen un papel primordial en el balance de energía, ya que las nubes reflejan hacia el espacio la radiación proveniente del Sol, pero también absorben la radiación infrarroja proveniente del suelo. Esta influencia de las nubes sobre la radiación es especialmente importante en el ultravioleta ya que existen configuraciones de tipo y posición en el cielo de las nubes en las que la radiación ultravioleta es mayor de la esperada.

Por otro lado la suspensión de partículas en la atmósfera (aerosol atmosférico) también ejerce un importante papel en el balance de energía. De forma directa el aerosol dispersa y absorbe la radiación y de forma indirecta influye en las nubes modificando su tiempo medio de vida y sus propiedades radiativas. El aerosol produce un efecto de enfriamiento de la Tierra, al contrario que el CO_2 y el resto de gases de efecto invernadero, sin embargo la incertidumbre acerca de la magnitud de este enfriamiento es aun muy grande por

lo que hacen falta más estudios e instrumentación para su caracterización.

Dada la importancia de la cobertura nubosa y otras propiedades macrofísicas de las nubes, así como del aerosol atmosférico, en los procesos de transferencia radiativa y de balance de energía en la Tierra, se propone el diseño de un dispositivo, la cámara de cielo (*"sky imager"*), para el registro continuo de las condiciones de cielo. Por un lado, es necesaria la información de cubierta nubosa junto con otras propiedades macrofísicas de las nubes para estudios meteorológicos y del efecto de las nubes sobre la radiación solar. Por otro lado, la importancia del aerosol atmosférico en el balance radiativo requiere establecer nuevos métodos para su caracterización.

Mientras que los dispositivos de cámara de cielo se han diseñado tradicionalmente para el registro de la cobertura nubosa, en este trabajo se plantea también su uso para la caracterización del aerosol atmosférico.

Abstract

Cloud cover is a meteorological measurement registered by visual inspection hourly or 3 hourly in all the meteorological stations. Clouds affect the weather and also have an important role in the amount of solar radiation reaching the Earth's surface. Cloud cover can reduce the solar radiation up to 99% and the different types of clouds exert a key role in the energy budget since clouds reflect incoming sun radiation, but also because they absorb Earth infrared radiation. This influence of clouds on radiation is especially important in the ultraviolet because certain configurations of clouds in the sky (type and position) yields an amount of ultraviolet radiation greater than expected.

On the other hand, the suspension of particles in the atmosphere (the atmospheric aerosol) also exerts an important role in the energy budget. Aerosol directly scatters and absorbs radiation and, indirectly affects clouds modifying their life time and radiative properties. Aerosol produces a cooling effect on the Earth system, opposite to the heating effect due to the CO_2 and the rest of green house gases, but the uncertainty is large, and therefore more studies and instrumentation are required for its characterization.

Because of the importance of cloud cover and other macrophysical properties of clouds, and the importance of the aerosol in the radiative transfer processes and energy budget, we propose the

design of a device, a sky imager, for the record of sky conditions. On one hand, the information on cloud cover and other macrophysical properties of clouds is needed for meteorological studies and studies on the cloud effect on solar radiation. On the other hand, the importance of the aerosol on the radiative budget requires establishing new methods for its characterization.

While sky imager systems have been design primarily for cloud cover characterization, in this work we also propose the use for aerosol characterization.

1

Introduction

Solar radiation is the only external energy source for the Earth-Atmosphere system and it is the direct or indirect responsible of all the phenomena affecting its meteorology and climatology. In average, the Earth emits to the space the same energy that absorbs from the Sun. Thus, any factor altering the composition of the atmosphere or the energy emitted by the Sun modifies the net radiative balance of the Earth-Atmosphere system and therefore, affects the climate.

This work focuses on the development of a sky imager and the techniques for characterization of two of the most important elements in the atmosphere affecting the Earth radiation budget: clouds and the atmospheric aerosol.

1.1 Clouds

Clouds are one of the most significant elements of the atmospheric system, playing several key roles (Seinfeld and Pandis, 1998). First, the radiation budgets at the top of the atmosphere, as observed from satellites, are closely related to the cloud field. Second, a small change in the cloud parameters may significantly amplify or offset climatic temperature perturbations due to the increase in CO_2 and other greenhouse gases. Third, in general, high clouds act as a greenhouse and warm the Earth, whereas low clouds, by reflecting sunlight back to space tend to cool the planet (solar albedo effect) (Liou, 1992).

Concerning the influence of clouds in the Earth's radiation budget we talk about the radiative effect of clouds. One of the prominent uncertainties in climate modeling is how the cloud system reacts in response to increases in the levels of greenhouse gases (Seinfeld and Pandis, 1998).

Calbó et al. (2005) reviewed the importance of clouds on ultraviolet radiation. UV radiation is defined as electromagnetic radiation having wavelengths within the range 100 – 400 nm and have important implications for human health (i.e. Berwick and Kesler, 2005; Godar, 2005; Grant and Holick. 2005). Because clouds are formed by small water droplets or ice crystals, radiation is scattered when passing through them, resulting in extinction or diminished transmittance of the atmosphere. Therefore, the usual effect of clouds is the attenuation of UV radiation reaching the Earth's surface (Bais et al., 1993). Nevertheless, ground level UV radiation may be affected by clouds in such a manner that sometimes it may be higher than UV radiation in cloudless conditions. This effect, known as cloud enhanced UV, is described in various studies (Estupiñan et al., 1996; Schafer et al., 1996; Sabburg and Wong, 2000; Sabburg et al., 2003) but the magnitude of this enhancement is not well established (Calbó et al., 2005).

Despite their great importance, clouds still remain one of the least understood components of the weather and climate system.

1.2 The atmospheric aerosol

Solid and liquid particles suspended in the atmosphere (the atmospheric aerosol) interacts both directly and indirectly with the Earth's radiation budget and climate (Horvath, 1998). The radiative forcing is defined by Ramaswamy et al. (2001) as the change in net (downward minus upward) irradiance (solar plus longwave; in W m^{-2}) at the tropopause after allowing for stratospheric temperatures to readjust to radiative equilibrium, but with surface and tropospheric temperatures and state held fixed at the unperturbed values. Radiative forcing is used to assess and compare the anthropogenic and natural drivers of climate change. Positive radiative forcings lead to a global mean surface warming and negative radiative forcings to a global mean surface cooling. Radiative forcing normally refers to the difference in net irradiance between the present and the beginning of the industrial era (approximately 1750) (Foster et al., 2007).

The direct effect is the mechanism by which aerosol scatter and absorb shortwave and longwave radiation, thereby altering the radiative balance of the Earth – atmosphere system (Foster et al., 2007). Scattering of aerosol exert a net negative direct radiative forcing, while partially absorbing aerosol may exert a negative direct radiative forcing over dark surfaces such as oceans or dark forest surfaces, and a positive radiative forcing over bright surfaces such as deserts, snow and ice, or if the aerosol is above clouds (e.g. Chylek and Wong, 1995; Haywood and Shine, 1995). Both positive and negative direct effect mechanisms reduce the

shortwave irradiance at the surface. The longwave direct effect is only substantial if the aerosol particles are large and occur in considerable densities at higher altitudes (Tegen et al., 1996).

The indirect effect is the mechanism by which aerosol modifies the microphysical and hence the radiative properties, amount and lifetime of clouds. Key parameters for determining the indirect effect are the effectiveness of an aerosol particle to act as a cloud condensation nucleus, which is a function of the size, chemical composition, mixing state and ambient environment (Penner et al., 2001). The microphysically induced effect on the cloud droplet number concentration and hence the cloud droplet size, with the liquid water content held fixed, has been called the 'first indirect effect' (Ramaswamy et al., 2001), 'cloud albedo effect' (Lohmann and Feichter, 2005) or 'Twomey effect' (Twomey, 1977). The microphysically induced effect on the liquid water content, cloud height, and lifetime of clouds has been called the 'second indirect effect' (Ramaswamy et al., 2001), 'cloud lifetime effect' (Lohmann and Feichter, 2005) or 'Albrecht effect' (Albrecht, 1989). Figure 1.1 shows a schematic diagram of the different effects of the atmospheric aerosol.

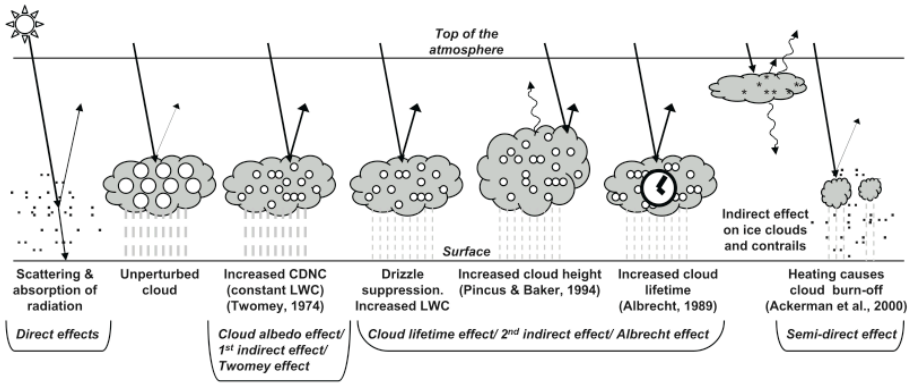

Figure 1.1. Schematic diagram showing the various radiative mechanisms associated with cloud effects that have been identified as significant in relation to aerosol. The small black dots represent aerosol particles; the larger open circles cloud droplets. Straight lines represent the incident and reflected solar radiation, and wavy lines represent terrestrial radiation. The filled white circles indicate cloud droplet number concentration (CDNC). The unperturbed cloud contains larger cloud drops as only natural aerosol particles are available as cloud condensation nuclei (CCN), while the perturbed cloud contains a grater number of smaller cloud drops as both natural and anthropogenic aerosol particles are available as cloud condensation nuclei. The vertical gray dashes represent rainfall, and LWC refers to the liquid water content. (From Foster et al., 2007 modified from Haywood and Boucher, 2000)

IPCC reported that the anthropogenic contributions to aerosol (primarily sulfate, organic carbon, black carbon, nitrate and dust) together produce a cooling effect, with a total direct radiative forcing of –0.5 [–0.9 to –0.1] W m^{-2} and an indirect cloud albedo forcing of –0.7 [–1.8 to –0.3] W m^{-2} (Foster et al., 2007). This can be compared to the forcing induced by the increase of the greenhouse

effect gases concentration during the last century (Foster et al., 2007). However, radiative forcing induced by aerosol has a factor of two uncertainty, and may thus have much more importance in the overall energy balance. Figure 1.2 shows the principal components of the radiative forcing of climate change.

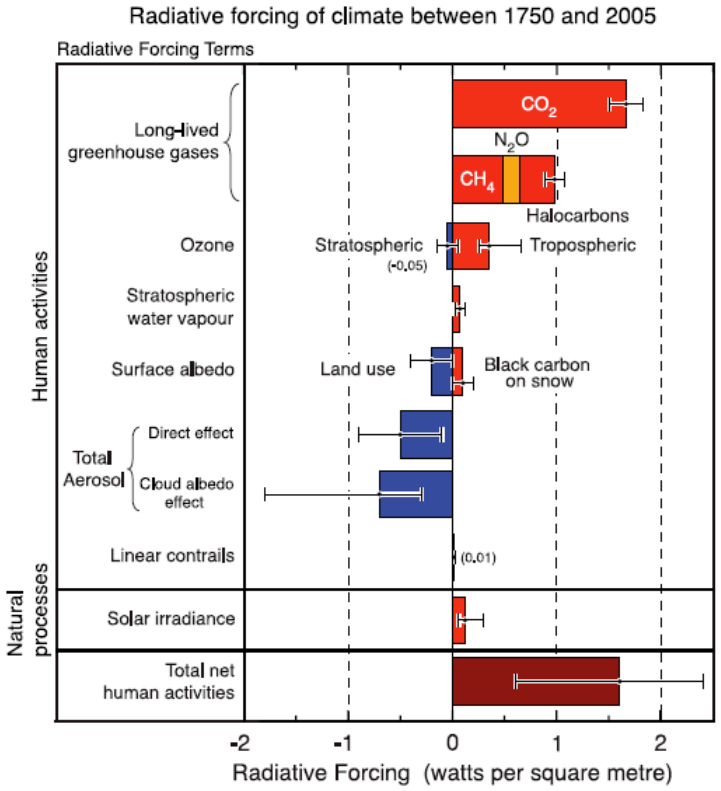

Figure 1.2. Summary of the principal components of the radiative forcing of climate change. All these radiative forcings result from one or more factors that affect climate and are associated with human activities or natural processes. The values represent the forcings in 2005 relative to the start of the industrial era (about 1750). The thin black line attached to each colored bar represents the range of uncertainty for the respective value. (From Foster et al., 2007)

Aerosol is the dominant uncertainty in radiative forcing. Solving these uncertainties induced by the different factors contributing to the radiative forcing due to aerosol is decisive in the estimation of the total uncertainty in radiative forcing (Foster et al., 2007).

Knowledge of the variables that determine the optical and microphysical properties of atmospheric aerosol is essential for the determination of their climate effects. Nevertheless, there are many difficulties in evaluating the climate effects of the aerosol due to the great spatial and temporal variability of their densities and properties. Remote sensing (from satellite and ground-based) appears to be a valuable tool for characterizing the microphysical and optical properties of the aerosol (Foster et al., 2007).

1.3 Outline of this work

The structure of this work is the following:

Chapter 2 describes the background to fully understand the characterization of the cloud cover and atmospheric aerosol from the ground surface using sky imagery.

Chapter 3 describes the sites where the instruments gathered the data used in this work.

Chapter 4 presents the two imagers used in this work and the sun photometer CIMEL CE318. The main core of this work involved the development of the All-Sky Imager. This work also used the calibrated Whole Sky Imager as collaboration between the Atmospheric Physics Group from University of Granada and the Atmospheric Optics Group from University of California at San Diego, where this instrument has been designed and developed.

Chapter 5 introduces the technique for cloud cover estimation applied to the All-Sky Imager. Starting with a review of the traditional algorithms and then, the new approach proposed. This approach with neural networks and genetic algorithms requires a brief introduction to these techniques. Finally the design of the algorithms, the final procedure and the results and evaluation of the process are presented.

Chapter 6 presents a methodology for aerosol optical depth estimation and its spectral dependency with the All-Sky Imager and the WSI and then, an inversion code applied to the WSI data for the retrieval of the aerosol size distribution.

Chapter 7 presents the concluding remarks. First of all, we present a brief summary of the sky imager itself. Then, we discuss the methodology for cloud detection and aerosol characterization. Finally, some notes for future work.

After the references, it is included a list of publications related to the thesis that have been published in different journals or scientific conferences.

2

Background

This chapter describes the background to fully understand the characterization of the cloud cover and atmospheric aerosol from the ground surface using sky imagery.

First section is an introduction to the Earth's atmosphere. Second section introduces the solar radiation and its interaction with the atmosphere. Following sections describe the two more interesting elements in the atmosphere for this work, clouds and the atmospheric aerosol.

2.1 The Atmosphere

The Earth's atmosphere can be divided into a number of well defined horizontal layers, mainly on the basis of temperature as is shown in Figure 2.1 (Barry and Chorley, 2003).

The troposphere is the lowest layer of the atmosphere and it is the zone where weather phenomena and atmospheric turbulence are most marked. It begins at the surface and extends to between 8 km at the poles and 16 km at the equator, with some variation due to weather factors. Temperature decreases with height at a mean rate of about 6.5°C. It contains 75% of the total molecular or gaseous mass of the atmosphere and virtually all the water vapor, and therefore the clouds (see section 2.3), and particles (aerosol particles as explained in section 2.4). The troposphere is capped in most places by a temperature inversion level (i.e. a layer of relatively warm air above a colder layer) and in others by a zone that is isothermal with height. The troposphere thus remains to a large extent self-contained, because the temperature inversion acts as a lid that effectively limits convection. This inversion level is called the tropopause.

The stratosphere extends upward from the tropopause to about 50 km. Temperature increases with height. The stratosphere contains the ozone layer, the part of the Earth's atmosphere that contains most of the ozone in the whole atmosphere. It is mainly located in the lower portion of the stratosphere from approximately 15–35 km above Earth's surface, though the thickness varies

seasonally and geographically. The limit of the stratosphere is marked by a zone that is isothermal with height, the stratopause.

Above the stratopause, the mesosphere extends from about 50 km to the range of 80–90 km. Temperature decreases with height, reaching –130°C in the upper mesosphere.

The thermosphere extends from 80–90 Km and temperature increases with height. The temperature of this layer can rise to 1,500°C. The International Space Station orbits in this layer, between 320 and 380 km.

The exosphere extends from 500–750 km up to 10,000 km and contains free-moving particles.

The Earth's atmosphere is composed of two groups of gases, one with nearly permanent concentrations and another with variable concentrations (Table 2.1). Nitrogen (N_2), oxygen (O_2) and argon (Ar) account for more than 99.96% of the atmosphere by volume. The permanent gases have virtually constant volume ratios up to an altitude of about 60 km. The amounts of variable gases are small, but they are extremely important in the radiation budget of the atmosphere. Water vapor is the major radiative and dynamic element in the Earth's atmosphere. The H_2O concentration varies significantly with both space and time. The highly variable spatial distribution of tropospheric H_2O is determined by the local hydrological cycle via evaporation, condensation (i.e. cloud formation) and precipitation (rainfall), and by large-scale transport processes. The stratospheric H_2O concentration is relatively small,

with a value of approximately 3–4 ppmv in the lower stratosphere. The atmosphere also contains various kinds of particles suspended in the air, the atmospheric aerosol, which are highly variable in space and time.

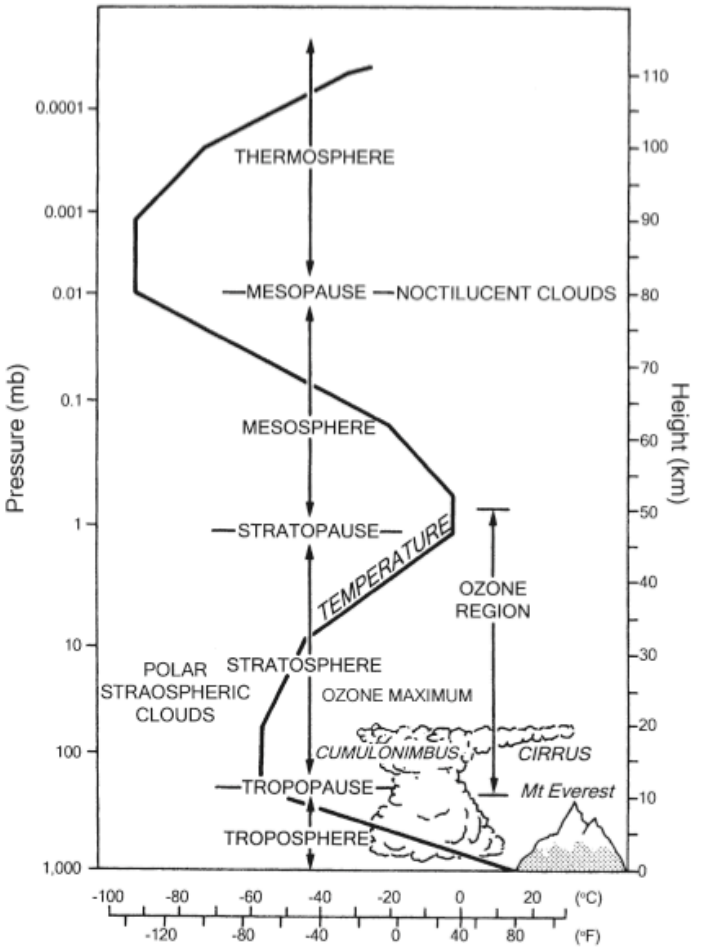

Figure 2.1. Vertical distribution of temperature and pressure up to 110 km. (From Barry and Chorley, 2003)

Permanent		Variable	
Element	**% volume**	**Element**	**% volume**
Nitrogen	78.084	Water vapor	0 – 0.04
Oxygen	20.948	Ozone	0 – $12x10^{-4}$
Argon	0.934	Sulfur dioxide	$0.001x10^{-4}$
Carbon dioxide	0.033	Nitrogen dioxide	$0.001x10^{-4}$
Neon	$18.18x10^{-4}$	Ammonia	$0.004x10^{-4}$
Helium	$5.24x10^{-4}$	Nitric Oxide	$0.0005x10^{-4}$
Krypton	$1.14x10^{-4}$	Hydrogen Sulfide	$0.00005x10^{-4}$
Xenon	$0.089x10^{-4}$		
Hydrogen	$0.5x10^{-4}$		
Methane	$1.5x10^{-4}$		
Nitric oxide	$0.27x10^{-4}$		
Carbon monoxide	$0.19x10^{-4}$		

Table 2.1. U.S. Standard Atmosphere (1976) composition.

2.2 Solar radiation: atmospheric interaction

The measurement of the interaction between solar radiation and atmosphere requires dealing quantitatively with light and defining radiometric quantities. The basis of the radiometric quantities is the monochromatic radiant flux Φ_λ, which is defined as the radiant power or radiant energy, Q, through a control surface per second at a given wavelength λ. This magnitude does not provide any information about the distribution of the energy in a direction or over a surface. The radiant flux, $d\Phi_\lambda$, received (or emitted) crossing an area, dS, on a detector (or source), without considerations about the direction is defined as the radiant flux density or irradiance:

$$E_\lambda = \frac{d\Phi_\lambda}{dS}. \tag{2.1}$$

In order to characterize the emission of point sources, the radiant intensity I_λ represents the radiant flux $d\Phi_\lambda$, propagated in a solid angle $d\Omega$. Its definition is

$$I_\lambda = \frac{d\Phi_\lambda}{d\Omega}. \tag{2.2}$$

For extended sources the radiance, defined as the flux emitted per unit solid angle and unit area (perpendicular to the direction considered *s*), is used. If θ is the angle between the normal of the radiating surface and the direction in which the emitted radiant flux is considered, the radiance is given by

$$L_\lambda = \frac{d^2\Phi_\lambda}{dS d\Omega \cos\theta} \tag{2.3}$$

Figure 2.2 shows a schematic diagram of the definition of radiance. The notation given above is summarized with units in table 2.2.

Radiometric quantity	Symbol	Unit
Radiant energy	Q	J
Radiant flux	Φ_λ	$W\mu m^{-1}$
Radiant flux density (irradiance)	E_λ	$W\ m^{-2}\ \mu m^{-1}$
Radiant intensity	I_λ	$W\ \mu m^{-1}\ sr^{-1}$
Radiance	L_λ	$W\ m^{-2}\ \mu m^{-1}\ sr^{-1}$

Table 2.2. Radiometric symbols and units

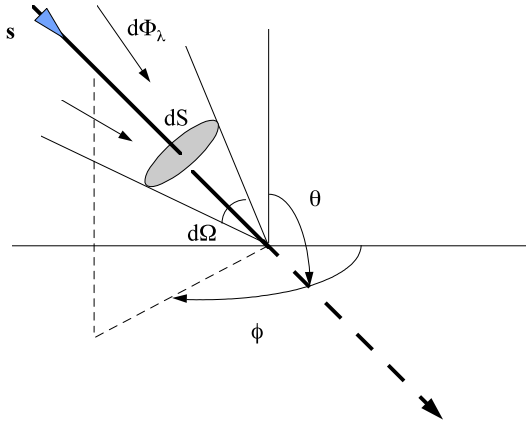

Figure 2.2. Definition of radiance. Zenith angle θ and Azimuth angle ϕ define the direction of the radiant flux *s*.

Solar radiation as it travels through the atmosphere (without clouds) suffers attenuation due to the scattering and absorption produced by the atmospheric components (gases and particles). In the scattering process the energy transported by an electromagnetic wave is scattered in every direction as a consequence of the interaction of this wave with the particles in the medium. Part of the scattered radiation comes back to the space and another part reaches the Earth's surface (diffuse radiation). Thus, in this process the incident energy does not form part of the internal energy of the particle. On the other hand, in the absorption process the energy becomes part of the internal energy of the particle. As a consequence the radiation that reaches the Earth's surface without a

change in its direction (direct radiation) suffers attenuation. Figure 2.3 shows a schematic diagram of the radiation distribution.

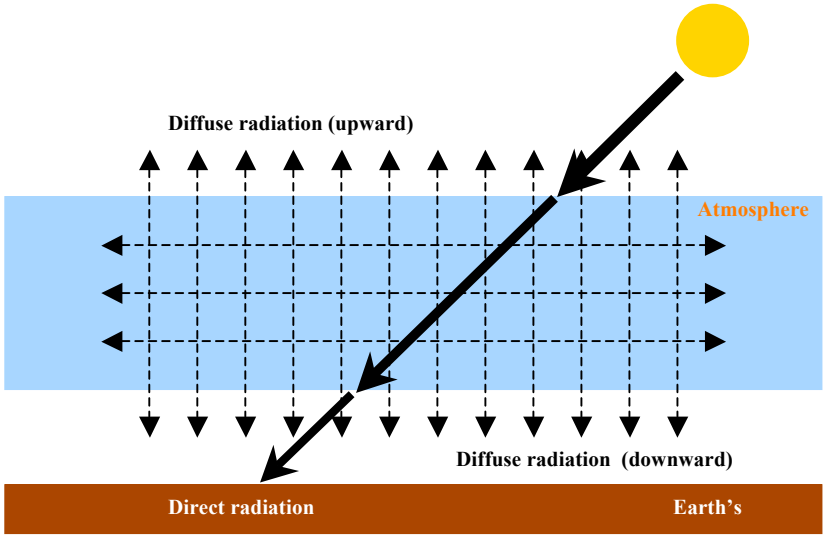

Figure 2.3. Distribution of the solar radiation components as they travel through the atmosphere.

2.2.1 Scattering and absorption processes in the atmosphere

The atmosphere presents basically two scattering phenomena, the first one due to molecules in the air, Rayleigh scattering, and the second one due to particles, Mie scattering. (Iqbal, 1983).

Rayleigh theory, published in 1899, was developed to demonstrate that the blue of the sky is a consequence of the scattering of solar radiation due to molecules in the air. Assuming that the scattering nuclei are small compared to the wavelength, Rayleigh described the spectral distribution of sky radiance and its polarization. The solution presents a dependency of the intensity of

the scattering proportional to λ^{-4} and a little dependency of the scattering angle.

On the other hand, Gustav Mie (1908) solved the Maxwell equations for the problem of the interaction of an electromagnetic wave with a sphere, assuming that the sphere is homogeneous and isotropic. A deep description of both theories is presented by Bohren and Huffman (1983).

The formulation describes two basic optical properties, the absorption and the scattering of solar radiation by a spherical particle. These properties depend on the size parameter (x) defined as a relation between the radius of the particle and the wavelength of the incident wave ($2\pi r/\lambda$) and also on the refractive index m, that depends on the chemical composition of the particle. The scattered radiance also depends on the scattering angle, Θ, and the function that describes its angular distribution, the phase function. Mie reached to an expression for the extinction coefficient σ_e for a suspension of spherical particles of different radii (between r_1 and r_2):

$$\sigma_e = \int_{r_1}^{r_2} \pi r^2 Q_e(x,m) n(r) dr \,, \tag{2.4}$$

where Q_e is the extinction efficiency factor and can be understood as the effectiveness with which the particle interacts with the radiant flux, and $n(r)$ is the size distribution of those spherical particles (see section 2.4.4).

Mie theory is applied when the size of the particles is comparable to the incident wavelength ($x \sim 1$), producing interference patterns with the partial waves emitted by the multipoles of the particles having phase differences. For this reason there is a strong angular dependency, there is an increase in the forward scattering (compared to Rayleigh scattering) and the chromatic dependency of the scattering is smaller. Mie theory converge into Rayleigh theory when x decreases, therefore Rayleigh theory can be explained with Mie theory, but due to the simplicity of Rayleigh theory they usually are applied separately. Figure 2.4 shows the differences in the scattering for both theories. Rayleigh scattering is symmetric respect to the plane perpendicular to the propagation direction and find its minimum at $\Theta = \pm 90^{\circ}$. On the other hand Mie scattering presents an asymmetry, with a strong forward scattering.

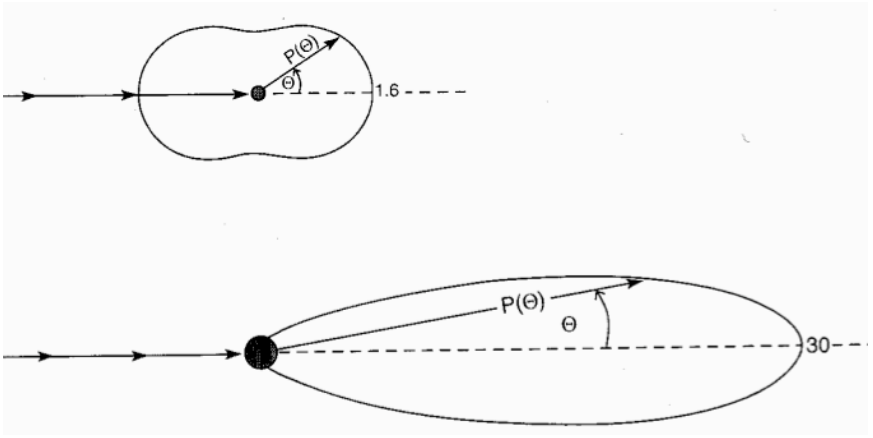

Figure 2.4. Up, Rayleigh scattering. Down, Mie scattering.

Solar radiation is also partially absorbed by the atmospheric components increasing their internal energy and therefore their temperature. The absorption process depends on the energy state of a molecule. The absorbed radiation is used to produce a transition from one energy state to another. Because the state energy associated to some kinds of energy, like rotational, vibrational or electronical energies, are quantized the absorption process occurs only at discrete wavelengths and is called selective absorption. When the absorption takes place over a number of wavelengths very close to each other it is possible some overlap and it is called band absorption (Iqbal, 1983).

The main molecular absorbers are H_2O (water vapor), CO_2, O_3, N_2O, CO, O_2, CH_4 and N_2. The minor absorbers are oxides of nitrogen NO_2, N_2O_4, N_2O_5; hydrocarbon combinations C_2H_4, C_2H_6, C_3H_8; and sulfurous gas H_2S. Most of these absorbers are active mainly in the near- and far-infrared wavelengths regions (from 0.7 to 100 μm). Atomic gases as O and N, on the contrary, absorb mainly the maximum UV and shorter wavelengths. Figure 2.5 shows the main molecular absorbers for the solar radiation spectrum.

Both scattering and absorption occur simultaneously, because all materials scatter, at least via their molecules, and absorb. The attenuation of the radiant energy in a real medium is expressed by the extinction coefficient σ_e, defined by the sum of the scattering (σ_s) and absorption (σ_a) coefficients: $\sigma_e = \sigma_s + \sigma_a$

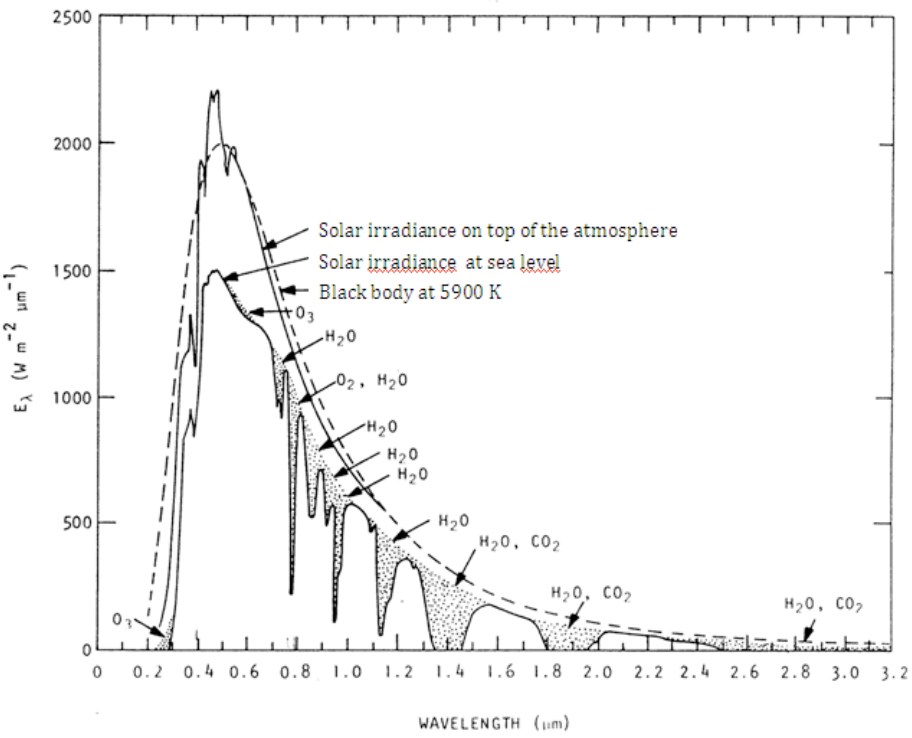

Figure 2.5. Identification of the various molecular absorbers. The graph shows the solar irradiance on top of the atmosphere, at sea level and also the corresponding irradiance for a black body at 5900 K.

2.2.2 Radiative Transfer Equation

Let us consider a volume dV of an isotropic non absorbing medium hit by a radiant flux characterized by the irradiance E. The flux $d^2\Phi$ scattered by dV in the solid angle $d\Omega$ at a given direction Θ respect to the incident direction is

$$d^2\Phi = Ef(\Theta)dVd\Omega\,, \tag{2.5}$$

where $f(\Theta)$ (in m^{-1} sr^{-1}) is the scattering function, that characterizes the angular distribution of scattered photons by the particles in the medium.

The amount of scattered flux is obtained integrating in all directions

$$d\Phi = EdV\int_{4\pi} f(\Theta)d\Omega\,. \tag{2.6}$$

The flux scattered by the volume dV must be equal to the flux lost due to scattering along the thickness of the volume ds. Then, the incident flux in a transversal section of the volume is noted EdA and the amount of scattered flux is $d\Phi=\sigma_s EdAds=\sigma_s EdV$. Thus, using equation 2.6 we obtain the relationship between $f(\Theta)$ and the scattering coefficient

$$\sigma_s = \int_{4\pi} f(\Theta)d\Omega\,. \tag{2.7}$$

If we are interested only on the angular dependency of $f(\Theta)$, we define the phase function $P(\Theta)$, related to $f(\Theta)$ by the following expression

$$P(\Theta) = 4\pi\frac{f(\Theta)}{\sigma_s}\,. \tag{2.8}$$

This parameter $P(\Theta)$ represents the fraction of scattered radiation in the direction Θ, per solid angle, respect to the scattered radiation in all directions.

The relative importance of the scattering and absorption is characterized with the single scattering albedo

$$\omega_0 = \frac{\sigma_s}{\sigma_s + \sigma_a} = \frac{\sigma_s}{\sigma_e} \tag{2.9}$$

Let us now consider a radiant flux propagating in a direction perpendicular to the thickness *ds* of a medium. The extinction of the radiance along the thickness is defined by means of the optical thickness

$$\tau_\lambda = \int_{s_1}^{s_2} \sigma_e ds\,. \tag{2.10}$$

In atmospheric problems is common the use of the optical depth, or normal optical thickness (δ) as the optical thickness measured vertically

$$\delta_\lambda = \int_{z_1}^{z_2} \sigma_e dz\,. \tag{2.11}$$

The relationship between optical thickness and optical depth is

$$\tau_\lambda = \delta_\lambda m_0\,, \tag{2.12}$$

and m_0 is the optical air mass. In equation 2.12 the optical air mass m_0 is a function of the solar zenithal angle (θ_0) defined as the angle between the zenith (the vertical direction) and the direct solar irradiance path. Its relation can be approximate with the following expression (Kasten, 1966):

$$m_0 = \frac{1}{\cos(\theta_0)}. \tag{2.13}$$

Equation 2.13 works assuming a uniform atmosphere with refractive index equal to one and considering a plane-parallel atmosphere (Iqbal, 1983). This approximation can be applied for θ_0 smaller than 80º. Otherwise, it has to be used a different approximation (i.e. Kasten and Young, 1989).

Based on the principle of conservation of energy we present the equation that describes the radiative transfer in a medium. The variation of radiance dL_λ, observed when a radiant flux travels through a volume (figure 2.6) has two components. On one hand, due to the attenuation

$$dL_\lambda^{\ 1} = -\sigma_e L_\lambda ds. \tag{2.14}$$

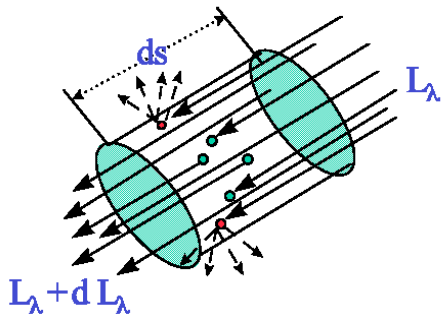

Figure 2.6. Schematic draw of the variation of the radiance observed when a radiant flux beam travels through a volume

On the other hand, the radiant flux can be intensified by the emission of the medium and the multiple scattering. This effect is quantified by the coefficient J_λ.

$$dL_\lambda^{\,2} = \sigma_e J_\lambda ds\,. \tag{2.15}$$

Thus, the total variation in the radiance is $dL_\lambda = dL_\lambda^{\,1} + dL_\lambda^{\,2}$. If we divide this expression by $\sigma_e ds$, the result is the general radiative transfer equation

$$\frac{dL_\lambda}{\sigma_e ds} = -L_\lambda + J_\lambda\,. \tag{2.16}$$

If the contribution due to emission is not considered, the source function can be expressed in term of the phase function $P(\Theta)$, and the radiative transfer equation presents this form

$$\frac{dL_\lambda}{\sigma_e ds} = -L_\lambda + \frac{\omega_{0\lambda}}{4\pi}\int_\Omega L_\lambda P(\Theta) d\Omega\,. \tag{2.17}$$

The next step consists on finding a solution to the equation for a medium equivalent to the atmosphere as real as possible. The simplest geometry is a layer limited by two parallel and infinite planes, where the properties are constant and the incident radiation is also constant. This is the case of the plane-parallel atmospheres that constitute a good approximation for the real atmosphere, where the vertical variations are faster than the horizontal variations for all the magnitudes. In this situation is

convenient measuring the distance over the vertical direction *z*, i.e. normal to the stratification plane (figure 2.7).

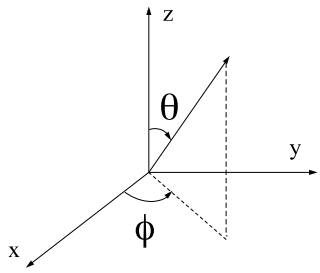

Figure 2.7. Coordinates defining a point. θ is the zenith angle and ϕ is the azimuth angle. The coordinates are noted with a 0 subscript refer to sun position.

This geometry allows approximating the optical mass to $m^{-1} = \mu = cos(\theta)$. Applying the variable change $dz=\mu ds$ in equation 2.16 and using the optical depth (equation 2.11) we obtain

$$\mu \frac{dL_\lambda(\delta_\lambda,\mu,\phi)}{d\delta_\lambda} = -L_\lambda(\delta_\lambda,\mu,\phi) + J_\lambda(\delta_\lambda,\mu,\phi). \qquad (2.18)$$

Let us assume that the input radiance does not vary with time, does not present horizontal gradients and that the atmosphere is isotropic. Multiplying equation 2.18 by $e^{-\delta_\lambda/\mu}$ and integrating between δ_0=0 (top of the atmosphere) and δ_λ, we obtain the solution for emerging radiance through the atmosphere from the level δ_λ

$$L_\lambda(\delta_\lambda,\mu,\phi) = L_\lambda(\delta_0,\mu,\phi)e^{\frac{-(\delta_0-\delta_\lambda)}{\mu}} + \int_{\delta_\lambda}^{\delta_0} J_\lambda(\delta'_0,\mu,\phi)e^{\frac{-(\delta_0-\delta_\lambda)}{\mu}} \frac{d\delta'_\lambda}{\mu}. \quad (2.19)$$

The physical interpretation is simple (figure 2.8). The radiance that reaches the level δ_λ is equal to the radiance on δ_0 attenuated between both levels, plus the contribution of the medium attenuated by the successive layers δ'.

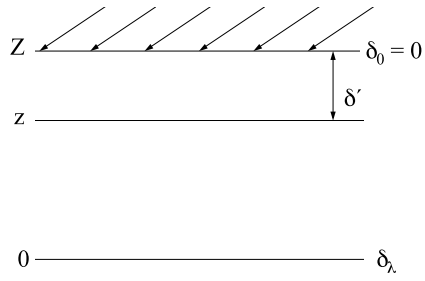

Figure 2.8. Plane-parallel atmosphere irradiated by a solar beam.

In the case of the direct sun irradiance, where the contributions for emission and scattering in directions other than the direct flux can be discarded, the solution to the radiative transfer equation can be reduced to the Beer-Bouguer-Lambert Law:

$$E_\lambda(\delta_\lambda,\mu,\phi) = E_\lambda(\delta_0,\mu,\phi)e^{\frac{-(\delta_0-\delta_\lambda)}{\mu}} \quad (2.20)$$

This expression tells us that the attenuation of the direct irradiance follows an exponential function.

2.3 Clouds in the atmosphere

Clouds are collections of droplets and crystals suspended in the air (Kokhanovsky, 2006). They are global in nature and regularly cover about 60% of the Earth's surface. Average global cloud coverage over the oceans is estimated at 65% and over land at 52% (Warren et al., 1986, 1988). The occurrence of clouds shows dramatic geographical variation and is generally restricted to the lowest 4 to 6 km of the troposphere except for cirrus. Clouds form and evaporate repeatedly. Only a small fraction (about 10%) of the clouds that form actually generate precipitation (Seinfeld and Pandis, 1998).

Clouds are conventionally classified in terms of their position and appearance in the atmosphere from the ground. The cloud classification system was proposed by Luke Howard in 1803 and has been adopted internationally (Rogers and Yau, 1989). WMO (1983) defines the essential requirements of this international system. Clouds are classified according to a Latin *Linnean* system (similar to the one used for plants and animals), which is based on the altitude of their bases, their vertical development and their structure. Most clouds fall into one of ten basic groups, known as *genera*. The troposphere is divided into three levels: low, middle and high. These are sometimes called *étages*. The height of the troposphere varies with latitude, but in the mid-latitude temperate regions of the world the clouds with base height below 2 km (sometimes 4 km) are designated low-level clouds, a category that includes stratocumulus (Sc), stratus (St) and nimbostratus (Ns). The

group of middle clouds with base height between 2 and 7 km consist of altocumulus (Ac) and altostratus (As). Cirrus (Ci) cirrostratus (Cs) and cirrocumulus (Cc) constitute a group of high-level clouds with base height above 7 km. Even though the base height designates the *étage*, some clouds extend through several *étages* (clouds with vertical development): cumulus (Cu) and cumulonimbus (Cb) (Seinfeld and Pandis, 1998). A summary of the *genus* classification is shown in Table 2.3.

Étages	**Genus**
Low level clouds	Stratocumulus (Sc)
	Stratus (St)
	Nimbostratus (Ns)
Mid level clouds	Altocumulus (Ac)
	Altostratus (As)
High level clouds	Cirrus (Ci)
	Cirrostratus (Cs)
	Cirrocumulus (Cc)
Clouds with vertical development	Cumulus (Cu)
	Cumulonimbus (Cb)

Table 2.3. Cloud classification.

WMO (1983) also defines the standard for manually recording cloud area. This standard is presented in Table 2.4. The unit of measurement of cloud area is the okta, meaning one eighth of the whole-sky as seen by an observer. Sometimes cloud area is quoted in tenths or even in percent.

Code	Okta	Area of cloud (tenths)
0	None	None
1	1 okta or less, but not zero	1/10 or less, but not zero
2	2	2/10 to 3/10
3	3	4/10
4	4	5/10
5	5	6/10
6	6	7/10 to 8/10
7	7 okta or more, but not zero	9/10 or more, but not 10/10
8	8	10/10
9	Sky obscured, or cloud area cannot be estimated	
/	No measurement made	

Table 24. International scale of cloud area (WMO, 1983).

Additionally, there has been a variety of other cloud properties estimated by direct observations for the purposes of radiation studies. Some of them include cloud obstruction of the sun (e.g. McKenzie et al. 1998), cloud thickness (e.g. Bener, 1964), cloud altitude (e.g. Frederick and Steele, 1995) and cloud velocity (Platt et al., 1994). Long et al. (2006) also describe other estimators as the uniformity of cloud coverage and the cloud brokenness.

2.4 The atmospheric aerosol

The atmosphere continuously contains particles ranging in size from a few nanometers to tens of micrometers in diameter. These particles are always present in the atmosphere and show highly variable densities. Aerosol is defined as a system

composed by a gas and solid or liquid particles suspended on it at least several minutes. If the gas taken into account is the atmosphere, the system formed by the gases and particles in the atmosphere is the atmospheric aerosol (Horvath, 1998).

Aerosol particles and gases present different characteristics. Atmospheric gases are invisible and react chemically, while the aerosol particles affect the visibility and they have less chemical activity. There are two ways for aerosol production: gas-to-particle conversion and mechanical processes. Approximately half the mass of atmospheric aerosol is produced by gas-to-particle conversion.

Gas-to-particle conversion includes the production of solid and liquid particles from substances in gas form. This production is due to the formation of new particles (homogeneous condensation) or the condensation on existing particles (heterogenic condensation). Whitby (1978) estimates that 95% of the aerosol mass produced is condensed on existing particles. In urban areas, Whitby (1980) concludes that 20% of the transformed mass by gas-to-particle conversion is used to produce new particles, and 80% is condensed in existing particles. Gases included in these processes are sulfur dioxide, nitrogen dioxide and hydrocarbons.

Mechanical processes conduct to the direct injection of aerosol into the atmosphere (dust, salt crystals, etc.) from volcanic eruptions, fires, sea spray and other natural processes.

Finally, atmospheric aerosol can be eliminated from the atmosphere by sedimentation, precipitation and the impact with obstacles. Normally, the coagulation is not considered an elimination process since it is part of the aerosol dynamic. With coagulation, particles grow in size but the total mass is the same. However, if we consider the atmospheric effects of the aerosol, coagulation can be treated as an elimination process.

2.4.1 Aerosol classification

Classifying aerosol according to size we have fine particles (less than 2.5 μm in diameter) and coarse particles (greater than 2.5 μm in diameter). Fine particles can often be divided roughly into two modes: the nuclei mode (or aitken mode) and the accumulation mode. The nuclei mode, extending from about 0.005 to 0.1 μm diameter, contains particles formed from condensation of hot vapors during combustion processes and from the nucleation of atmospheric species to form fresh particles. They are lost principally by coagulation with larger particles. The accumulation mode extending from 0.1 to 2.5 μm diameter contains particles formed from coagulation of particles in the nuclei mode and from condensation of vapors onto existing particles, causing them to grow into this size range. The accumulation mode is so named because particle removal mechanisms are least efficient in this regime, causing particles to accumulate there. The coarse mode, from >2.5 μm diameter, is formed by mechanical processes and usually

consists of man-made and natural dust particles (Seinfeld and Pandis, 1998). Figure 2.9 shows an idealized schematic depicting the typical distribution of surface area of an atmospheric aerosol.

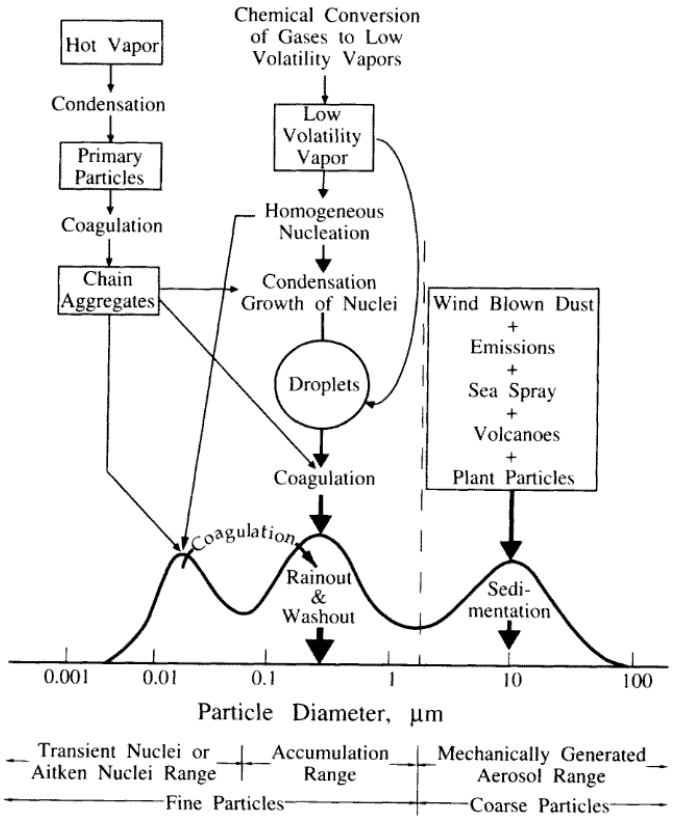

Figure 2.9. Idealized schematic of the distribution of particle surface area of an atmospheric aerosol (Whitby and Cantrell, 1976). Principal modes, sources and particle formation and removal mechanisms are indicated (From Seinfeld and Pandis, 1998).

Significant natural sources of particles include soil and rock debris (terrestrial dust), volcanic action, sea spray, biomass burning, and reactions between natural gaseous emissions. Emissions of particles attributable to the activities of humans (anthropogenic aerosol) arise primarily from four source categories: fuel combustion, industrial processes, nonindustrial fugitive sources (roadway dust from paved and unpaved roads, wind erosion of cropland, construction, etc.) and transportation sources (automobiles, etc.).

Anthropogenic aerosol can be divided according to its composition in organic aerosol and inorganic aerosol (sulfates and nitrates). The largest fraction of organic aerosol is produced in the form of smoke from tropical fires (Echalar et al., 1995; Chylek and Wong, 1995; Chylek et al., 1995). For inorganic aerosol, components are mainly sulfates from petroleum derivates combustion. Densities of these components have increased rapidly since the industrial revolution (Kondratyev, 1999). Densities are larger in the northern hemisphere, where all industrial activities are focused. Sulfate aerosol does not absorb solar radiation, but scatters it reducing the solar energy reaching the Earth's surface.

2.4.2 Aerosol Optical Depth

The aerosol optical depth (AOD) is the simplest and more significant magnitude to characterize the columnar atmospheric aerosol load (Holben et al., 2001). It is the magnitude

more extended, especially in remote sensing where it is complicated (or impossible) to obtain other magnitudes. The AOD is easy to obtain with spectral direct irradiance extinction measurements. Moreover, the spectral dependency of the AOD is related to the size of particles.

The Beer-Bouguer-Lambert law (equation 2.20) presented in section 2.2.2 represents the attenuation of the monochromatic direct solar flux density as it travels through the atmosphere and reaches the Earth's surface. This attenuation is characterized by the optical thickness (equation 2.10) or the optical depth (equation 2.11) which represents the extinction due to the spectral scattering and absorption of the atmospheric components, normalized to the vertical or atmospheric column. Optical depth is calculated solving it in the Beer-Bouguer-Lambert equation (equation 2.20):

$$\delta_\lambda = \frac{-1}{m_0} \ln \frac{E_\lambda}{\rho^{-2} E_{0\lambda}}, \qquad (2.21)$$

where ρ is the correction for Earth-Sun distance and modulates the differences in the flux at the upper limit of the atmosphere along the year.

Assuming that the scattering and absorption processes are independent for the different atmospheric components, δ, is expressed as the sum of the optical depth of the different components

$$\delta_{\lambda} = \delta_{g\lambda} + \delta_{NO_2\lambda} + \delta_{w\lambda} + \delta_{O_3\lambda} + \delta_{r\lambda} + \delta_{a\lambda}, \quad (2.22)$$

where the different subscripts stand for different attenuation processes relevant in the solar spectrum, thus *g* refers to the uniformly mixed gases absorption, NO_2 to the nitrogen dioxide absorption, *w* to the water vapor absorption, O_3 to ozone absorption, *r* to the Rayleigh scattering component and *a* to the aerosol attenuation (scattering and absorption). In order to characterize the AOD the measurements are performed in wavelengths outside the strong atmospheric absorption bands and thus the absorption contributions can be discarded or corrected in a simple way (e.g. Alados-Arboledas et al, 2003).

The spectral dependency of the AOD can be approximated using the Ångström Law (Ångström, 1964):

$$\delta_{a\lambda} = \beta\lambda^{-\alpha}, \quad (2.23)$$

where α and β are the Ångström coefficients. λ is expressed in μm. α is the Ångström exponent and is related to the size of the aerosol particles. It is often used to discuss the relative proportion between fine and coarse particles in size distributions without calculating it. Its values vary from 0 to 4, but typical values are from slightly negative to 2.5, where greater values means smaller particles and vice versa. β is the turbidity factor and is related to the amount of aerosol particles and also represents the AOD at 1000 μm (Shifrin, 1995).

2.4.3 Aerosol microphysical properties

Aerosol particles are characterized by their shape, size, chemical composition and total content, which determine their radiative properties. A simple way to characterize a set of particle suspended on a fluid is by means of its density that represents the total mass per volume or air, usually represented in μg m^{-3} for atmospheric aerosol. It is also widely used the number density of particles *N*, expressed in inverse volume units.

However, the most complete description of the aerosol is provided by the size distributions (Horvath, 1998). Considering spherical particles with a radius in the logarithmic interval *[lnr, lnr+dlnr]*, the number of particles in this interval will be *dN* and the mass *dM*. The use of the logarithmic scale is useful due to the large range in size of aerosol particles. Number size distribution is denoted as

$$n(r) = \frac{dN}{d\ln r}, \tag{2.24}$$

and mass size distribution as

$$m(r) = \frac{dM}{d\ln r}. \tag{2.25}$$

In the same way, volume size distribution is defined as

$$v(r) = \frac{dV}{d\ln r}, \tag{2.26}$$

representing the aerosol volume in an air column of unity cross section per logarithmic particle radius unit. The total number of particles (or mass or volume) is obtained integrating between the minimum and maximum particle radius.

$$N = \int_{\min}^{\max} n(r) d\ln r \,. \tag{2.27}$$

Considering spherical particles, volume and number distributions can be related using the following expression:

$$v(r) = \frac{dV}{d\ln r} = \frac{4\pi}{3} r^3 \frac{dN}{d\ln r} \,. \tag{2.28}$$

It has been observed that size distributions measured in the atmosphere present certain rules, and this allows their modeling. The general approach is to represent these size distributions using a mathematical expression with some fitting parameters retrieved by the measurements.

At the present time, it is an open problem to clarify the number of parameters necessary to define the radiative characteristics of the aerosol and which one can be obtained with accuracy using only the measurements. A good representation for the aerosol, specially the smaller particles, in clean and polluted areas, is the log-normal distribution function (Hegg et al., 1993):

$$v(r) = \frac{dV}{d\ln r} = \frac{V_0}{\sigma\sqrt{2\pi}} \exp\left[-\frac{\ln^2(r/r_m)}{2\sigma^2} \right] . \tag{2.29}$$

Similar functions can describe mass and number size distributions. In this function, r_m and σ are the adjustable parameters, V_0 represent the volume of particles in an air column of unity cross section. The standard deviation of the logarithm of the radii σ represents the width of the size distribution. The median radius of the particles r_m provides the position of the maximum in the curve of the distribution.

Atmospheric aerosol size distribution can be represented with the sum of three log-normal distributions, called modes (see figure 2.9), building a multimodal size distribution function. Both modeling of the actual distribution show a good agreement in the range of radii of interest.

Besides the shape, content and size distribution, another physical property that characterizes the aerosol, related to its chemical composition, is the refractive index expressed by the complex number $m = n - ki$. This magnitude is wavelength dependant. The real part of the refractive index n determines the scattering of the incident wave. It varies from 1.33 for pure water to 1.77 for soot. The greater the index, the larger the effect of the particle on the incident radiation. The imaginary part k determines the ability of the particle to absorb radiation. Larger values mean more absorption capability. This value varies from 0 for non absorbent particles as marine salt, to 0.4 for soot (D'Almeida et al., 1991).

3

Sites description

This work has been carried on mainly in Granada (Spain) although some of the instruments were operated at the Southern Great Plains in the United States. This chapter describes the sites where the instruments gathered the data used in this work.

3.1 Granada

The station of the Atmospheric Physics Group (Grupo de Física de la Atmósfera, GFAT) is located at Granada (Spain) on the rooftop of the Andalusian Center for Environmental Studies building (Centro Andaluz de Medio Ambiente, CEAMA) at 37.16ºN latitude, 3.6ºW longitude and 680 m a.s.l. The station records meteorological and radiometric information. Instruments such as broadband radiometers (ultraviolet, visible and infrared), UV spectroradiometer (Bentham DMc-150) and sun photometers (CIMEL CE318) are continuously gathering data. The records are complemented with meteorological parameters at ground level such as atmospheric pressure, wind, temperature and humidity.

Granada is a non-industrialized medium-sized city in southeastern Spain. It is situated in a natural basin surrounded by mountains. Semicontinental conditions prevailing at this site are responsible for large seasonal temperature differences, with cold winters and hot summers. The area also experiences periods of low humidity. Most rainfall occurs during spring- and wintertime. The summer is normally very dry, with few rainfall events in July and August (anon., guia clima 1995). Annually, 31.15% of the days in Granada have clear sky days (0 oktas), 46.44% cloudy (1 – 7 oktas), and 22.4% overcast (8 oktas), according to climatology over the period 1961-1990 (anon., guia clima 1995). The region also experiences dust outbreaks that carry important loads of mineral aerosol coming from the Sahara desert. These events are especially

common in summertime (Lyamani et al, 2005; Guerrero-Rascado et al., 2009).

A map of the area of the CEAMA station is shown in figure 3.1

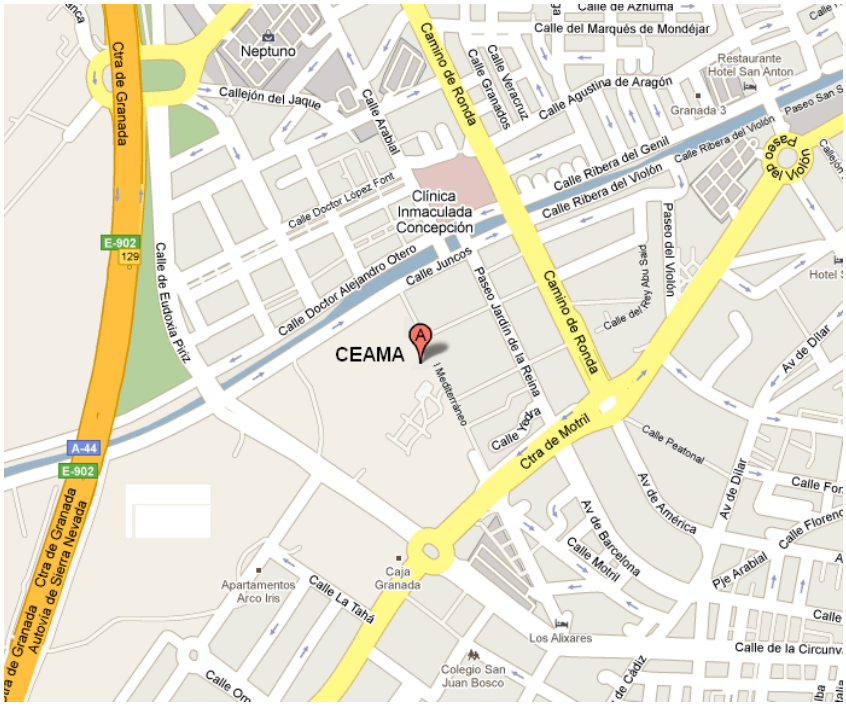

Figure 3.1. CEAMA station map

The All-Sky Imager and the radiometer CIMEL CE318, described in the next chapter, are located in the station.

3.2 Southern Great Plains

Part of this work is the result of a research stay at the Atmospheric Optics Group (AOG) in the Marine Physical Laboratory, Scripps Institution of Oceanography, University of California San Diego. This group has been researching and developing sky imagers for decades (Johnson et al., 1989; Shields et al., 1993; Shields et al., 1998). They have different sky imagers in different locations. The WSI used in this work was located in the Southern Great Plain (SGP) in the United States during 2000 – 2004 (an earlier WSI was at the site from 1995 – 2000).

The SGP site was the first field measurement site established by the Department of Energy's (DOE) Atmospheric Radiation Measurement (ARM) Program (www.arm.gov). Scientists are using the information obtained from the SGP to improve cloud and radiative models and parameterizations and, thereby, the performance of atmospheric general circulation models used for climate research.

The SGP was chosen as the first ARM field measurement site for several reasons including its relatively homogeneous geography and easy accessibility, wide variability of climate cloud type and surface flux properties, and large seasonal variation in temperature and specific humidity.

The SGP site consists of in situ and remote-sensing instrument clusters arrayed across approximately 55,000 square

miles (143,000 square kilometers) in north-central Oklahoma. Figure 3.2 shows a map of the facility.

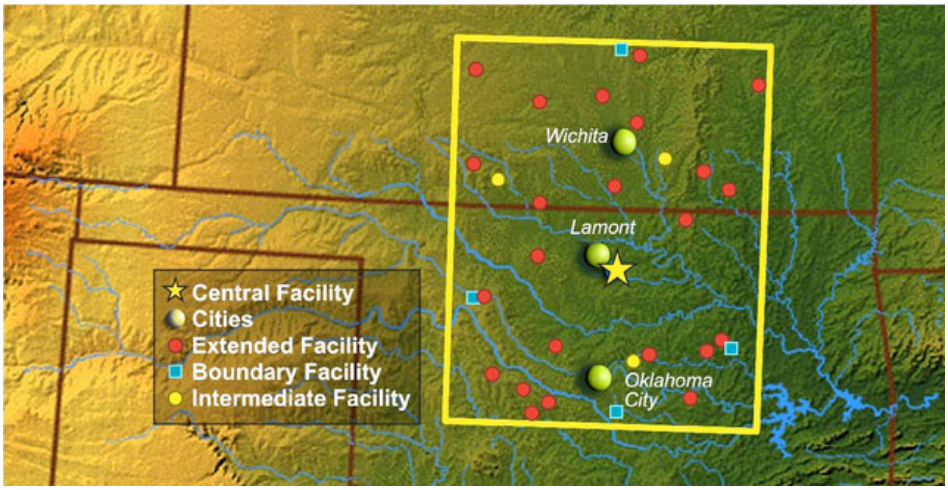

Figure 3.2. SGP facility map

The central facility is a heavily instrumented location on 160 acres of cattle pasture and wheat fields southeast of Lamont, Oklahoma (36.61°N, 97.5°W, 320 m a.s.l.). More than 30 instrument clusters have been placed around the SGP site, at the Central Facility and at Boundary, Extended, and Intermediate Facilities. The locations for the instruments were chosen so that the measurements reflect conditions over the typical distribution of land uses within the site.

Both instruments, the CIMEL CE318 and the WSI are located in the central facility.

4

Instrumentation

This chapter presents the two imagers used in this work and the sun photometer CIMEL CE318. The main core of this work involved the development of the All-Sky Imager described in section 4.1.1. This work also used the calibrated Whole Sky Imager, described in section 4.1.2, as collaboration between the Atmospheric Physics Group from University of Granada and the Atmospheric Optics Group from University of California at San Diego, where this instrument has been designed and developed.

4.1 Sky Imagery

In recent years, atmospheric researchers have become increasingly interested in quantifying clouds. As we saw in section 1.1, clouds are a major meteorological phenomena related to the hydrological cycle and affect the energy balance on both local and global scales through interaction with solar and terrestrial radiation. Clouds, and cloud-aerosol interaction, are responsible for the largest uncertainties in climate model (Houghton et al., 2001). In addition, clouds affect our everyday lives, for example modifying the amount of ultraviolet radiation that reaches the earth's surface. Most cloud-related studies require some sort of cloud observations, such as the amount and type of clouds that are present. These macrophysical observations have been performed historically by human observers who recorded cloud cover and cloud type at several meteorological stations and at given time intervals, typically hourly at many US sites and most of the Spanish meteorological stations, 3 hourly at many other sites worldwide (Long et al., 2006). However, high costs associated with human observers have led to the research of observations based on automatic devices to detect and quantify cloud amount and type. Satellite retrievals have known weaknesses in quantifying small and/or low cloud features due to their limited spatial resolution and undesired surface influences on the measured radiances. Other option for obtaining continuous information on sky conditions is the use of sky imagers (Long et al., 2006).

There have been numerous instruments and techniques developed to automate the measurement of the cloud properties in the last three decades but it was until recently, the last decade, when these instruments began to experiment some success on fully automate the ground-based measurement of cloud properties, typically the cloud area. Sabburg (2000) and Parisi et al. (2004) presented overviews on the different sky imagers developed until recently. Here is a summary.

Borkowski et al. (1977) used a standard 35 mm camera with telephoto lens. The lens was located above a hemispherical reflector. Processed negatives of the whole-sky were projected onto a grid made of concentric circles and radial lines. Cloud area was measured by manually counting the number of intersections covered by clouds on the grid. Wooldridge (1993), and Wooldridge and Hayman (1994) also analyzed 35 mm whole-sky negatives for cloud area. They considered the grid design and cloud retrieval methodology and recommended using an equal area grid and a cloud presence/absence scale.

The application of computer vision to sky imagers has become possible due to the rapid increase in camera technology. For example, McKenzie et al. (1998) attempted to use a video camera, developed by Harnett (1992), to study the effect of cloud area on UV radiation. However, restrictions of lack of color and the necessity of shading the camera from direct sunlight limited its suitability. Schafer et al. (1996) employed a ground based whole-sky video camera to study cloud effects on UV radiation. However, due

to lack of suitable digital image processing (DIP) software, they estimated solar obstruction by cloud and cloud area from the images by manual inspection.

DIP began in the 1960s and revolutionized the analysis of aerial photographs (Lillesand and Kiefer, 1994). When DIP was applied to analyzing satellite and ground based sky camera images, the full automation of the measurement of cloud properties was realized. For example, Wooldridge (1993) and Platt et al. (1994) describe the development and evaluation of an automated, whole-sky, video camera system, incorporating DIP. The system estimated cloud area, optical thickness and the velocity of clouds from one image to the next. The methodology was promising when illuminance levels were high enough to provide quality digital images. However, sky conditions for mid range cloud area was poorly retrieved. Also, Long and DeLuisi (1998) describe the development of an automated whole-sky camera system using DIP. The system is essentially a digital form of the sky imager developed by Borkowski et al. (1977). This design by Long and DeLuisi was later improved and commercialize by the company Yes Inc. under the name of Total Sky Imager (TSI) that is described deeper by e.g. Long et al. (2006).

Other sky imagers do not provide a full hemispherical field of view. Sabburg (2000) developed a sun-centered sky camera (SCSC). The system located the position of the sun in the sky images, evaluated the sun obstruction by clouds and then digitally eliminated the sun disc from the images for further analysis. Finally,

a new set of sky properties based on the cloud distribution on the sun vicinity. Thus, they extracted properties as solar disk obstruction, cloud cover, aureole brightness, cloud brokenness, cloud brightness variation and angle of maximum cloud cover. The main limitation of this method is the field of view of the system. Also, Sabburg and Long (2004) proposed a model of the enhancement of UVB due to clouds using parameters from the analysis of images from the TSI.

The Environmental Physics Group at University of Girona developed a sky imager that is described by Long et al. (2006). The system consists on a video camera with a fish eye lens. They recently developed a new sky imager placed in a sun tracker. This system presents similarities to the All Sky Imager described in section 4.1.1.

On the other hand, Shields et al. (1998) developed a sky imager combining a fish eye lens with narrow band filters. This sky imager also operates at night and retrieves the sky radiance in all directions of the sky, as we will see in section 4.1.2.

4.1.1 All-Sky Imager

4.1.1.1 Design, development and features

There are advantages on developing specific-purpose imagers; for example, the user has a detailed knowledge of the prototype system and can choose components that best suit a

specific task. However, this development process requires knowledge of detectors and optical systems, as well as development of the interface algorithms needed to construct actual images in a format using the readings of the detector array (Long et al., 2006). In the GFAT we decided to develop a sky imager, so we have fully control of the components, algorithms and operation schema.

The original idea behind the sky imager is to provide images of the whole sky dome during daytime for cloud cover characterization. The problem with sky imagery from the ground is that there are very bright region (e.g. close to the Sun) and other darker regions. The sky imager has to capture details all the image regions at the same time since we need information about the clouds in each pixel of the image. Moreover, Sun direct irradiation cannot strike the CCD to prevent stray light and a possible blooming of the sensor.

Our All-Sky Imager is a custom adaptation of a scientific CCD camera. The principal modifications are the lens, the environmental housing and the solar shadow system.

The camera body is a color CCD sensor by QImaging (RETIGA 1300C). It provides full color images (1280 x 1020 pixels) with three channels: one centered in red wavelengths, another centered in the green and the last one centered in the blue. The CCD sensor has 12-bit digitization per channel and therefore, the final image has 36-bit digitization and 4096 counts per channel. These characteristics offer a higher dynamic range than

conventional CCD cameras and allow better discrimination for details in images with very dark or bright areas with the same exposure time. A peltier cell coupled to the CCD cools it to 25º C below ambient in order to reduce dark noise. Table 4.1 shows the main characteristics of the CCD sensor as provided by the manufacturer.

Sensor type	2/3" color CCD (bayer mosaic)
Light sensitive pixels	1280x1024 (1.3 mega-pixels)
Pixel size	6.7μm x 6.7μm
Readout noise	8 e^-
Dark current	0.15 e^-/píxel/s
Quantum efficiency	400nm 30%; 500nm 43%; 600nm 30%
Digital output	12-bit
Integration time	40 μs to 15 min. in 1μs increments
Shutter control	Electronic shutter
Gain and Offset control	0 to 10x optimum gain
Optical interface	C-mount, 2/3" optical format
Digital/Electrical Interface	FireWire 1394 interface
Power requirements	900mA at 12V (11W)

Tabla 4.1. CCDsensor specifications

The lens is a Fujinon CCTV fish eye lens developed for a 2/3 inches format megapixel color CCD with C-mount. The field of view is 185º. This configuration guarantees a 180º field of view projected onto the CCD, and therefore the image captured shows the whole sky dome. The optical data sheet provided by manufacturer (FUJINON TV Lens, Optical Data Reports,

FE185C057HA) indicates that there is no longitudinal or lateral chromatic aberration and that the angular distortion in less than 0.8% at every angle between 0 and 180º (Table 4.2). Since the distortion is so low, no correction is applied to the images.

Half angle of view (degrees)	Angular distortion (%)
92.51	-0.80
82.55	0.05
73.15	0.36
63.96	0.43
54.85	0.39
45.75	0.30
36.63	0.20
27.50	0.12
18.34	0.05
9.18	0.01

Table 4.2. Angular distortion per angle. It is calculated from 0 to 90º and extrapolated to 180º.

An environmental housing built by the GFAT protects the All-Sky Imager from the rain, snow, and extreme temperatures on the rooftop. The housing has a transparent acrylic dome on the top, and the walls have two layers with polyurethane foam in the middle for thermal isolation. The thermoelectric regulator, a Peltier system by Supercool, controls the temperature inside the housing. The temperature controller configures the Peltier as a cooler or heater as necessary and maintains the same temperature, 25ºC,

inside the housing under most conditions. Figure 4.1 shows a schematic diagram of the All-Sky Imager.

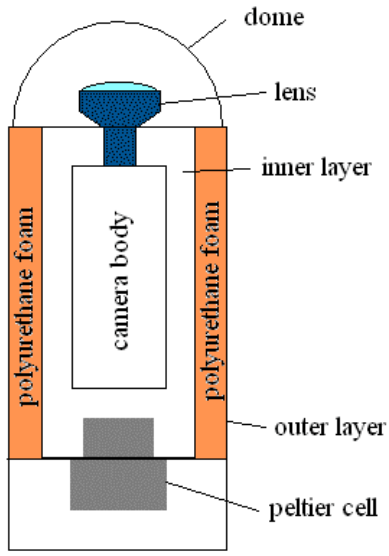

Figure 4.1. Schematic diagram of the All-Sky Imager

The solar shadow system must protect the lens, and consequently the CCD, at every moment from the direct irradiation of the Sun. The 2AP Sun Tracker/Positioner from Kipp & Zonen follows the Sun and projects the shade of three spheres onto a tray. The original function of the Sun Tracker is to shadow three radiometers, but it has been adapted for the All-Sky Imager. The Sun Tracker shades the All-Sky Imager, which is placed in the middle tray. Figure 4.2 shows the final configuration of the All Sky Imager placed in the 2AP Sun Tracker.

Figure 4.2. Final configuration of the All-Sky Imager placed in the Sun Tracker

4.1.1.2 Control software

The All-Sky Imager system includes control software that automates the image acquisition and analyses them for cloud characterization. The original software provided by the manufacturer of the CCD camera did not suffice for our needs, and thus new software has been developed.

The CCD sensor manufacturer supplies an application program interface (API) to program specific applications in C/C++. The control software has been developed to obtain color images from the pixel matrix of the CCD sensor. Each pixel is sensitive to one color (red, green or blue); the pattern that the sensor follows is

called bayer mosaic (Figure 4.3). As we can see, each 4 pixels (2x2) have the information of the three channels. It has one pixel for red, one pixel for blue and two pixels for green. Thus, the nominal resolution is 640x512 in the green and 320x256 in the red and blue. The information about the other channels for each pixel is retrieved by interpolation of the neighbor pixels providing a full resolution image (1280 x 1024 pixels) with the three channels.

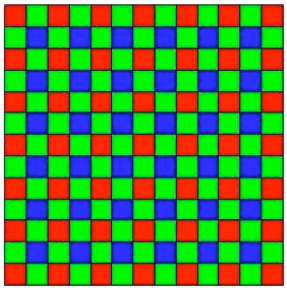

Figure 4.3. Bayer Mosaic

The new control software allows setting the camera parameters such as exposure time, gain, and offset. It is possible to change between 8 and 12 bit digitization (it is always set as 12), and the CCD Peltier cell can be connected or not. The control software has a timer and takes pictures with a specified time interval during daytime only. This time interval is set to 5 minutes as a compromise between short intervals that require large storage space and long intervals where useful information would be lost. All the images

with solar zenithal angle less than or equal to 80º are stored in the computer.

The data acquisition software changes the format of the original full resolution image (1280x1024 pixels) to a 900 x 900 pixels image that covers the useful area. By extracting this region, we reduce the size of the images, which is important because of the massive amount of data stored in the computer. Then, images are saved in the computer in TIFF format. This format is selected to enable storage of 12-bit images in lossless format. The images represent the whole sky dome, and the useful area of the image is circular, where the center of the image is the zenith and the horizon is along the border of the circle (spherical projection) as it can be seen in Figure 4.4.

Figure 4.4. Image captured with the All-Sky Imager

Along with the images, the software stores the settings for every image as well as an event log (setting changes, malfunctions, etc.). Figure 4.5 shows a capture of the control software.

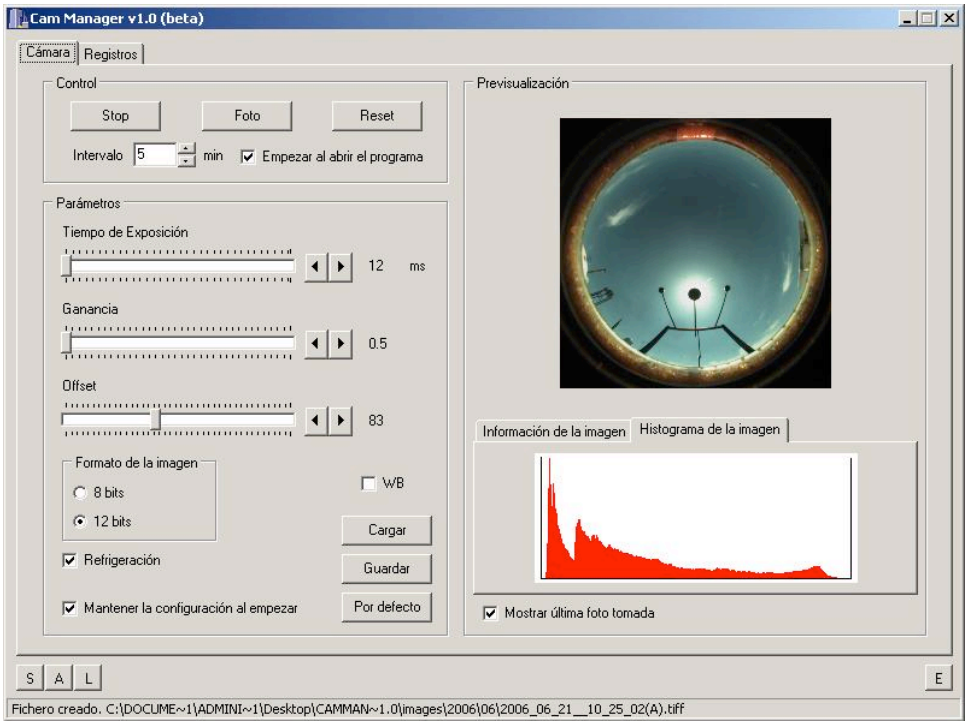

Figure 4.5. Control software of the All-Sky Imager

After the deployment of the All-Sky Imager we estimated the optimal parameters and kept them fixed. This is done using the histogram of the image. The histogram presents the tonal distribution of an image, i.e. represents the frequency of every possible value a pixel can take (0 to 4096 in a 12-bit CCD). The

parameters have to be adjusted in a way that the histogram does not have pixels at 0 (underexposed) or at 4096 (overexposed) for all of the possible images and it has to have a gaussian shape (tested over several days at different solar zenith angles). After trying different configurations the exposure time was set to 12 ms, the gain was set to 0.5 and the offset was set to 83.

4.1.1.3 Geometric calibration

In order to obtain an atmospheric aerosol characterization we will see in chapter 6 that it is necessary to locate the principal plane of the images. This plane is perpendicular to the image plane. Thus, in the projection of the sky onto the image this plane is a line and is easily found. The All-Sky Imager is placed on a sun tracker and the whole system follows the sun therefore, the principal plane in the image is the line that crosses the image vertically. However, the placement of the All-Sky Imager in the sun tracker is not perfect and so, this line can be displaced some pixels.

A simple method allows obtaining the correct placement of the principal plane in the images. First, we mark a 10° step ruler in an acrylic dome where 0° is the zenith and 90° is the horizon. Then, the dome is placed in the place of the original protection dome. The line is aligned with the sun tracker's shadow system. Figure 4.6 shows a sky image with the calibration dome in place.

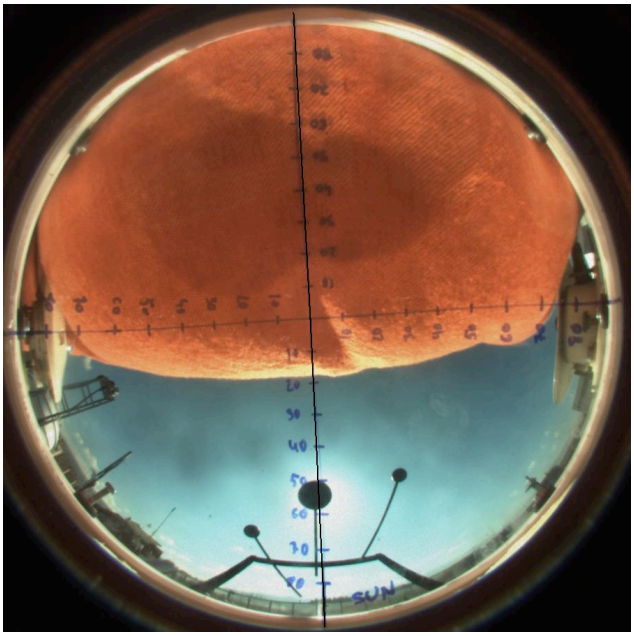

Figure 4.6. Sky image with the calibration dome in place. The orange blanket was placed to facilitate the visualization of the marks. Note that the vertical ruler is aligned with the sun tracker shadow system.

Once the image is captured each mark is associated with its pixel coordinates. A linear model can be applied to the X and Y coordinates of the images and the corresponding equations allow finding the pixel coordinates of a specific zenithal angle.

The maximum absolute error is calculated to be ±5 pixels horizontally and ±1 pixel vertically and each pixel is 0.21° in size (field of view of the pixel). Finally the equations for the model are:

$$P_X = -4.69\theta + 450.7\,, \tag{4.1}$$

$$P_Y = -0.246\theta + 439.3\,. \tag{4.2}$$

Figures 4.7 and 4.8 shows the correlation between pixels coordinates and zenithal angle and the equations for the model.

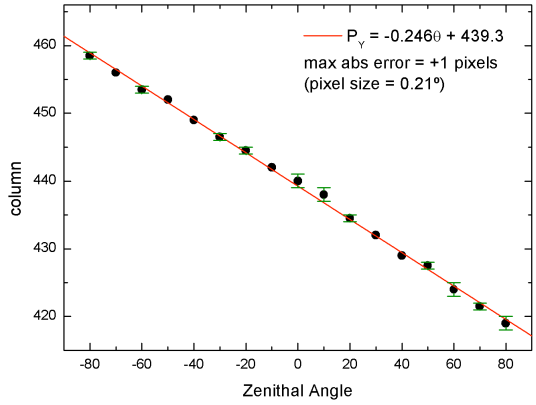

Figure 4.7. Pixel Y coordinate (row) versus zenithal angle

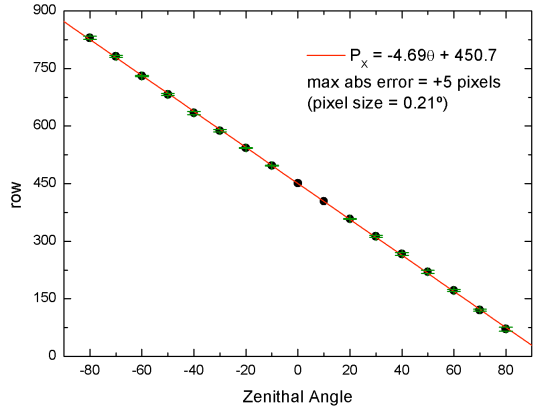

Figure 4.8. Pixel X coordinate (column) versus zenithal angle

4.1.2 Whole Sky Imager

4.1.2.1 Features

The Atmospheric Optics Group (AOG), at the Scripps Institution of Oceanography, has been very active in the development of digital sky imagers for two decades. The original concept for the WSI evolved from a measurement and modeling program using multiple sensors for monitoring sky radiance, atmospheric scattering coefficient profiles and other parameters related to vision through the atmosphere (Johnson et al., 1980; Johnson et al., 1989). In particular, the first automated WSI was conceived as combining the features of the all-sky camera with a scanning radiometer system that provided quantitative measurements of sky radiance distribution. Early systems were based on digital cameras, with fisheye lenses, optical filter changers, relay optics to provide the proper image size and location, equatorial sun occultors to provide shading for the lens, and early versions of personal computers for automated control. With the use of very low noise 16-bit CCD cameras and an occultor modified to handle both sun and moon, these systems were further developed into the Day/Night WSI (Shields et al., 1998).

The Day/Night WSI is a 16-bit digital imaging system that acquires images of the full sky (180º FOV) under both day and night conditions in order to assess cloud fraction, cloud morphology, and radiance distribution. The WSI measures the sky radiance in approximately 185,000 directions simultaneously by

using a 512x512 CCD sensor. The result is a 0.35° field of view in each direction, to cover the full 180º dome. Images are acquired in visible and near infrared (NIR) wavebands with filters at 450 nm (blue), 650 nm (red), and 800 nm (NIR) under sunlight or moonlight. The full width at half maximum (FWHM) of the filters is 70 nm. An open hole visible filter is used under starlight. The image acquisition interval is user selected, with intervals such as 1 minute or 10 minutes between image sets. A picture of the instrument fielded at the Oklahoma Cloud and Radiation Testbed (CART) site at SGP is shown in figure 4.9. The primary features seen in this figure are the environmental housing that protects the sensor and electronics, the optical dome, and the solar occultor that shades the optics. Figure 4.10 shows a daytime image.

Figure 4.9. Day/Night WSI fielded at SGP CART site

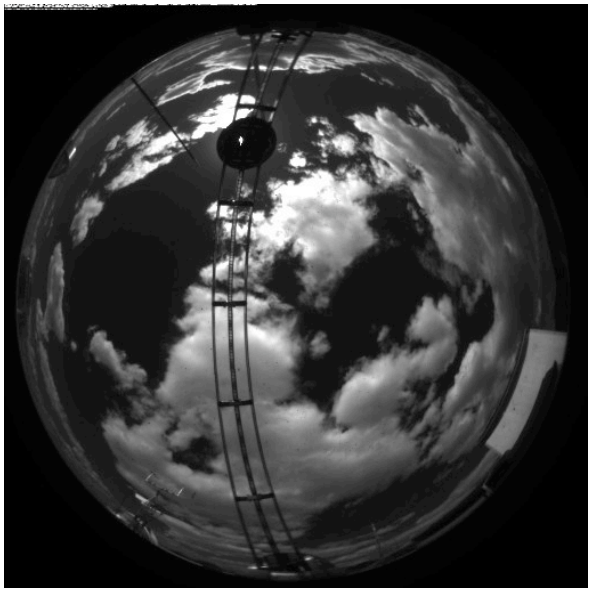

Figure 4.10. Raw red image. The edge is the horizon and the center is the zenith. The arc is the shadow system.

The primary optical element is a fisheye lens with a 181° field of view (FOV). The light is filtered by spectral and neutral density filters, and transferred via a tapered fiber optic bundle (with approximately 10^6 optical fibers) to the CCD.

The CCD camera, provided by Photometrics, is a very low noise 16-bit camera. Typical instrument noise (readout and dark current noise) is approximately 0.1% of the signal in the daytime. At night, under the darkest conditions with no moon at a 1-minute exposure, instrumental noise is approximately 1% of the signal of the background sky between stars, and a much lower fraction of the

star radiance signal. The camera in combination with the filter and exposure selection by the system, yield a dynamic range about 10^{10}. That is, radiance can be measured from approximately 3 10^{-7} to 7 10^{2} (red) or 6 10^{3} (blue) W m^{-2} μm^{-1} sr^{-1}.

A PC-based controller controls the system, with electronics developed at the AOG for manual or automated control. Algorithms programmed into the instrument provide flux control to keep data on scale even during quickly changing times such as sunrise and sunset.

The environmental housing seen in figure 4.9 is designed to keep the camera and electronics cool. Self-diagnostic indicators such as readouts of CCD temperature, housing temperature, and coolant flow rate are also included in this housing. The arc seen in figure 4.9 provides shading for the optical system. Even though the camera would not be damaged by direct sun radiation, this shading is desirable because it minimizes stray light especially near the sun.

4.1.2.2 Absolute radiance calibration

One of the capabilities of the WSI is the determination of the absolute radiance distribution. The fisheye lens directs the light from different directions onto different pixels in the image plane, and the signal of each pixel may be calibrated to yield a determination of the absolute radiance, in W m^{-2} μm^{-1} sr^{-1}, in that

direction. The FOV for each pixel is approximately 0.35º. Thus, this radiance product is equivalent conceptually to a radiance distribution determined by a scanning radiometer, except that all radiances are acquired simultaneously (at 185,000 points) and at a very high spatial resolution.

The overall sensitivity is determined by the lens, the transmittance of the various filters, the throughput of the optical fiber bundle, and the quantum efficiency of the CCD chip. The calibration process has different stages (Shields et al., 1998).

First of all the spectral sensitivity of the chip and transmittance of filters are measured. These spectral curves are used in conjunction with the calibration lamp spectral irradiance to compute the effective lamp irradiance in the filter passbands used by the WSI. These effective irradiances are in turn an input to the processing of the absolute calibrations.

Dark calibration characterizes the pixel-to-pixel variations of the zero signal (no light) offset. A dark image, i.e. with the shutter closed, is taken every time the exposure is changed.

Flat Field calibration characterizes the pixel-to-pixel variation in the system gain. During the calibration process the WSI is placed inside an integrating sphere. Several images are taken and processed to determine the uniformity. As a result we obtain a flat field image and a normalization constant.

Linearity characterizes the relative system response to changing exposure and changing light levels. There is a finite shutter opening time and shutter delays, and corrections are made for these when the images are acquired. The system is linear with respect to changing light levels to better than 0.5% over most of its range, hence no linearity correction is currently applied.

Off-axis rolloff determines the off-axis effects of optical fresnel losses and solid angle per pixel changes. This correction is determined imaging a source changing the zenith angle. The resulting correcting is a function of the relative power of the source as a function of the zenith angle.

Finally, absolute radiance calibration determines the absolute radiance as a function of the exposure time and filter selection. Several redundant measurements are taken in each filter combination (spectral and neutral density filter). The computed calibration constants *CC* are the absolute radiance for each filter combination that will yield a signal of 10,000 counts (dark-corrected) at an exposure of 100 ms.

The equation to calibrate an image is as follows.

$$C_p = (R_p - D_p)\frac{FFNorm}{FF_p}Ro_p\frac{100}{Expos}\frac{CC}{10000}, \qquad (4.3)$$

where C_p is the radiance in the pixel, R_p is raw pixel signal value in the image (number of counts), D_p is the pixel value in the dark image, *FFNorm* is the flat field normalization constant, FF_p is the

pixel value in the flat field image, Ro_p is the pixel value in the rolloff image, *Expos* is the exposure time in ms and *CC* is the calibration constant of the filter combination used to acquire the image. Figure 4.11 shows a schematic chart of the calibration of an image.

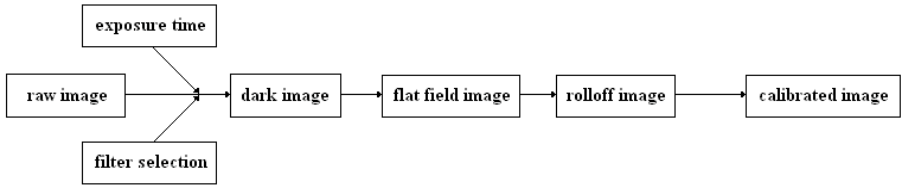

Figure 4.11. Schematic chart of the calibration of an image. Exposure and filter components are constants in the calibration process, the rest are images.

4.1.2.3 Geometric calibration

Geometric angular calibration characterizes zenith angle and azimuth angle in object space as a function of pixel in image space. The first step in the calibration is to provide an approximate calibration, accurate to approximately 2 pixels. In order to calibrate the WSI an image is taken in the calibration room where different marks have been placed on the wall from -90 to 90º. Image is centered to 0º zenithal angle and every mark is associated to a pixel in the image with visual inspection. Using a standard least squares method with matrix inversion a 3rd order polynomial fits of radius versus zenith angle is made for the data. The radius is forced to 0 when θ equals 0. The equation takes the form

$$radius = R_0(C_1\theta - C_2\theta^2 - C_3\theta^3), \tag{4.4}$$

where R_0 is the image radius of about 246 pixels.

Given the radius and azimuth angle, the x- and y-pixel coordinates are found using equations (4.5) and (4.6). x_{center} and y_{center} are the coordinates of the image center and radius is the value from equation (4.4)

$$x = x_{center} + Radius \times \sin(azimuth), \tag{4.5}$$

$$y = y_{center} + Radius \times \cos(azimuth). \tag{4.6}$$

After the instrument is fielded, a more precise geometric calibration is determined using the star field. This second calibration also takes into account the slight errors in leveling of the instrument and alignment with respect to true North. For this calibration, approximately 100 bright stars in the image are selected, and compare their actual position in the image with an anticipated position based on star libraries and the first level geometric calibration. In this process, the actual position is determined to sub-pixel accuracy by characterizing the Point Spread Function around the star. An iterative process is used to a modified high precision geometric calibration, typically accurate to about half a pixel. The high-resolution calibration takes the form:

$$\phi = C_1 + \phi_0 + C_2\rho Cos(\pi\phi_0/90) + C_3\rho Sin(\pi\phi_0/90), \tag{4.7}$$

$$\theta = C_4\rho + C_5\rho^2 + C_6\rho^3 + C_7\rho Cos(\pi\phi/90) + C_8\rho Sin(\pi\phi/90), \tag{4.8}$$

where

$$\phi_0 = \arctan\left[\frac{x - x_{center}}{y - y_{center}}\right] \tag{4.9}$$

and

$$\rho = \sqrt{(x - x_{center})^2 + (y - y_{center})^2} \tag{4.10}$$

This process was originally developed by Dr. Tim Tooman of the ARM program (personal correspondence with the AOG), and then further developed by the AOG.

4.2 Sun photometer CIMEL CE318

Sun-photometry is the most common way to characterize aerosol in daytime from the ground. First sun photometers were developed by Volz (1974) exploiting the new electric thermopiles and the development of the optics industry that produced the first spectral filters (Iqbal, 1983, Rollin, 2000). Volz's photometer included two spectral channels designed for the calculation of the solar constant and the measurement of atmospheric transmittance, and it is the precursor of the modern sun photometers. Advances in electronics brought substantial improvements in sun photometry (Forgan, 1994; Schmid et al., 1997; Holben et al., 1998; Morys et al., 2001), but the design of the instruments have not changed a lot since Volz's photometer (Holben

et al., 1998; Estellés, 2006). These new developments are basically, more sensitive, accurate and stable.

The development of interferential filters has a vital importance for sun photometry. Characteristics of these filters, determined by their slit functions, define the spectral selectivity of the measurements. It is fundamental in the design of a photometer the selection of the central wavelength and width of the filters that define the channels of the instrument. There are several wavelengths recommended by the WMO (Shaw, 1983). They are in the so-called spectral windows, where there is no strong absorption by gases so the effect of atmospheric aerosol is isolated. It is also common to include specific absorption bands to characterize a specific gas component (typically water vapor and ozone).

4.2.1 Description

The design of the sun photometer CIMEL CE318 consists on an optical head with two collimators, a robotic arm for sun tracking and sky positioning and an electronic box (http://www.cimel.fr).

The optical head includes the sensors and the optics for the measurements. It has attached a double collimator with a field of view of 1.2º for the direct irradiance measurements, solar aureole (about 6º around the sun) and sky radiance in the almucantar plane (fixing the solar zenithal angle and varying the

azimuth angle) and the principal plane (fixing the solar azimuth angle and varying zenithal angle). The interferential filters select the measurement channels. These filters are placed in a filter wheel and one of the positions is blind for noise measurement. The wavelengths of the instrument are centered on 340, 380, 440, 670, 870, 936 and 1020 nm. The 936 nm channel is used for precipitable water content calculation; the others are used for the characterization of the optical and microphysical properties of the atmospheric aerosol. The FWHM of the filters are 2 nm for the 340 nm filter, 4 nm for the 380 nm filter and 10 nm for the rest. The slit function of the filters is Gaussian. Finally, the detectors are silicon photodiodes.

The robotic arm moves the optical head pointing to the sun for the direct irradiance measurements and it also move the head for the almucantar and principal plane measurements (figure 4.12).

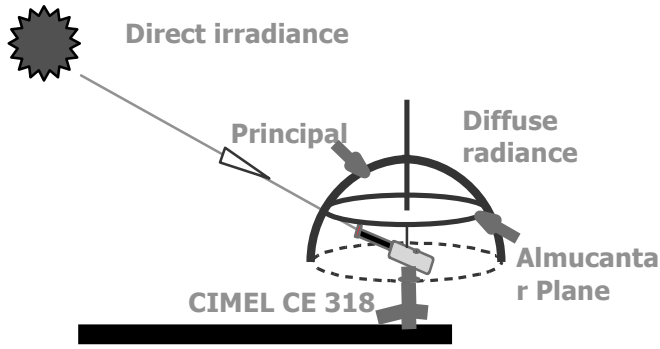

Figure 4.12: Measurements schema for direct irradiance and almucantar and principal planes.

The electronic box includes the necessary electronics for the function of the robotic arm and the optical head. These electronics can be programmed and the system works automatically following certain protocols established. It can also operate manually. The box also includes the batteries, a solar panel, a humidity sensor and the data transmission system. Figure 4.13 shows the CIMEL CE318.

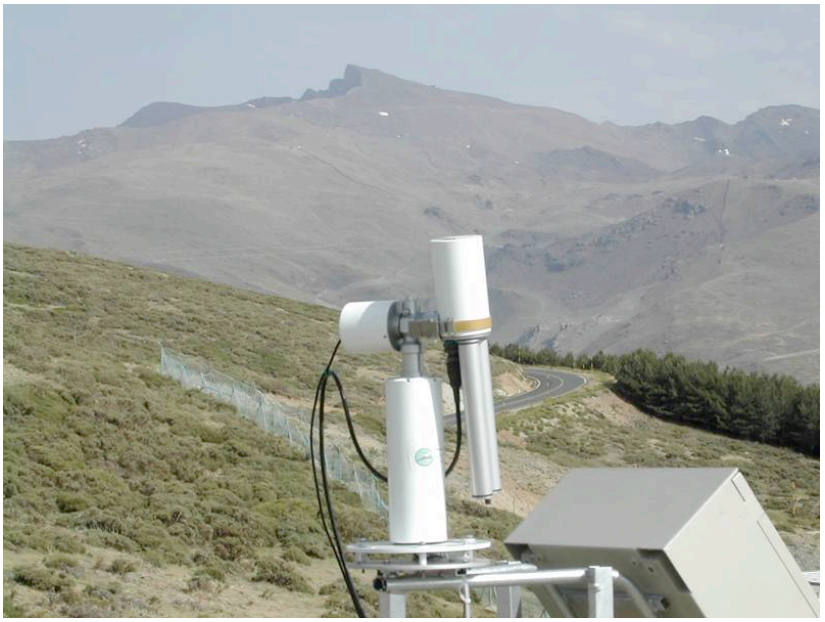

Figure 4.13. A Cimel CE 318 fielded in Sierra Nevada (Granada, Spain)

4.2.2 Measurements schema

Filters at 340, 380, 440, 670, 870, 937 and 1020 nm are used for the direct irradiance measurements. It takes 10 seconds to measure with all the filters. This is repeated three times at 30 seconds interval to form three measurements per channel (triplet). The triplet is used for the cloud screening (Holben et al., 1998; Smirnov et al., 2001). On the other hand the measurement sequence is defined according the relative optical mass. When the optical mass is less than 2, the triplet is measured every 15 minutes, when the optical mass is between 2 and 5, the triplet is measured at 0.25 optical mass intervals. Finally, when the optical mass is between 5 and 7, the triplet is measured at 0.5 optical mass intervals.

Filters at 440, 670, 870 and 1020 nm are used for the sky radiance measurements. Almucantar plane measurements start at the sun position and continue 360º in approximately 40 seconds per channel. Measurements are performed every hour between 9 a.m. and 3 p.m. in solar time and also when the optical mass is 4, 3, 2, and 1.7 in both, morning and afternoon. Principal plane measurements start 6º below the sun position and continue moving the optical head upwards taking approximately 30 seconds per channel. Measurements are performed every hour when the optical mass is below 2.

4.2.3 Sun photometer networks

Sun photometer CIMEL CE318 was developed in early 90s as collaboration between the company Cimel Electronique (Paris, France) and the Laboratorie d'Optique Atmosphérique (LOA) from l'Université des Sciences et Technologies de Lille (France). The first model became the standard instrument of the PHOTONS network (Photométrie por le Traitement Opérationnel de Normlization Satellitaire, http://www-loa.univ-lille1.fr/photons). In the mid 90s, NASA (National Aeronautic and Space Agency) in collaboration with PHOTONS created AERONET (Aerosol Robotic Network, http://aeronet.gsfc.nasa.gov) using the CIMEL CE318 as the standard instrument as well. CIMEL CE318 is also the standard instrument in other networks, for example AEROCAN (the Canadian sun photometer network, http://pages.usherbrooke.ca/aerocan) or the Spanish network RIMA (Red Iberica de medida de aerosoles, http://www.rima.uva.es).

AERONET is the wider network and pretends to obtain optical and microphysical properties of the atmospheric aerosol in order to validate satellite measurements and create a climatology of aerosol (Holben et al., 1998). It is composed by over 200 stations distributed all over the world (figure 4.14) covering all kind of aerosol, anthropogenic and natural.

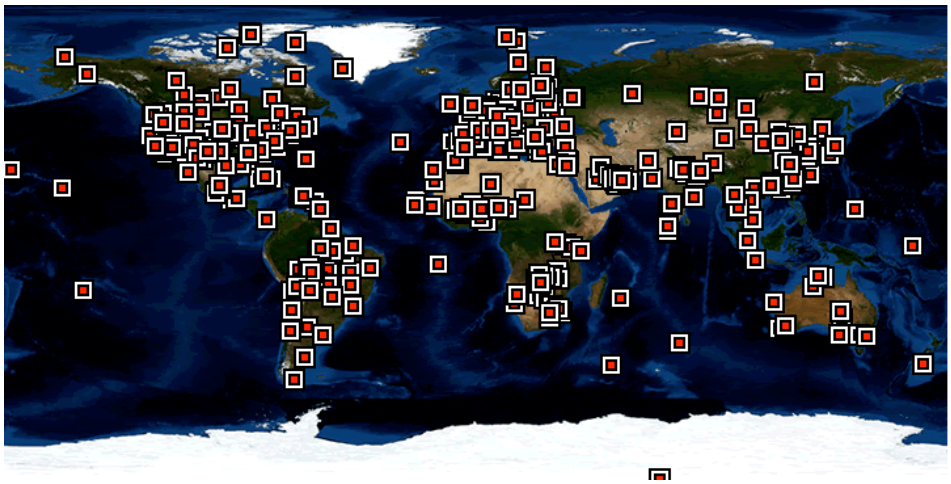

Figure 4.14: Distribution of the AERONET stations over the world (image from http://aeronet.gsfc.nasa.gov)

AERONET provides data almost in real time, but there are three levels in the processing of the data. AOD data are computed for three data quality levels: Level 1.0 (unscreened), Level 1.5 (cloud-screened), and Level 2.0 (cloud screened and quality-assured). Inversions, precipitable water, and other AOD-dependent products are derived from these levels and may implement additional quality checks following the procedures developed by Dubovik et al. (2002; 2006).

The instruments used in this work are two Cimel CE318, one of them from the GFAT sited on the rooftop of the CEAMA) in Granada (Spain) and the other one from the ARM sited in the SGP, in Oklahoma, United States. The first one operates in AERONET since 2004 but it also uses algorithms developed in the

GFAT for the inversions (Olmo et al, 2006; 2008). The second one operates in AERONET since 1994.

5

Cloud cover characterization

In this chapter we present the technique for cloud cover estimation applied to the All-Sky Imager. First, we will see the traditional algorithms more widely applied and the new approach that we propose. This approach with neural networks and genetic algorithms requires a brief introduction to these techniques. Then, we proceed with the design of the algorithms and the final procedure and finally, the results and evaluation of the process.

5.1 Introduction

In section 4.1 we saw that the development of sky imagers increased drastically due to the dramatic improvements in technology in recent years, both with respect to the hardware and digital image processing (DIP).

DIP is based on the fundamental steps of image acquisition, noise removal, feature extraction, recognition and knowledge (Gonzalez and Woods, 1992). Goodman and Henderson-Sellers (1988) reviewed the major types of DIP algorithms used for analyzing satellite images for cloud properties and grouped these into three classes. These classes consisted of thresholds, radiative transfer and statistical procedures, and example applications are described by Chou (1991), Ebert (1992), Romanov (1994) and Chen and Takagi (1994). Nevertheless, Goodman and Henderson-Sellers (1988) pointed out that ground-based observations of cloud area are different from satellite-based retrieval because of the difference in viewing geometry. They established this difference in about ±1 okta.

Thresholds and radiative transfer procedures have also been applied to ground-based sky image processing. A method based on the threshold of the ratio between the red and blue channels of the images has been widely used. This method was developed by the AOG for the WSI (Johnson et al., 1989). A limit or threshold is set for a clear-sky ratio value for each pixel in the image, and the pixels for which the red/blue ratio exceeds the clear

limit are counted as cloudy. It must be noted that the particular threshold function is climate and camera dependent. In addition, how white tinted the blue of the sky appears, which is considered to be cloud free, relates to such factors as the typical aerosol loading at a given location. One way to account for these effects is to tailor the clear/cloud threshold specifically for a given camera and location (Long et al, 2006). This method, with different variation in the process of selecting the threshold, is applied to imagers such as the WSI, WSC and the TSI. Alternatively, there is a threshold method based on the hue-saturation-intensity color space (Souza-Echer et al., 2006).

In this work, we present a different way to approach the problem of cloud cover determination. We are considering this problem as a classification problem. Pixels of the images are classified into one of three different classes: clear sky, opaque cloud or thin cloud. The classification method applied is neural networks and the input selection is chosen by means of a genetic algorithm. Following sections describe the instruments for this method, i.e. the neural networks and the genetic algorithms, and then the procedure applied for the cloud cover determination.

5.2 Neural networks

An Artificial Neural Network (Lippman, 1987; Khanna, 1990; Bishop, 1995) is an information processing paradigm that is inspired by the way biological nervous systems, such as the

brain, process information. The key element of this paradigm is the novel structure of the information processing system. It is composed of a large number of highly interconnected processing elements (neurons) working in unison to solve specific problems. After a training (also called learning), the neural network is configured for a specific application, such as classification, pattern recognition, functional approximation, control system, etc. According to Haykin (1994) a neural network resembles the human brain in two aspects: the knowledge is acquired by the network through a learning process, and interneuron connection strengths known as synaptic weights are used to store the knowledge.

Neural networks have been widely used in atmospheric science recently, as Gutiérrez et al. (2004) reviewed. Some other examples developed in our research group (GFAT) are Alados et al. (2004); Gil et al. (2005) and Alados et al. (2007).

The Perceptron (Rosenblatt, 1961) is the elemental unit in a neural network and emulates a biological neuron. It has a set of inputs (dendrites in the biological neurons), a processing unit (soma or nucleus) and an output (axon). The inputs are weighted and the processing unit consists on the weighted sum of the inputs. The output is a function of that sum (transfer function) and is, typically, a linear, gaussian or sigmoidal function.

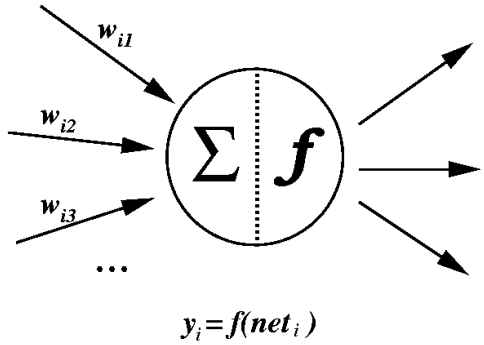

Figure 5.1. The perceptron

A set of perceptrons forms a neural network and the way this perceptrons are connected determine the kind of neural network.

Multilayer Percentron, described in the following section is an example of a neural network widely used for classification and pattern recognition.

5.2.1 Multilayer Perceptron

Multilayer perceptron (Rumerlhart et al., 1986; Barber and Bishop, 1997) has been used widely for classification and the training algorithms has been studied and tried numerous times. Moreover, the topology is very simple.

The topology of the multilayer perceptron requires determining the number of layers and the number or neurons per

layer. The first layer is called input layer and the number of neurons is determined by the input parameters and their codification (this is called pattern or prototype). The last layer is the output layer and the number of neurons is defined by the output of the system. In the case of classification it could be, for example, one neuron per class. Layers between the input and output are the hidden layers. The number or hidden layers and the number or neurons per hidden layer depend on the problem and requires trying different possibilities. Connections between neurons in a multilayer perceptron are always feed-forward, i.e. each neuron in one layer is only connected to all the neurons in the following layer except the last layer that gives the final output. Figure 5.2 shows a schematic draw of the topology of the multilayer perceptron.

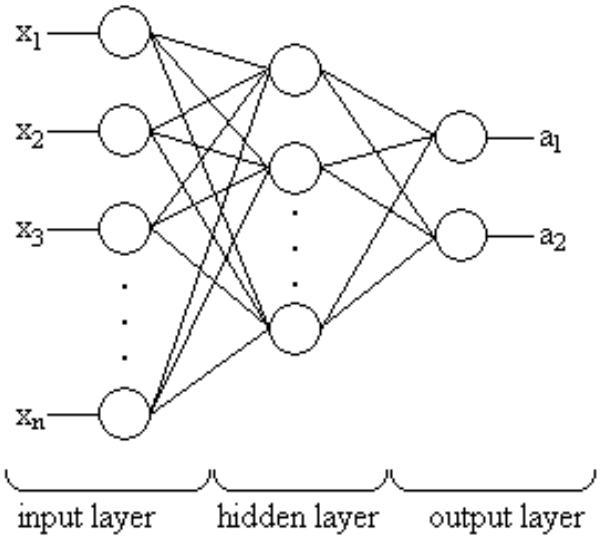

Figure 5.2. Topology of the multilayer perceptron

Training algorithm for multilayer perceptron is the backpropagation (Rumerlhart et al., 1986) o a variant of it. The algorithm tries to minimize the mean square error between the output of the multilayer perceptron and the desired output by changing the weights in the input of the neurons. The algorithm is a supervised learning algorithm, thus it requires a set of pairs pattern-output. This set is divided in two subsets, one for training and the other one for validation. The algorithm begins with random weights and presents the training set to the neural network. At the end of the iteration it calculates the mean square error and changes the weights in the inputs in the direction of minimizing the mean square error. The actualization of the weights in the hidden and input layers requires calculating the gradient. Therefore the transfer functions in the neurons have to be continuous. After several iterations, the neural network learns to classify according to the presented problem. The validation of the algorithm consists on presenting the validation subset and calculating the network throughput. Basically, calculating the success rate for an independent set (the validation subset).

The steps in the design of a multilayer perceptron are:

1. selection of the input and its codification
2. selection of the output codification
3. number or hidden layers and number or neurons in each layer

4. selection of the training and validation sets
5. selection of the training algorithm
6. selection of the transfer function en each neuron in each layer.

5.3 Genetic Algorithms

Genetic algorithms (Holland, 1962; Bremermann, 1962; Goldberg, 1989; Michalewicz, 1992) are bio-inspired systems as well. They are based in the evolution theory by natural selection developed by Darwin. A population of individuals evolve over generations, some individuals adapts better to the environment and have a higher probability of survival. The evolution occurs due to two processes, the crossover between individuals (mixing their genetic information) and the mutation of one individual.

Genetic algorithms are used in a wide range of fields such as optimization, robotics, control system, classification, etc.

Population represents a set of solutions for a problem. The objective is to evolve the population for a specific problem trying to produce better generations of solution to the problem than their ancestors.

Chromosomes are the individuals of the population. This is the solution to the problem. The codification of the chromosome depends on the problem. Essentially is a string of genes

and these can be binary numbers, real numbers, intervals, represent an order, etc. We work over the original codification, the binary string.

Fitness function evaluates each chromosome in the population. The idea is to determine which individuals (solution to the problem) adapts better to the environment (solve the problem better). Each chromosome has a fitness.

The main operators applied to the chromosomes are the crossover and the mutation. In the crossover two chromosomes mix their genes generating one or more offspring. The codification of the chromosomes determines the kind of crossover operators that can be applied. One-point crossover selects a point in the parents' individuals and exchanges the genetic information after this point generating two children with a mix of the genetic information of the parents. In the mutation, a chromosome changes one gene. Once again, the codification determines the kind mutation operator. The simple mutation, for binary codification, changes a gene for the other value, i. e. from 0 to 1 or vice versa. Figure 5.3 shows a graphic description of the crossover and mutation operators.

These operators described above are applied to a subset of the population. The selection procedure picks the individual over which the operators will be applied. The selection depends on the fitness of the individual and some probability. Therefore the best individuals have higher probability for crossover and mutation and their genetic information will keep in the

following generations. A typical procedure is the selection by roulette. Each individual has a percent assigned as a function of its fitness (the larger the fitness, the larger the percent) and a random number will fall inside the interval of an individual, then this individual is picked. Figure 5.4 illustrates the process of roulette selection.

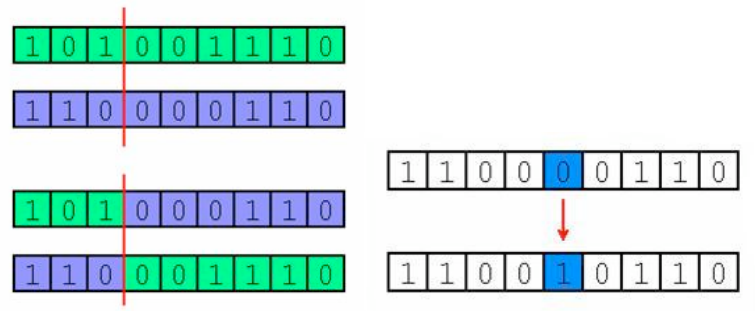

Figura 5.3. Crossover and mutation operators

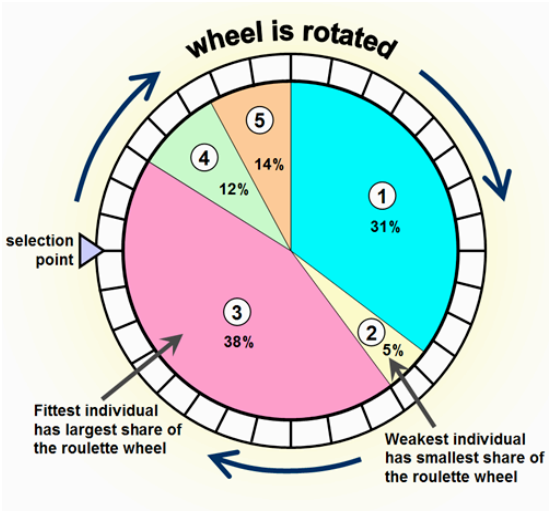

Figure 5.4. Roulette wheel approach based on fitness. There are 5 individuals with a percent assigned as a function of their fitness. The selection point falls into one of the individuals. Fitter individuals have higher probability of being selected while weaker individuals have lower probability of being selected.

Finally the elitism operator keeps the best individuals in the population over generations until another better individual substitutes it. This operator increases the velocity of convergence in genetic algorithms when they are used for optimization.

5.4 Design of the cloud classification algorithm

Inputs to the neural network are a set of parameters extracted from every pixel of the images. Parameters are extracted from the image by using a 1 and 9 pixel window (see figure 5.6). For each pixel we compute some parameters using a 9 pixels window centered on it, that is, using information from the eight pixels that surround it (neighbors). The first version of the procedure had a total of 18 parameters extracted from the pixels. These parameters are:

- Value of signal in R channel
- Value of signal in G channel
- Value of signal in B channel
- Mean value of pixel and neighbors in R channel
- Mean value of pixel and neighbors in G channel
- Mean value of pixel and neighbors in B channel
- Variance for the pixel and its neighbors in R channel
- Variance for the pixel and its neighbors in G channel

- Variance for the pixel and its neighbors in B channel
- Value of signal in gray scale
- Mean value for the pixel and its neighbors in gray scale
- Variance of values for the pixel and its neighbors in gray scale
- R/G for pixel
- R/B for pixel
- G/R for pixel
- G/B for pixel
- B/R for pixel
- B/G for pixel

Consequently, the input layer of the multilayer perceptron (MLP) has 18 perceptrons.

We have established three possible output classes. The pixels are classified as opaque cloud, thin cloud, or clear sky by visual inspection of the images. Hence the output layer has three perceptrons. Each perceptron in this layer evaluates one of the three classes. The outputs of the neural network are in the range [0,1].

Values close to 1 indicate that the pixel corresponds to the class. Values close to 0 indicate that the pixel does not correspond to the class.

The neural network has only one hidden layer, as a multilayer perceptron only needs three layers to create a decision region as complex as required (Lippman, 1987), and the number of perceptrons is the same as the input layer, since some testing revealed that more perceptrons do not increase the performance.

The selection of the training and test sets is a delicate operation. The set has to cover all the possibilities that we encounter. The procedure to create these sets requires the visual inspection of the images extracting portions of them and classifying them. For that reason we examined a set of 50 images with a wide variety of sky conditions and extracted specific regions of those images. Those regions are patches of the images, some of them close to the horizon, the circumsolar area and transition between cloud and sky, which are difficult areas to classify, and also areas of clear sky and inside a cloud. The 18 parameters are extracted for each pixel in those portions of the images and we labeled the pixels in one of the three possible classes and made a table with the input parameters and the corresponding class. This set has a size of about 1000 samples. This set was randomly divided in two, and one set was selected as training and the other as a test set.

Transfer function has been selected by test for each layer in the neural network. The output layer has a sigmoid transfer

function since the output range is [0, 1]. In this layer the neuron with the maximum decides the class of the sample is being classified. For the hidden and input layers the difference between a lineal or sigmoid transfer function is minimum, so lineal function is selected.

The training algorithm was also selected by test. Five variations of backpropagation (Howard and Beale 2000), and the one with the best performance was selected. Three random seeds have been selected for the division of the table in training and validation sets and the network has been trained three times for each set (running 6 times per seed using one of the divisions as training and the other as validation and vice versa). The network has been trained over 100 iterations reaching a mean square error in the training set of 10^{-2}. Resilient backpropagation (Riedmiller and Braun, 1993) is the one that reached the best performance (over 80% of success in all runs). This variant of the backpropagation only uses the sign of the derivative to determine the direction of the weight update, the magnitude of the derivative has no effect on the weight update and therefore the optimum is reached faster when the transfer functions are sigmoid. The size of the weight change is determined by a separate update value. The parameters of the training algorithm have been left by default since the results were good.

A large set of parameters has been selected in the beginning and an optimization process has been applied to reduce

the number or parameters keeping or increasing the performance of the neural network as explained in the next section.

5.5 Design of the optimization algorithm

A genetic algorithm minimizes the number of input parameters keeping or increasing the performance of the neural network. Reducing the number or parameters we reduce the size and therefore the running time and efficiency of the classification.

The chromosomes represent the input parameters to take into account. They are a binary string of 18 elements (genes) with a value of 1 when the parameter is taken into account and 0 otherwise.

Fitness for each individual is the performance of the network with the corresponding input parameters. Therefore, the fitness function creates a neural network with the corresponding inputs, it trains it and validates it. The validation consists in presenting the validation set to the network and calculates the success rate in the classification for that set.

The crossover operator selected is the simple crossover explained in section 5.3 but modified to, at least have one 1 (there has to be at least one parameter as input). If all the parameters are 0, mutation is forced. The mutation parameter also described in section 5.3, was also modified to avoid an individual

with all genes to 0 (again another mutation is forced). The selection algorithm is the roulette also described in section 5.3.

Initial population is generated randomly but the individual with all genes to 1 is forced to be in the population. This way, the reference neural network explained in section 5.4 is evaluated in the first generation. The genetic algorithm evolves to better solutions that necessarily have less parameters. If all parameters were needed, the highest fitness value would be reached in the first generation, if not, following generations will create individuals with less parameters and thus the final neural network will be an optimization of the original one.

The parameters used in the genetic algorithm are:

- Number or generations: 500
- Population size: 50
- Crossover probability: 0.9
- Mutation probability: 0.1

5.6 Final procedure

Different in-house programs have been designed in order to develop a final procedure for the cloud cover assessment using the techniques discussed in sections 5.4 and 5.5. First, the design of the neural network (creating and optimizing with a genetic

algorithm) was developed and, second, the program that classifies the pixels of the sky images and provides the cloud cover assessment of the sky images.

One program, the NN program, enables creating and training neural networks specifying some parameters, i.e., the number of neurons in the different layers, the transference functions, the learning algorithm, and the training and test sets. Another program, the GA program, implements the genetic algorithm and all the functions required, including the fitness function, i.e., the NN program. The outputs of the GA program are the best neural network found and its performance. Figure 5.5(a) shows a schema of this procedure, and figures 5.5(b) and 5.5(c) show flux diagrams of the GA program and the subroutine that creates and evaluates the neural network, i.e., the NN program. The performance is calculated from the test set, computing the error rate in that set.

Finally, another program analyzes the images for cloud classification using the neural network obtained with the genetic algorithm. This program first extracts the parameters of the image pixels, i.e., the input of the neural network; then the neural network classifies every pixel; and, finally, a new image, the result image, is built representing the opaque clouds as white, the thin clouds as gray, and the sky as blue. Black represents areas not analyzed, which are the solar-shadow system and the building on the horizon. This result image is analyzed to extract information about cloud cover in percent or oktas for the two cloud classes (opaque and thin) and the cloud cover in different regions of the

image and the brokenness and uniformity of cloud cover. Figure 5.6 is a schema of this procedure with an example of the original and result images. The output parameters extracted from the sky images are:

- Percent of opaque clouds
- Percent of thin clouds
- Oktas for opaque and thin clouds
- Percent of opaque clouds in every octant (Fig. 5.7)
- Percent of thin clouds in every octant (Fig. 5.7)
- Sun position in octant (Figure 5.7)
- Brokenness of cloud cover
- Uniformity of cloud cover

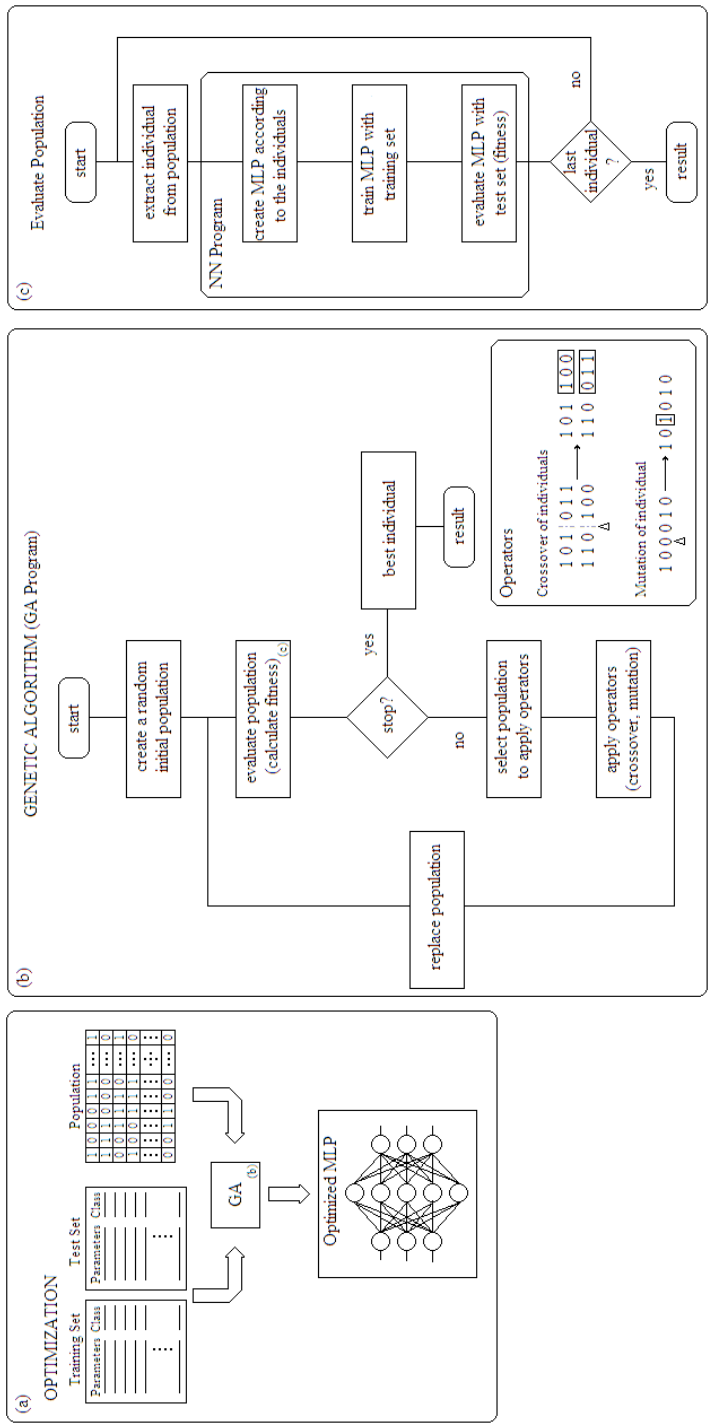

Figure 5.5. (a) Schema of the optimization procedure. (b) Flux diagram for the GA program. (c) Flux diagrams for the NN program.

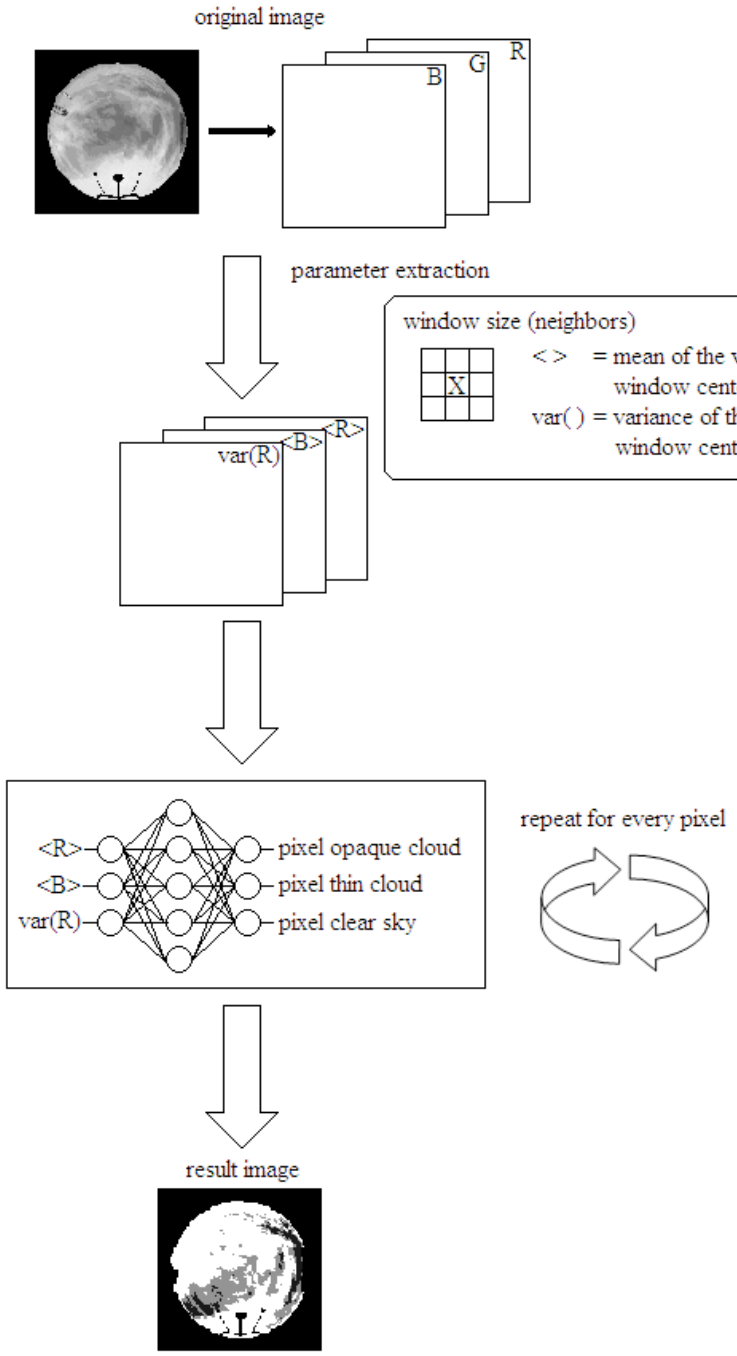

Figure 5.6. Schema of the final procedure. It receives a sky image and generates the resulting image.

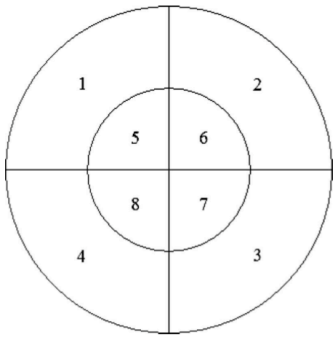

Figure 5.7. Position of the octants for the output parameters. (The image is rotated to calculate the percent in regions; hence the south is always placed at the bottom of the image.)

The program creates a thumbnail version of the original and analyzed images and they are showed on a website in real time along with some analysis (oktas and percent of clouds). This website was developed by the GFAT using PHP (www.php.net). The website also allows to navigate through all the stored images (starting on October 2005). It can be accessed through the address http://cloudcamera.ugr.es or navigating through the GFAT website: http://atmosfera.ugr.es. Figure 5.8 shows an example of the website.

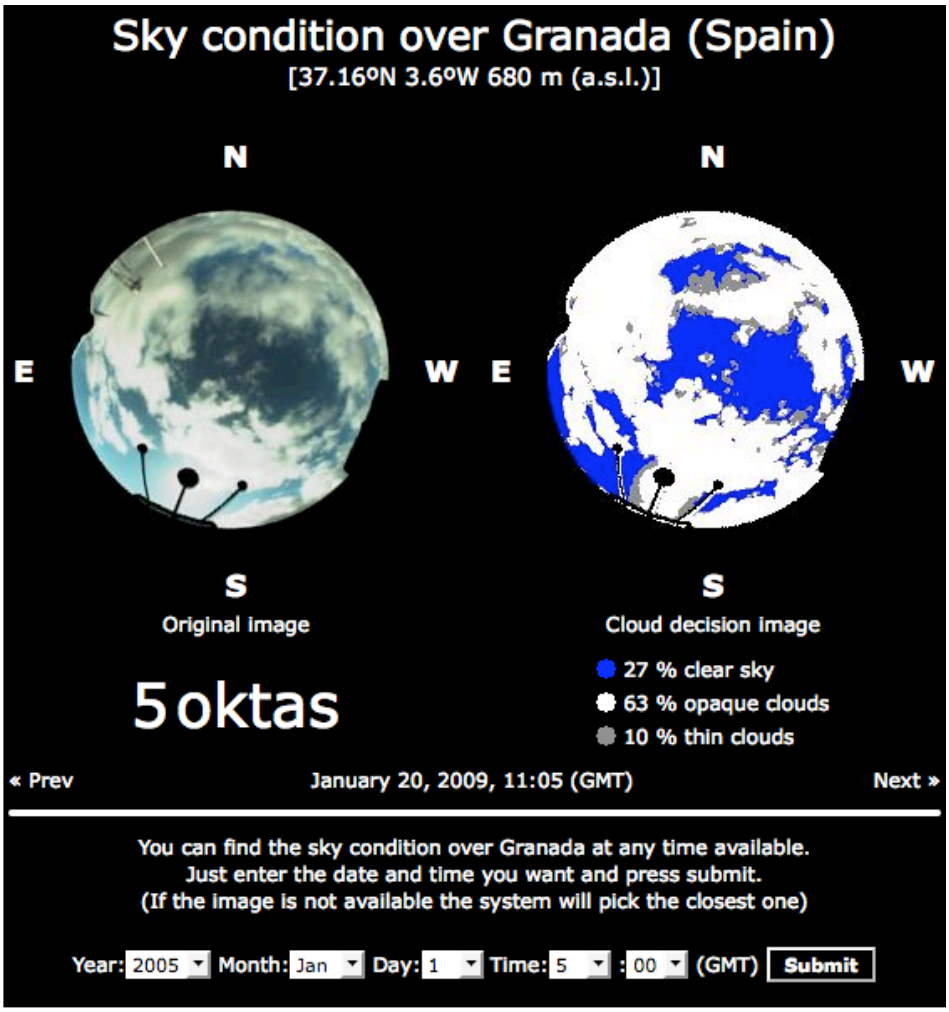

Figure 5.8. Image capture of the website showing the original image on the left, processed image on the right and analysis.

Initially, we use as many as 18 inputs parameters for the neural network. The performance of the neural network is calculated by using the test set. First, we calculate the error rate, or error in classification (number of errors divided by the number of cases in the test set), then, the performance is (1 – error rate). The

performance of this version of the neural network is 82% including the whole set of input data; that is, the error in pixel classification is 18%.

The genetic algorithm found the best neural network with three input parameters out of the original 18. These parameters are the mean of the pixel and its neighbors in the red and blue channels and the variance of the pixel and its neighbors in the red channel (a schema of the neighbors of the window size can be seen on figure 5.6). The performance of the optimized neural network is 85%, that is, the error in pixel classification is 15%. More important, with the reduction in the number of input parameters, the time used in the parameter extraction procedure is significantly reduced and the running time if the whole procedure is reduced too. It is also significant to emphasize that the information is in the red and blue channels; that is, the channels used in the algorithms based on threshold of the red/blue ratio image. The use of more parameters or different channels contaminates the learning process of the neural network, worsening performance when more inputs are used.

5.7 Results and evaluation

5.7.1 Pixel-based evaluation

As indicated in section 5.4, we have selected a set of 50 images with a wide variety of sky conditions, making a set of about 1000 samples. This sample test was randomly divided in two,

one selected as training and the other as test. To evaluate the classification procedure in this section we have used the set of 500 samples not selected in the training procedure. Thus, we have used different approaches. In the pixel-based evaluation we have tested the number of successes and failures, discriminating the type of failure. That is, there are three classes, so when the neural network fails in the classification of pixels there are two possibilities: the neural network can fail classifying in one class or another. Table 5.1 shows error frequencies for the three classes. The first row shows the error frequency for classification of the neural network in the three different classes for the pixels cataloged as clear sky by a human observer. The second row shows the same for pixels catalogued as thin cloud by a human observer, and the third row those cataloged as opaque. The classification of clear skies is quite good; over 88% of the test pixels are correctly classified. Opaque clouds are also well classified; more than 84% of the test pixels are correctly classified. Over 61% of thin clouds pixels are correctly classified, but almost 30% are classified as clear skies and about 10% are classified as opaque cloud. Human inspection of pixels for classification is quite complicated in this case. Thin clouds are difficult to detect visually in the sky images, so that may be one reason why thin clouds are detected as clear sky. On the other hand, the ability of the observer to distinguish between opaque and thin clouds is a source of error mainly when the pixel is wrongly classified as opaque cloud.

	Pixel estimated as (%)		
Pixel observed as	Clear sky	Thin cloud	Opaque cloud
Clear sky	**88.11**	28.44	5.78
Thin cloud	11.01	**61.41**	9.45
Opaque cloud	0.88	10.16	**84.77**

Table 5.1. Contingency of the relative frequency of pixel classification (maxima are boldface)

5.7.2 Image-based evaluation

The evaluation of the procedure for cloud cover assessment requires a reference to compare the actual sky condition with the cloud cover estimated over the whole image. This can be done by comparing the performance of the full classification of our methodology with an independent record of cloud cover by human observers. The closest meteorological office is situated at the Armilla Air Force Base, located 4 km from the station. There are no mountains, big buildings or other obstacles between them; so, it is assumed that the cloud cover registered at the meteorological office is similar to the estimation of cloud cover with the All-Sky Imager. The meteorological office archives the METAR reports (WMO, 1995). METAR stands for aviation routine weather report, and it is used by pilots in partial fulfillment of a preflight weather briefing. These reports are generated every hour in daytime and include information about cloud cover. The cloud cover given is not the best, as it is given in ranges of oktas instead of oktas per se. That is, there is a category for clear skies (0 oktas), another for few clouds (1-

2 oktas), another for scattered clouds (3-4 oktas), another for broken clouds (5-7 oktas), and the last one for overcast (8 oktas).

The All-Sky Imager provides the percent of clouds and the number of oktas, so the resolution is different, and we have to assume an uncertainty of at least 1 okta in the comparison. For the METAR categories we use the mean of oktas in the interval, e.g., the "few clouds" category is 1.5 oktas (± 1 okta), "scattered clouds" is 3.5 oktas (± okta) and so.

The evaluation has been performed over 15 months of data (from October 2005, to December 2006). Figure 5.9 shows the monthly average oktas registered on the METAR record and by the All-Sky Imager. This average has been done with estimation from all the images available and all the available METAR observations for every month. Figure 5.10 shows the number of sky images for each month. We can see that August and September of 2006 have very few images because of a period of inactivity due to maintenance of the All-Sky Imager. These months are omitted from this study. The difference between the monthly METAR register and the monthly estimated cloud cover is less than one okta (the resolution error of the comparison) except for December 2005 and April 2006, for which the differences barely exceed one okta, and May, July and October of 2006. This difference can be explained by the incidence of Saharan dust events at Granada (Lyamani et al., 2005; 2006). Dust events contains mainly coarse particles that provoke a strong forward scattering, and therefore the brightness of the image, especially in the circumsolar area, is higher than usual. This

brightness is classified as cloud by the algorithm procedure and introduces an error.

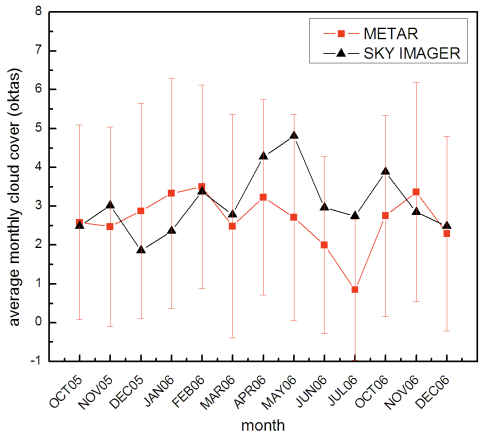

Figure 5.9. Comparison of monthly average oktas of METAR record for clouds (and its standard deviation) and the All-Sky Imager. The averages are computed using all the measurements in every month.

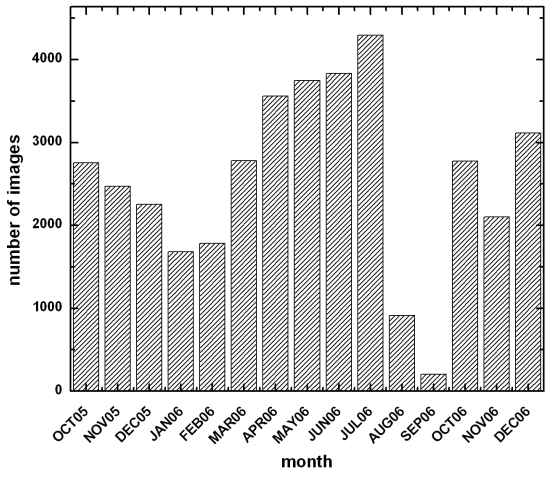

Figure 5.10. Number of images registered by the All-Sky Imager every month.

Figure 5.11 further illustrates the impact of the dust events on the comparison between the All-Sky Imager and METAR results. The bar values show the absolute difference between the All-Sky Imager oktas and the METAR report for clouds. The line plot in figure 5.11 shows the monthly values of the Ångström exponent that characterizes the spectral dependency of the atmospheric aerosol optical depth and it is related to the size of the particles (see section 2.4.3 and equation 2.11): large values of α indicate the prevalence of fine particles from urban-industrial and biomass burning sources, while low values of α are related to the presence of coarse particles such as desert dust. We have computed the Ångström exponent in the interval 440-1020 nm, using the photometric CIMEL-CE318 measurements (Lyamani et al., 2006). Figure 5.11 shows that the months with bigger particles in average are May, June and July 2006. Figures 5.9 and 5.11 show that the two months with meaningful negative differences (about 1 okta, All-Sky Imager – METAR), December 2005 and January 2006 correspond to the highest values of the Ångström exponent. On the other hand, the greatest positive differences (about 2 oktas, May and July 2006) correspond to the lowest values of Ångström exponent.

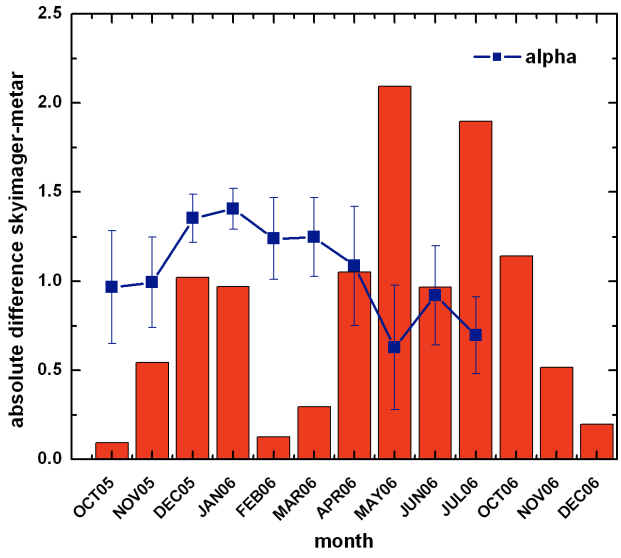

Figure 5.11. Absolute difference between All-Sky Imager estimated oktas and METAR report for clouds. The ordinates axis also gives the values of the Ångström exponent (alpha).

As example, figure 5.12 shows the measurements of the All-Sky Imager and the METAR report for clouds on May 29 2006, during a day with a dust event. The CALIMA web site (Characterization of Aerosol due to African Mass Intrusions, www.calima.ws) from the Environmental Ministry of Spain recorded that the day was associated with a Saharan dust event. Thus, the number of oktas estimated with the sky images is higher than the values registered in the METAR reports.

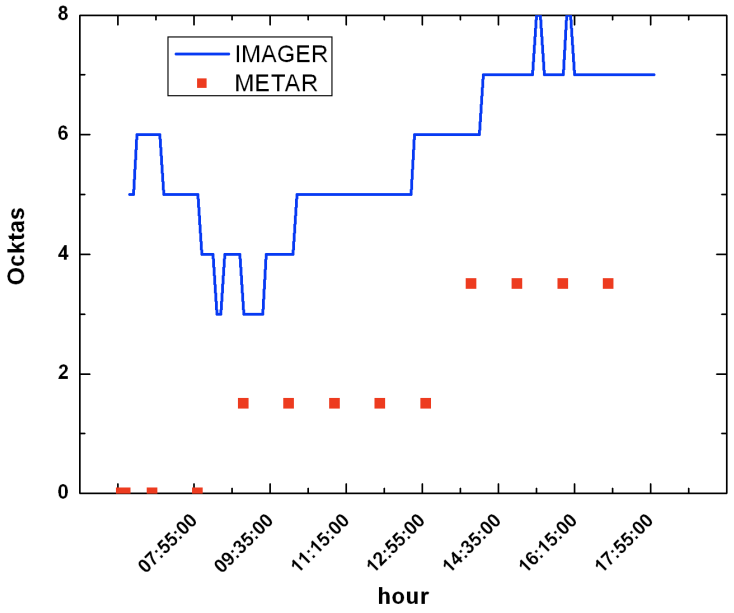

Figure 5.12. Estimation of cloud cover and METAR report during a dust event (May 29, 2006).

Figure 5.13 shows a relative frequency histogram for the difference between All-Sky Imager oktas and the METAR report for cloud cover in temporally coincident measurements. More than 60% of the sky images estimates differ less than or exactly one okta from the synchronic METAR report. This is the minimum uncertainty that can be expected in the comparison, since METAR data are given in interval of 2 or 3 oktas. On the other hand, as we have seen in figure 5.11, dust events explain the cases when the difference between All-Sky Imager and METAR is larger, as the All-Sky Imager procedure classifies a greater part of the sky as cloudy in those cases.

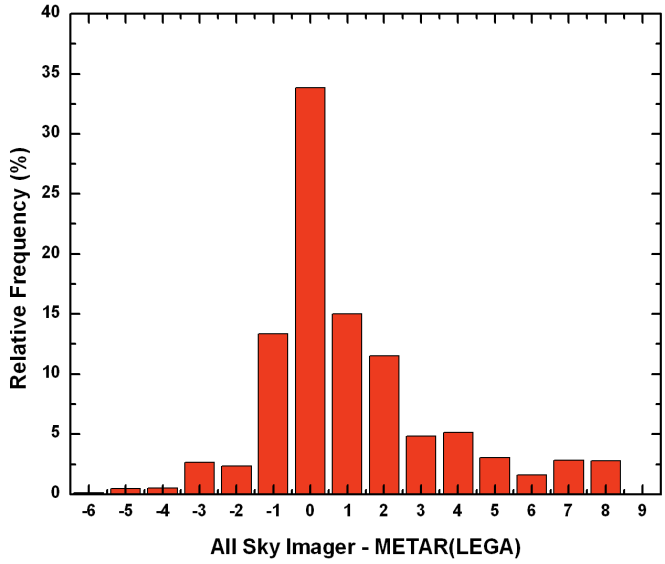

Figure 5.13. Relative frequency histrogram for the difference between All-Sky Imager oktas and METAR records for cloud cover in temporally coincident measurements over the whole data set.

6

Aerosol characterization

Section 4.2 presented the sun photometry as the most common way to characterize the atmospheric aerosol. Aerosol optical depth (AOD) is calculated by extinction measurements using the Beer-Bouguer-Lambert law (equation 2.20), and the microphysical properties of the atmospheric aerosol are calculated by inversion codes using either the AOD or a combination of AOD and sky radiance measurements performed at the principal or almucantar planes.

Sky imagers can capture the sky brightness (in the form of pixel counts) or even sky radiance of the whole sky simultaneously. On the dark side, direct irradiance is not available because the sun disc is blocked with the shadow system.

This chapter presents a methodology for the estimation of AOD and its spectral dependency with the All-Sky Imager and the WSI and, in a second step, an inversion code applied to the WSI data for size distribution estimations.

6.1 Optical properties of the atmospheric aerosol

Calculating the AOD with a sky imager requires a different approach than the traditional methodology applied in sun photometry. Since the sun, and therefore the direct solar irradiance, is not available, we use the sky radiance on the principal plane to estimate the AOD. Before we discuss the methodology we need to introduce one of the tools used. The AOD is estimated using a neural network. Section 5.3 introduced the neural networks and the multilayer perceptron. This time a different kind of neural network is used and presented in the following section.

6.1.1 Radial Basis Function Neural Networks

Radial basis function (RBF) networks (Yee and Haykin, 2001; Gutiérrez et al., 2004) are especially suitable for function approximation. The inputs of the radial basis networks are the variables of the function, and the output is the function approximation.

RBFs emerged as a variant of neural networks in late 80s. However, their roots are established in much older pattern recognition techniques as for example potential functions, clustering, functional approximation and spline interpolation (Tou and Gonzalez., 1974). RBFs are embedded in a two layer neural network, where each hidden unit implements a radial activated function. The output units implement a weighted sum of hidden unit

outputs. The input into an RBF network is nonlinear while the output is linear. Their excellent approximation capabilities have been studied by Poggio et al. (1990) and Park and Sandberg (1991). Due to their nonlinear approximation properties, RBF networks are able to model complex mappings, which multilayer perceptrons can only model by means of multiple intermediary layers (Haykin, 1994).

Same as multilayer perceptrons, the design of a RBF network requires determining the inputs (variables of the function), the output (the function values), the number of neurons and the training.

The topology of the RBF networks consists in a two-layer feed-forward neural network. Such a network is characterized by a set of inputs and a set of outputs. In between the inputs and outputs there is a single hidden layer of neurons. Each of them implements a radial basis function. Figure 6.1 shows the topology of the RBF networks.

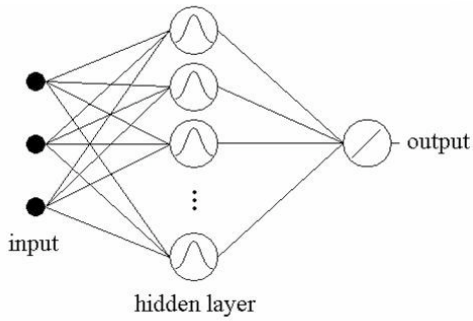

Figure 6.1. RBF network topology

RBF networks are characterized for its transfer function, which is the RBF. In this case input to the transfer function is the vector distance between its weight vector *w* and the input vector *p*, multiplied by the bias b

$$n = \|w - p\|b\,. \tag{6.1}$$

The transfer function for a radial basis neuron is a Gaussian function

$$a(n) = \exp(-n^2)\,. \tag{6.2}$$

The RBF has a maximum of 1 when its input is 0. As the distance between *w* and *p* decreases, the output increases. Thus, a radial basis neuron acts as a detector that produces 1 whenever the input *p* is identical to its weight vector *w*. The bias *b* allows the sensitivity of the neuron to be adjusted.

This topology allows a very simple training for function approximation or interpolation. Every sample in the training set creates a new neuron in the hidden layer, i.e. the hidden layer has the same number of neurons as samples in the training set. The weight of the connection input-neuron is set to the input value. Therefore *n* in function (6.1) is 0 and *a* in function (6.2) is 1. The last layer gathers the hidden layer's outputs and readjusts the output to provide the correct function value. A typical input would activate several neurons (the weight is not exactly the same as the input since the input is not in the training set), i.e. $0<a<1$ for several neurons output and the final output to the network is a combination of the different neuron outputs. This feature allows to the network to

interpolate the function values and, therefore learn the shape of the function. Assuming that the training set is well spread along the input range, the RBF network learns the shape of the function with the training set. An independent set, the test set, is used to evaluate the function approximation. It works like a spline interpolation with the advantage that N-dimensional functions can be approximated easily but the disadvantage that the function is unknown.

6.1.2 Aerosol Optical Depth estimation

The sky radiance depends directly on the molecules, and aerosol load through several parameters connected with extensive and intensive aerosol properties. While previous investigations have related AOD to radiances measured in a restricted range of scattering angle to simulate the spaceborne point of view (e.g. Kaufman, 1993; Sánchez et al., 1998), here the development is focused on surface measurements.

There is a dependency between radiance along the principal plane and the aerosol optical properties (Olmo et al, 2008). The effect of the AOD and α on the radiance over the principal plane is shown in figure 6.2. The graph shows sky radiance over the principal plane measured with the WSI on two different days with extreme values of α and different values of AOD. The relationship of the radiance over the principal plane and the AOD can be seen as well as the relationship of the radiance over the principal plane, the wavelength and α.

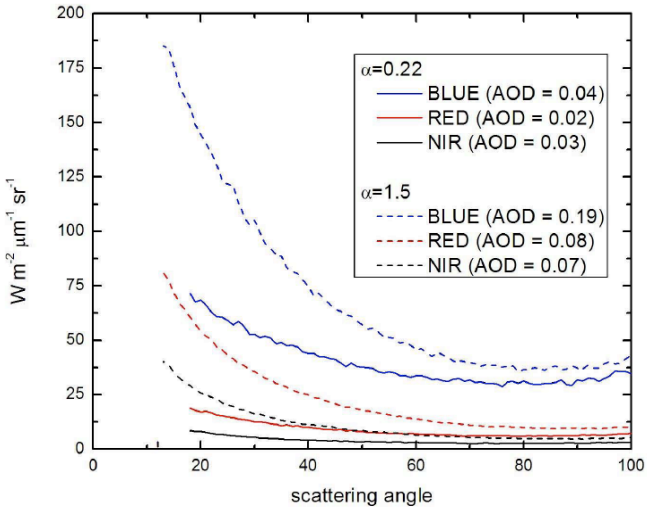

Figure 6.2. Comparison of the radiance along the principal plane of the WSI varying the □ngström exponent □ and AOD. The three wavelengths of the WSI are represented.

As we stated before, the methodology applied uses RBF networks. We are considering that the AOD is a function of the sky radiance over the principal plane. Several scattering angles are selected as inputs to the RBF network and the output is the AOD itself. There are several differences in the methodology applied to the All-Sky Imager and the WSI, so both methodologies are explained in separated sections.

6.1.2.1 All-Sky Imager

The information provided by the All-Sky Imager includes the sky brightness reaching the surface for every pixel of

the image. This brightness is, in the form of pixel counts, somehow related to the sky radiance assuming the linearity of the CCD sensor. This approximation also includes the assumption of knowing the filters response and the uniformity of the bayer mosaic of the CCD (see section 4.1.1.1).

Looking at figure 6.2 we observe that scattering angles closer to the Sun exhibit a large dependence on the AOD. The scattering angle at 90º has a smaller dependency on AOD and also on the Ångström exponent α. This last scattering angle is the minimum polarization point and it is the point where the Rayleigh scattering presents a minimum (see section 2.2.1).

Inputs to the RBF networks are sky radiances at specific scattering angles in the principal plane. We selected a value close to the sun (20º scattering angle) and the 90º scattering angle. These values are easily retrieved using the equations 4.1 and 4.2 presented in section 4.1.1.3. On the other hand, the brightness of the sky also depends on the SZAº or, in other words, the amount of radiation reaching the earth's surface depends on the air mass. Finally, these sky radiances and the cosine of the SZAº (for its relation to the air optical mass, equation 2.13) are inputs to the RBF network.

AOD is wavelength dependant, and we need to relate the channels of the All-Sky Imager with the spectral dependence of extinction measured by the CIMEL CE318. We considered relating the blue channel with the 440 nm and the red channel with the 670

nm wavelength. Thus, the output of the neural network is the value to be estimated, i.e. AOD at 440 nm and 670 nm corresponding to the blue and red channels, respectively. There is a different neural network for each AOD. The training process requires a data set pairing inputs and outputs. The inputs are the sky radiances at 20º and 90º scattering angles in the corresponding wavelength and the cosine of the SZAº; the outputs are the AOD at 440 nm or 670 nm.

The experimental data used in this work are sky images catalogued as cloudless skies from October 2005 to February 2006. Using the methodology explained in chapter 5 we sorted out the cloudy images. The final data set consisted on 1018 images that were processed to extract the inputs and matched to CIMEL CE318 measurements. The time interval for both instruments is different, so we established a margin of ±2 minute for the association. These 1018 experimental cases were used for model development and for validation. This set is divided randomly in two subsets, a training set using 2/3 of the whole data set and a test set using 1/3 of the whole data set. All values, inputs and outputs, were normalized to the range [0,1], i.e. the values are rescaled to that range where the minimum and maximum values correspond to 0 and 1, respectively. During the training every measurement is used to adjust the internal values of the neural network (the weights) so the output is the desired variable amount, i.e. the AOD corresponding to the wavelength we are trying to estimate. Once the network is trained we use the test set to evaluate the performance of the network. The coefficient of determination (R^2), calculated between the AOD

estimated with the CIMEL and the values estimated with the All-Sky Imager using the test set, is our performance estimator. The performance depends on the selection of the training and test sets. These sets are created randomly out of the whole data set. Hence we repeat the process nine times and select the best partition, i.e. the one that yields the best performance.

6.1.2.2 Whole Sky Imager

The absolute radiance calibration of the WSI provides the actual sky radiance in every scattering angle. Section 4.1.2.2 explained the calibration process and equation 4.3 lets us pixel calibrations in the sky image for absolute radiance.

We extract the sky radiance values over the principal plane in the images for every scattering angle. Thus, we have these values for scattering angles from 1º to 100º. Equations 4.5 and 4.6 in section 4.1.2.3 let us obtain the coordinates x and y in the image plane given a zenith and azimuth angle, so knowing the Sun position we can locate the principal plane making the azimuth angle equal to the Sun azimuth angle and varying the zenith angle. While in the All-Sky Imager methodology we selected a couple of scattering angles by visual inspection of the principal planes as criterion, here the selection of those scattering angles is done by means of a greedy algorithm (Cormen et al., 2001). The greedy algorithms are iterative algorithms that build a string solution getting the best item every loop. While AOD is sky radiance dependent, not

all the scattering angles are necessary in its estimation. The first iteration of the algorithm creates 100 networks using the radiance at one of the scattering angles. All of them are evaluated and the best one is added to the solution. The second iteration of the algorithm creates 99 networks using the radiance at the best scattering angle of the previous iteration and the radiance at a different scattering angle. Once again, the best one is added to the solution. This process is repeated until the performance decreases, i.e. no more scattering angles are needed. During the process we applied a mask to eliminate the measurements with non-valid values (obstruction due to the horizon or shadow system or brightness in the circumsolar area). As a result, the final data set may vary depending on the scattering angles used. Summarizing, as inputs we have the sky radiance in scattering angles selected by the greedy algorithm and the SZA°.

Again, we need to relate the wavelengths of the WSI filters with the wavelengths used to measure the extinction values with the CIMEL CE318. We used the nearest wavelength and, therefore the 450 nm filter is associated with the 440 nm in the CIMEL CE318, the 650 nm filter is associated with the 670 nm and the 800 nm filter is associated with the 870 nm. Thus, we developed a RBF network model for each WSI wavelength obtaining an estimation of the AOD at 440, 670 and 870 nm respectively.

The data set selected in this work comprises the period from October 1st 2001 to September 29th 2002. This data set is from a whole year, so we can model the seasonal variability of the

atmospheric aerosol. Using the cloud decision images processed by the Atmospheric Optics Group (AOG) we sorted out all the cases with clouds, to work with the clear-sky results. A total of 1047 clear-sky image sets (i.e. 3 spectral images acquired in one set) were associated with a synchronous CIMEL measurement, applying a ±2 minutes margin. This image set has been used to create and validate the model. The whole data set consists of the radiances over the principal plane of the 1047 images, the SZA° at the time of the measurement and the synchronous AOD calculated with the CIMEL CE318. This set is divided randomly in two subsets, a training set using 2/3 of the whole data set, and a test set using 1/3 of the whole data set. All values are normalized to the range [0,1] as in the All-Sky Imager methodology. The R^2 calculated between the AOD estimated with the CIMEL and the values estimated with the Whole Sky Imager using the test set, is our performance estimator. Again, the process is repeated nine times and selects the best partition, i.e. the one that yields the best performance.

6.1.3 Ångström exponent

Once we obtain the AOD, its spectral dependency offers valuable information about the particles size in a direct and simple way. Section 2.4.3 introduced the Ångström Law (equation 2.23) and the Ångström coefficients α and β. The calculation of these coefficients requires defining the spectral interval. The most common way is to consider the visible and near infrared interval

440 – 1020 nm. Other authors define intervals in the ultraviolet (340 – 380 nm), visible (440 – 670 nm) and near infrared (870 – 1020 nm) and three different Ångström exponents α_1, α_2 and α_3 (e.g. Vergaz, 2001).

Once the interval is selected, there are several ways for calculating the Ångström coefficients. The most common way is the linear fit of the spectrum expressed as:

$$\log \delta_{a\lambda} = \log \beta + \alpha \log \lambda \tag{6.3}$$

using the interval 440-1020.

We will use this methodology for the WSI and a technique with neural networks for the All-Sky Imager and the WSI as explained in the following sections.

6.1.3.1 All-Sky Imager

Using the traditional methodology and the equation 6.3 with the All-Sky Imager AODs does not provide good results. AODs are estimated well, but the propagation of errors when we calculate α does not allow getting to a good estimation. For this reason a new RBF network model is applied. The idea is the same as the estimation of the AOD. α is a function of the sky radiance and therefore can be estimated with a function approximation method. Since α is the spectral dependency of the AOD we need the sky radiance on several wavelengths as inputs to the model. Also, in

section 6.1.2 and figure 6.2 we saw that α is more sensitive to changes of sky radiance in scattering angles closer to the sun. For these reasons we created the model using as inputs the sky radiance on 10º, 20º and 90º scattering angles in both blue and red channels. SZAº is also an input.

The procedure is exactly the same as in AOD estimation. The same data set, the same splitting in training and test sets and so on. Now the output is α instead of the AOD at a specific wavelength. α can be calculated using different intervals. The interval 440-1020 nm includes the wavelengths of our All-Sky Imager, and therefore this is the interval used to compare the results. The R^2 calculated between the α estimated with the CIMEL in that interval and the values estimated with the neural network using the test set, is our performance estimator. Again, the process is repeated nine times and selects the best partition, i.e. the one that yields the best performance.

6.1.3.2 Whole Sky Imager

Two different approaches have been tested to estimate the Ångström parameters. First, we use the method explained in section 6.1.3 (linear fit) using the AODs estimated with the neural networks, as seen in section 6.1.2.2. Secondly, a new RBF network has been trained using the α calculated with the CIMEL CE318. In this case the interval is 440 – 870 nm. The procedure is the same applied to the All-Sky Imager explained in section 6.1.3.1.

6.1.4. Results and evaluation

6.1.4.1 All-Sky Imager

Figure 6.3 shows the AOD (440 nm) estimated with the neural network using the blue channel of the sky images versus the AOD (440 nm) calculated with the CIMEL CE318. Figure 6.4 shows the AOD (670 nm) estimated with the neural network using the red channel of the sky images versus the AOD (670 nm) calculated with the CIMEL CE318. In both cases, the analyses have been performed over the test set. The linear fits are forced through zero, thus the slope *b* provides information about the relative over- or underestimation associated with the model. The coefficient of determination R^2 gives an evaluation of the experimental variance explained by the model. The performance of the models was evaluated also using the root mean squared deviation (RMSD) and the mean bias deviation (MBD). These statistics allow for detection of both the differences between experimental data and model estimates and the existence of systematic over- or underestimation. Table 6.1 shows statistics of the analyses for the different models selected.

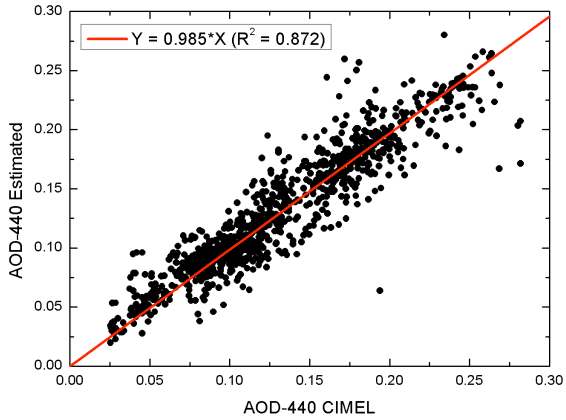

Figure 6.3. Scatter plot of estimated versus measured values for AOD at 440 nm.

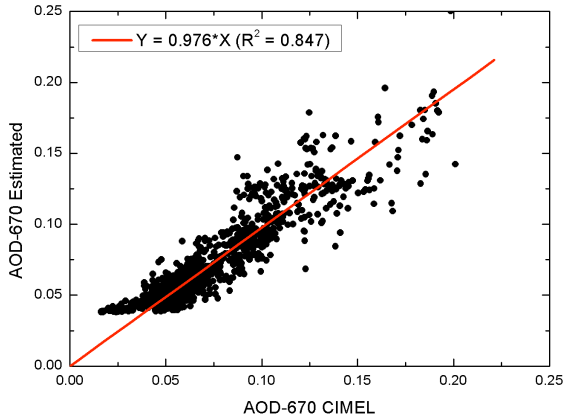

Figure 6.4. Scatter plot of estimated versus measured values for AOD at 670 nm.

Finally, Figures 6.5 and 6.6 show histograms of the differences between measured and estimated AOD (440 nm) and AOD (670 nm), respectively. Figure 6.5 reveals that 52% of the estimated AOD (440 nm) has deviation less than 0.01. Figure 6.6

reveals that 62% of the estimated AOD (670 nm) has a deviation less than 0.01. This threshold in the deviation corresponds to the nominal error in the retrieval of AOD for AERONET network (Holben et al., 1998).

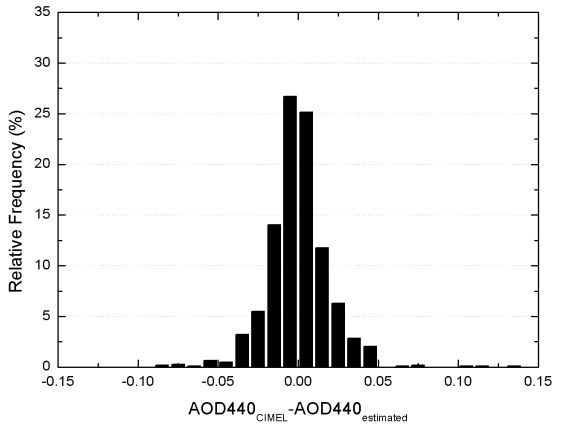

Figure 6.5. Histogram of the differences between measure and estimated values for AOD at 440 nm.

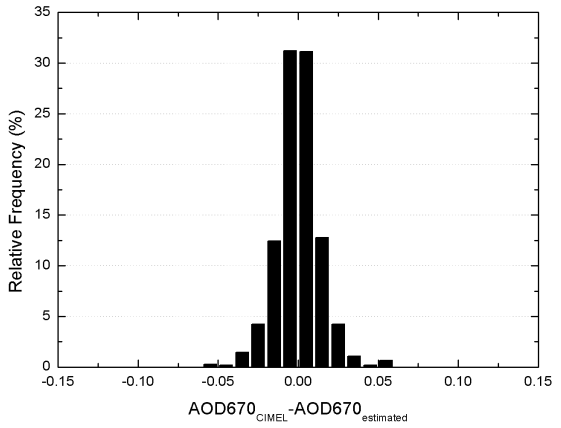

Figure 6.6. Histogram of the differences between measure and estimated values for AOD at 670 nm.

We also tried an ANOVA test for AOD estimation and the *p*-value is 0.976 at 440 nm and 0.93 at 670 nm, i.e. the measured and estimated AODs are indistinguishable with a 98% and 93% probability at 440 and 670 nm, respectively.

Figure 6.7 shows α estimated with the neural network, using the sky radiances in both channels (red and blue) of the sky images, versus α calculated with the CIMEL CE318 in the interval 440-1020 nm. The performance of the model was evaluated using the R^2, RMSD and the MBD, and Table 6.1 shows these statistics of the analysis.

Finally, Figure 6.8 shows a histogram of the differences between measured and estimated values for α.

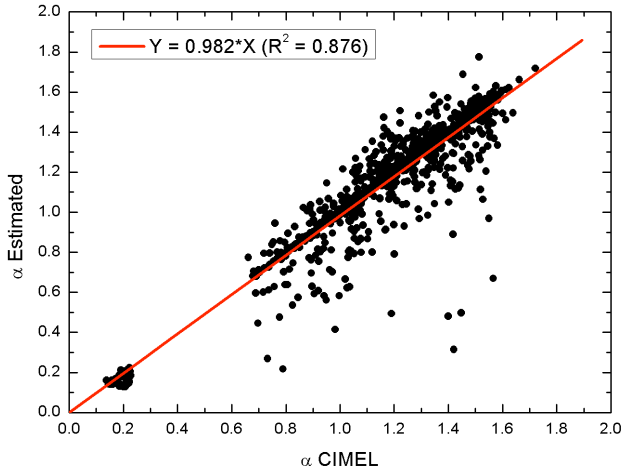

Figure 6.7. Scatter plot of estimated versus measured values for α.

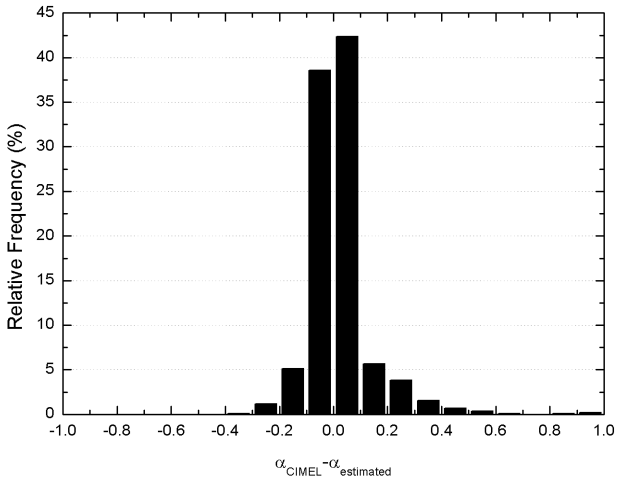

Figure 6.8. Histogram of the differences between measured and estimated values for α.

	b±error	R^2	MBD	RMSD
AOD440	0.985±0.004	0.872	7E-5	0.019
AOD670	0.976±0.005	0.847	1.3E-4	0.014
α	0.982±0.003	0.876	0.021	0.012

Table 6.1. Statistical results of the RBF networks for estimation of AOD at 440 nm, AOD at 670 nm and α. The column *b* represents the slope of the linear fitting through zero of the data and its error, R^2 is the coefficient of determination, MBD is the mean bias deviation and RMSD is the root mean squared deviation.

6.1.4.2 Whole Sky Imager

There is an important difference in the methodology for both instruments. While the input selection in the methodology for the All-Sky Imager followed intuition, for the Whole Sky Imager

there is an algorithm that selected the most adequate scattering angles. At the end, the greedy algorithm selected only one scattering angle for each AOD model.

For the blue WSI channel (450 nm associated to the 440 nm AOD), it selected the 37º scattering angle. Therefore the model has two inputs: the sky radiance at that scattering angle over the principal plane and the SZA. 117 measurements had to be eliminated from the original 1047 measurements due to shadow system obstruction, so the model was created from the remainder of this set with 930 measurements. For the red WSI channel (650 nm associated to the 675 nm AOD) selected the 71º scattering angle. The number of valid measurements after applying the mask is 968. Finally, for the NIR WSI channel (800 nm associated to the 870 nm AOD) selected the 83º scattering angle. The number of valid measurements is 973 in this case.

Figure 6.9, 6.10, and 6.11 show estimated values of AOD at 440, 675 and 870 nm, respectively, versus calculated values of AOD with the CIMEL at those wavelengths. The analysis has been done over the test set. The linear fit was also forced through zero so the slope provides information about the over- or underestimation associated with the model. Table 6.2 shows the statistics for the three models. Figure 6.12 shows histograms of the differences between measured and estimated AOD at 440, 675 and 870 nm.

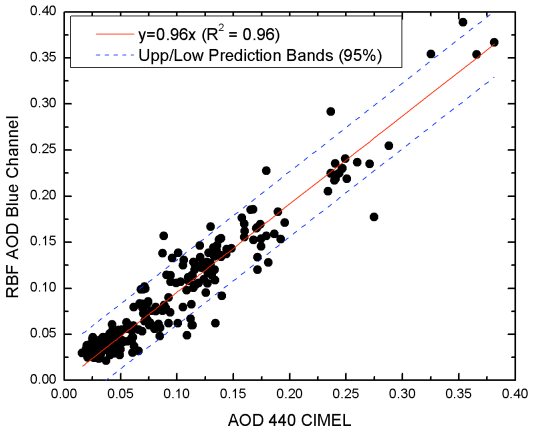

Figure 6.9. Scatter plot of estimated AOD values from the WSI versus values calculated from the CIMEL CE318 for 440nm. The line represents the linear fit through zero and the dashed lines are the upper and lower prediction bars at 95%.

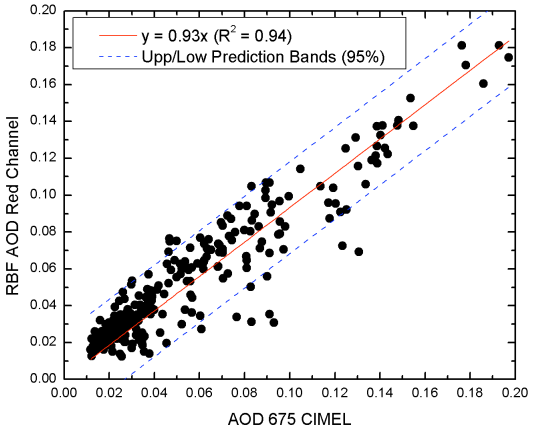

Figure 6.10. Scatter plot of estimated AOD values from the WSI versus values calculated from the CIMEL CE318 for 675nm. The line represents the linear fit through zero and the dashed lines are the upper and lower prediction bars at 95%.

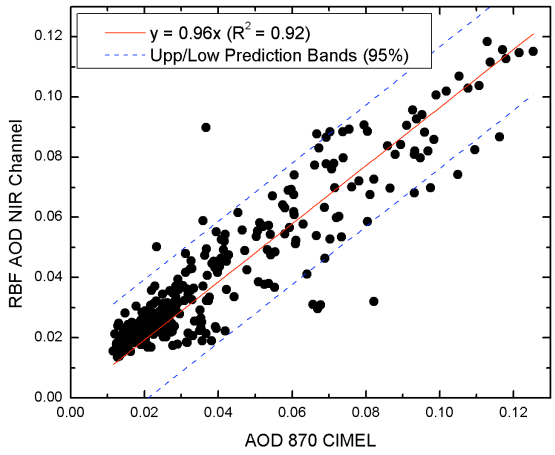

Figure 6.11. Scatter plot of estimated AOD values from the WSI versus values calculated from the CIMEL CE318 for 870nm. The line represents the linear fit through zero and the dashed lines are the upper and lower prediction bars at 95%.

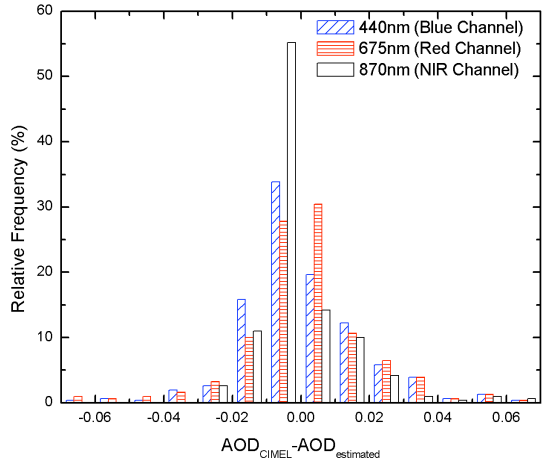

Figure 6.12. Histogram of the differences between calculated (from CIMEL CE318 measurements) and estimated values for AOD at 440, 675 and 870 nm.

	Set size	Scattering angle	b	R^2	MBD (%)	RMSD
AOD440	930	37º	0.96	0.96	-2	0.05
AOD675	968	71º	0.93	0.94	-1	0.07
AOD870	973	83º	0.96	0.92	3	0.07

Table 6.2. Statistical results of the RBF networks for estimation of AOD at 440, 675 and 870 nm. The column *b* represents the slope of the linear fitting through zero of the data, R^2 is the coefficient of determination, *MBD* is the mean bias deviation and *RMSD* is the root mean squared deviation.

As we can see in figure 6.9 and table 6.2, 96% of the data variance is explained by the model that estimates the AOD at 440 nm. MBD and the slope of the linear fit reveal a slight systematic underestimation. Figure 6.12 shows a histogram of the differences between the calculated and estimated values. It reveals that 81% of the estimated AOD values at 440 nm had a deviation less than 0.01 with respect to the CIMEL result, which is the AERONET AOD estimated uncertainty (Holben et al., 1998).

Figure 6.10 and Table 6.2 reveal that 94% of the data variance is explained by the model that estimates the AOD at 675 nm. MBD and the slope of the linear fit also indicate a slight systematic underestimation. Figure 6.12 shows that almost 80% of the estimated AOD at 675 nm has a deviation less than 0.01.

Finally, figure 6.11 and table 6.2 reveal that 92% of the data variance is explained by the model that estimated the AOD at 870 nm. While MBD suggests a slight overestimation, the slope of

the linear fit indicates an underestimation. Figure 6.12 shows that 90% of the estimated AOD at 870 nm has a deviation less than 0.01.

Figure 6.9, 6.10 and 6.11 reveal that the data set is not homogeneously distributed along the whole range of values. There are a lot of points with low AOD and very few with higher AOD. This can explain the slight systematic underestimation of the model. The linear fit is forced to zero and there are a lot of points close to zero, but the very few values far from the zero introduce a variance that, in this case makes the slope be slightly below 1.

The coefficient of determination decreases when we estimate AOD at longer wavelengths. This can be because of the difference between the central wavelength of the filters of the WSI and the CIMEL increases with the wavelength. That is, the AOD at 440 nm, is estimated with the measurements at 450 nm (10 nm of difference), the difference is 25 nm for AOD at 675 nm and it is 70 nm for AOD at 870 nm. In other words, at 440 and 675 nm there is an overlapping of the filters because of the FWHM of the WSI filters is 70 nm, but at 870 nm the filters do not overlap, hence this can produce a decrease in performance.

For the α estimation, figure 6.13 shows estimated versus calculated values of α with the CIMEL in the interval 440-870 nm using the linear fitting procedure. Figure 6.15 shows the histogram of the differences between calculated and estimated α. Figure 6.13 reveals that 63% of the data are explained by the model

that estimated α. Figure 6.15 shows that 48% of the estimated α has a deviation less than 0.1, which is the estimated uncertainty in the AERONET procedure for α calculation (Holben et al., 1998).

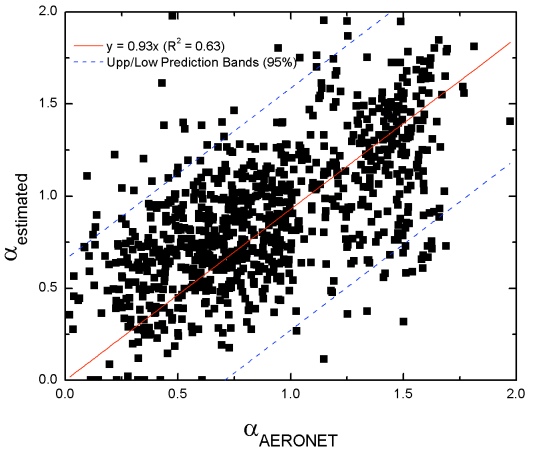

Figure 6.13. Scatter plot of estimated versus measured values for α (440-870 nm) using the AERONET standard procedure over the whole data set.

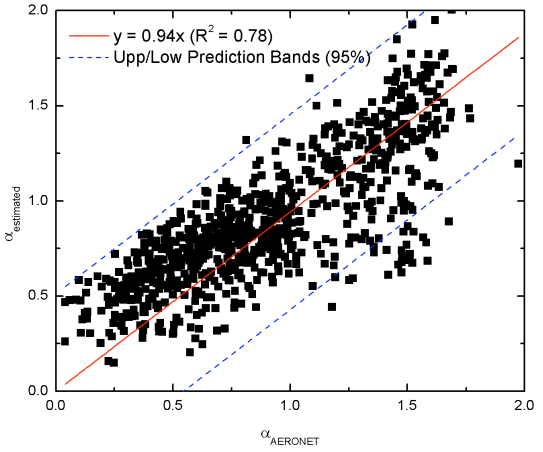

Figure 6.14. Scatter plot of estimated versus measured values for α (440-870 nm) using a neural network-based model with RBFs over the test set.

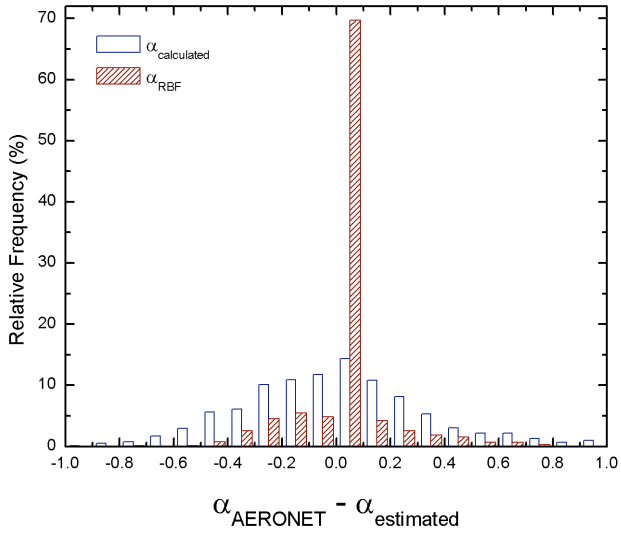

Figure 6.15. Histogram of the differences between measured and estimated values for α (440-870nm) for both methods.

The α estimation affected by the error introduced in the AOD estimation. The AOD at 870 nm introduces an error in the calculation of α by linear fitting of ln(AOD) vs wavelength. For this reason, we tried a new neural network-based model using RBF networks to estimate the value of α using the radiance over the principal plane of the sky images for the three wavelengths. The inputs for this model are the same for the estimation of the AOD together, i.e. we combined the radiance at different scattering angles over the principal plane for the three wavelengths, and the SZA. The model is trained and validated to calculate α in the interval 440-870 nm in the same way the model for the AODs were created. Figure 6.14 shows estimated versus CIMEL calculated values of α in the interval 440-870 nm using this method. Figure 6.15 shows the

histogram of the differences between measured and estimated α. Figure 6.14 reveals that 78% of the data are explained by the model that estimates α. Figure 6.15 shows that 84% of the estimated alpha has a deviation less than 0.1, which is the estimated uncertainty in the AERONET procedure for α calculation. This represents a clear improvement in the estimation of α from WSI images.

Even though the uncertainty in the estimation of α is large with the standard method, the estimation is still useful for the interpolation of the AOD at different wavelengths. We have tested it calculating the AOD at 500 nm with α and β estimated with the first method using Ångström law (Ångström, 1964) and compared it with the AOD at 500 nm obtained from CIMEL CE318 measurements. Figure 6.16 show estimated values of AOD at 500 nm versus calculated values of AOD with the CIMEL. 96% of the data variance is explained by the model that estimates the AOD at 500 nm.

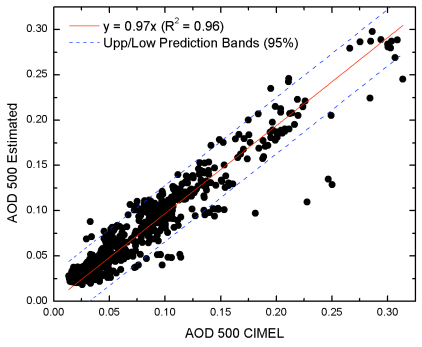

Figure 6.16. Scatter plot for estimated versus measured values for AOD at 500 nm. The estimation has been done using α and β calculated with the standard AERONET procedure with the estimated values of AOD with the neural network-based model.

As we can see, the use of this estimation yields a very good estimation of AOD in different wavelengths (one of the main usefulness of α).

6.2 Microphysical properties of the atmospheric aerosol

A relationship between the size of atmospheric aerosol particles and the wavelength dependence of the extinction coefficient was first suggested by Ångström (1929). Since that time, Ångström law (equation 2.23) has been directly related to a parameter of a Junge size distribution when the radii extend from 0 to infinity (van de Hulst, 1957; Junge, 1955). Curcio (1961) use the wavelength dependence of the particulate extinction coefficient in the visible and near-infrared regions to infer the aerosol size distribution existing above water in the Chesapeake Bay area. He determined that the majority of aerosol size distributions could best be represented by a two-component size distribution consisting of a Junge-type distribution plus a small component of larger particles. This type of composite distribution was the most capable of explaining the wavelength dependence of the attenuation measurements he observed.

Yamato and Tanaka (1969) were the first to apply a numerical inversion algorithm to spectral measurements of extinction coefficient in order to determine an aerosol size distribution. These authors applied the linear inversion techniques developed by Phillips (1962) and Twomey (1963) to the problem of

numerically solving the Fredholm integral equation of the first kind which arises in this problem (see equation 6.5 in next section). Although they clearly demonstrated that these numerical procedures are quite successful for obtaining size distributions by remote sensing, other investigators have still continued to estimate parameters of model size distribution from spectral attenuation measurements (e.g. Quenzel, 1970; Shaw et al., 1973). Although these fitting procedures are reasonably satisfactory, they are more restrictive than inversion procedures in that they assume that the atmospheric particulates follow one of several possible analytical distributions.

Grassl (1971) presented an iterative method for numerically inverting spectral attenuation data. After demonstrating the success of this algorithm on spectral attenuation coefficients generated for three model size distributions, he presented the size distributions obtained by inversion of two real data cases.

In order to accurately determine aerosol size distributions from spectral optical depth measurements obtained from direct solar observations, it is necessary to collect optical depth measurements over a sufficient number of wavelengths to obtain a good estimate of both the ozone absorption and particulate optical depths separately. In making these corrections, Grassl (1971) used tabulated values for a model atmosphere instead of alternative observations.

6.2.1 King's inversion code

An earlier theoretical study from Herman et al. (1971) of angular scattering intensities was extended by King et al. (1978) to the problem of inferring columnar aerosol size distribution by inversion of spectral optical depth measurements. An inversion formula which explicitly includes the magnitudes of the measurements variances was derived and applied to optical depth measurements with a solar radiometer.

The spectral dependency of the aerosol optical depth contains information about the size distribution of the aerosol (e.g. Heintzenberg et al., 1981; Wang et al., 1989). Following Mie's theory and considering that atmospheric aerosol is composed by spherical particles with a unique refraction index, *m*, we can determine the columnar size distribution through the spectral variation of the aerosol optical depth. Starting with equations 2.4 and 2.11 we have

$$\delta_{a\lambda} = \int_{z_1}^{z_2} \int_{r_1}^{r_2} \pi r^2 Q_e(r,\lambda,m) n(r) dr dz \qquad (6.4)$$

and, considering the radii limits between 0 and the infinity and performing the height integration, equation 6.4 can be rewritten as

$$\delta_{a\lambda} = \int_0^{\infty} \pi r^2 Q_e(r,\lambda,m) n_c(r) dr\,, \qquad (6.5)$$

where $n_c(r)$ is the unknown columnar aerosol size distribution, i.e. the number of particles per unit area per unit radius interval in a vertical column through the atmosphere, the extinction coefficient

Q_e has been rewritten showing the dependency with the radius r and the wavelength λ separately, and m is the refraction index.

To determine $n_c(r)$, the transform of equation 6.5 must be obtained. Since an expression for $n_c(r)$ cannot be written analytically as a function of the $\delta_{a\lambda}$ values, a numerical approach must be followed. Therefore, the integral in equation 6.5 is replaced by a summation over coarse intervals in r, each of which is composed of several subintervals as described by Herman at al. (1971) for the case of the angular distribution of scattered light of one wavelength. In order to examine the specific kernel functions, which result if that procedure is applied to the present problem, we let $n_c(r) = h(r)f(r)$, where $h(r)$ is a rapidly varying function of r and $f(r)$ is more slowly varying. With this substitution, equation 6.5 becomes

$$\begin{aligned}\delta_{a\lambda} &= \int_{r_a}^{r_b} \pi r^2 Q_e(r,\lambda,m) h(r) f(r) dr = \\ &= \sum_{j=1}^{q} \int_{r_j}^{r_{j+1}} \pi r^2 Q_e(r,\lambda,m) h(r) f(r) dr\end{aligned} \tag{6.6}$$

where the limits of integration have been made finite with $r_1=r_a$ and $r_{q+1}=r_b$. If $f(r)$ is assumed constant within each coarse interval, a system of linear equations results which may be written as

$$g = Af \tag{6.7}$$

In order to take into account the error from the approximation, we have to add a term to equation 6.7. Thus the equation has the form

$$g = Af + \varepsilon, \tag{6.8}$$

where ε is the unknown error vector whose elements ε_l represent the deviation between the measurements (g_i) and the estimation ($\Sigma_j A_{ij} f_j$). This deviation arises from quadrature and measurement errors, as well as any unvcertainties as to the exact form of the kernel function (in this case $\pi r^2 Q_e(r,\lambda,m)$).

Returning to equation 6.6, the elements of equation 6.8 are given by

$$g_i = \delta_{a\lambda i}, \qquad i=1,2,\ldots,p$$

$$A_{ij} = \int_{r_j}^{r_{j+1}} \pi r^2 Q_e(r,\lambda_i,m)h(r)dr, \qquad j=1,2,\ldots,q \tag{6.9}$$

$$f_j = f(r_j \le r \le r_{j+1})$$

In terms of an integral over $x=\log r$, equation 6.9 may be rewritten as

$$A_{ij} = \int_{x_j}^{x_{j+1}} K(x,\lambda_i)dx, \tag{6.10}$$

where

$$K(x,\lambda) = \pi 10^{3x} Q_e(10^x,\lambda,m)h(10^x)\ln 10. \tag{6.11}$$

Equations 6.10 and 6.11 are those obtained by Yamamoto and Tanaka (1969) if $h(r)$ takes the form of a Junge size distribution (Junge, 1955),

$$h(r) = r^{-(\nu+1)}, \tag{6.12}$$

with ν assumed to have a value of 3.0.

Phillips (1962) and Twomey (1963) have discussed the instability in the solution vector f which results if equation 6.8 is directly solved by minimizing $\Sigma\varepsilon_i^2$. Phillips suggested that, due to ever-present error, a constraint be added that discriminates against such instability. In order to select a physical solution among the family of solutions that satisfy equation 6.8, Phillips introduced a smoothing constraint such that the sum of the squares of the second derivatives of the solution points is minimized. For a quadrature of equal division, the solution vector f is obtained by minimizing a performance function Q, defined as

$$Q = \sum_{i=1}^{p} \varepsilon_i^{\,2} + \gamma \sum_{j=2}^{q-1} (f_{j-1} - 2f_j + f_{j+1})^2, \tag{6.13}$$

where γ is some non-negative Lagrange multiplier. Minimizing Q with respect to the unknown f_k coefficients, when γ equals zero, is equivalent to making an unweighted least-squares fit to the data.

Since it is further known that some of the $\delta_{a\lambda}$ measurements are more precise than others, it is desirable to include that information in the mathematical formalism. For the case in which the measurements are correlated with known covariances $\sigma^2_{g_i g_j}$, a more general form of equation 6.13 would be

$$Q = \sum_{i=1}^{p}\sum_{j=1}^{p} C_{ij}^{-1}\varepsilon_i\varepsilon_j + \gamma\sum_{j=2}^{q-1}(f_{j-1} - 2f_j + f_{j+1})^2 , \qquad (6.14)$$

where $C_{ij}=\sigma^2_{gi\,gj}$ is an element of the measurement covariance matrix C. This follows from the Gauss-Markov theorem in the absence of a constraint (e.g. Liebelt, 1967), and thus the minimum value of Q represents the statistically optimum estimate of f.

Following the method suggested by Twomey (1963) whereby the performance function is differentiated with respect to each of the f_k coefficients, a set of simultaneous equations results, which may be written as

$$-\sum_{i=1}^{p}\sum_{j=1}^{p} C_{ij}^{-1}A_{ik}\varepsilon_j + \gamma\sum_{j=1}^{q} H_{kj}f_j = 0 \qquad k= 1,2,\ldots,q \qquad (6.15)$$

where H_{kj} is an element of the smoothing matrix H defined by Twomey (1963).

Writing the series of equations 6.15 in matrix for, we have:

$$-A^T C^{-1}\varepsilon + \gamma H f = 0, \qquad (6.16)$$

where A^T is the transpose of A. Eliminating ε leads to the solution of f

$$f = (A^T C^{-1}A + \gamma H)^{-1} A^T C^{-1} g. \qquad (6.17)$$

The iterative method proposed by King et al. (1978) begins guessing an initial solution that is updated every iteration. The process is repeated until a stable solution is reached. This method considers that the initial function has the shape of a Junge distribution (equation 6.12) related to the Ångström parameter by equation $v=\alpha - 2$. Normally, several values of v are used to calculate the initial function and they are compared to the final results. The lagrange parameter γ enters (equation 6.17) in a manner such that elements of γH are to be added to $A^T C^{-1} A$ to produce the desired smoothing, the magnitude of $\gamma H_{kj}/(A^T C^{-1} A)_{kj}$ is of importance, not the magnitude of γ alone. In selecting γ, therefore, $\gamma_{rel} \equiv \gamma H_{11}/(A^T C^{-1} A)_{11}$ is allowed to vary in the range 10^{-3} to 1 until a minimum value of γ_{rel} is reached for which elements of the solution vector f are positive (negative values of the elements of f constitute an unphysical solution).

King et al. (1978) discussed the difficulties associated with the use of inversion of spectral measurements of aerosol optical depth in order to obtain the aerosol columnar size distribution. We note important among these difficulties the election of the radii range that contribute the most to the values of optical depth. These authors showed that the radii that contribute most significantly to the magnitude of the Mie optical depth measurements vary somewhat with the type of the size distribution to be retrieved. Satisfactory size distribution determinations can normally be obtained for the radii range 0.1 μm < r < 4.0 μm when measurements are available for wavelengths throughout the visible and near-infrared regions.

Another difficulty is the sensitivity of the distribution function to the refractive index. In general, the shape of the size distribution does not change with the refractive index (King et al., 1978; Gonzalez and Ogren, 1996 and Martinez-Lozano et al., 1999)

6.2.2 Results and evaluation

Before we run the inversion code we have to select a refractive index. As it was stated before, the results do not significantly change with the refractive index. Literature establishes commonly used default values (e. g. D'Almeida et al. 1991 and Martinez-Lozano et al., 1999), so a value of $1.5 - 0.0005i$ was selected.

The wavelengths used and the corresponding AODs are given by the instrument. WSI provides 3 wavelengths and we estimated in section 6.1.2.2 the AOD at those wavelengths (440, 670 and 870 nm). Also, the Ångström coefficients α and β are calculated in section 6.1.3.2 so we can estimate AODs at other wavelengths. On the other hand we compared the results with the size distributions given by the CIMEL CE318 using the five wavelengths available (380, 440, 670, 870 and 1020 nm).

Figure 6.17 shows three examples of size distribution calculated with the King's inversion code for days with different AODs and α. Size distribution has been estimated using the WSI with 3 wavelengths, also with 5 wavelengths (estimated with the

Ångström coefficients α and β) and with the CIMEL using 5 wavelengths.

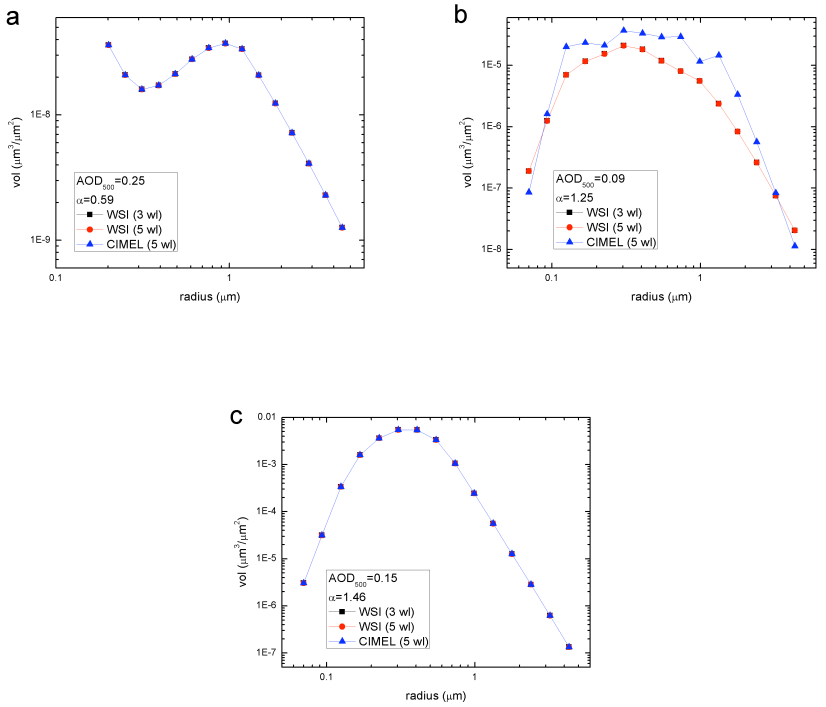

Figure 6.17. Size distribution for (a) December 18th 2001, (b) June 6th 2002 and (c) July 25th 2002 calculated with King's inversion code using the WSI and the CIMEL CE318 with 3 and 5 wavelengths

As we can see, the distributions are exactly the same for two of the cases and it is different for the case with lower AOD.

In order to compare the results for a large data set we need a different estimator than the visual inspection of the size distributions. The effective radius is the ratio between size distribution function momentums and constitutes a parameter that

describes radiatively the size distribution. In other words, if all the particles would have the effective radius, the radiative response would be the same as the radiative response of the actual size distribution.

$$r_e = \frac{\int_0^\infty r^3 n(r) dr}{\int_0^\infty r^2 n(r) dr} \tag{6.18}$$

The same data set used in section 6.1.2.2 is used here to calculate the size distribution. Over 900 cases are calculated using the WSI with 3 and 5 wavelengths and the CIMEL using 5 wavelengths.

Figures 6.18 and 6.19 show frequency histograms of the difference between the effective radius of the WSI size distributions and the effective radius of the CIMEL distributions. Figure 6.18 uses 3 wavelengths for the WSI and figure 6.19 uses 5 wavelengths for the WSI.

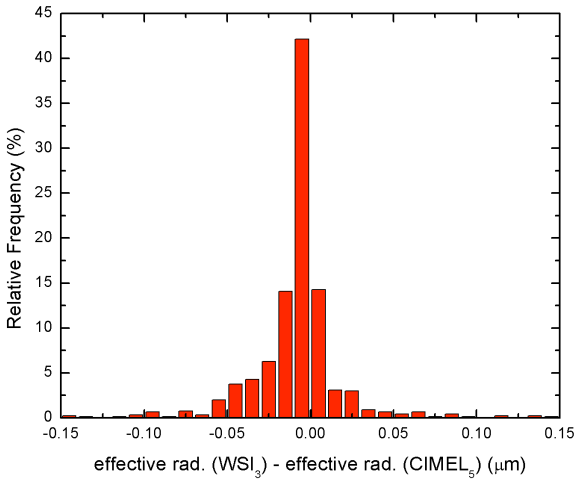

Figure 6.18. Histogram of the differences between WSI effective radius and CIMEL effective radius using 3 wavelengths in the WSI (440, 670 and 870 nm) and 5 wavelengths in the CIMEL (380, 440, 670, 870 and 1020 nm).

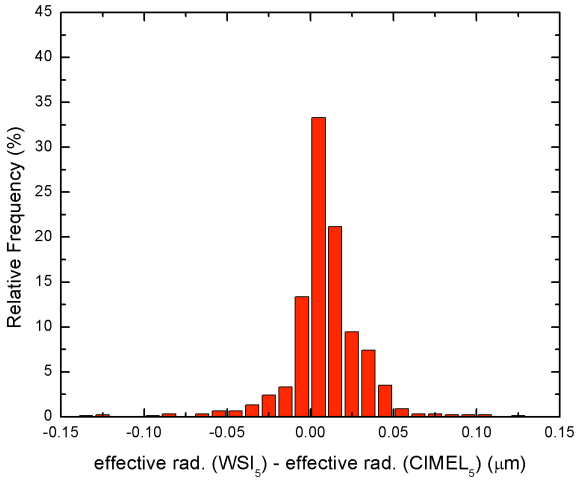

Figure 6.19. Histogram of the differences between WSI effective radius and CIMEL effective radius using 5 wavelengths in both instruments (380, 440, 670, 870 and 1020 nm).

The goodness of the effective radius estimation using the WSI compared to the CIMEL can be evaluated with some statistical analysis over the data sets and the histograms. First, the whole CIMEL data set has an effective mean radius of $\bar{r}_e = 0.093$ μm and the standard deviation is $\bar{\sigma} = 0.021$ μm, which means that the standard deviation is about 22%. Then, performing a Gaussian fitting on the histogram in figure 6.18 (WSI with 3 wavelengths) we obtain that the center of the Gaussian is x_{c3} = -0.0026 μm with σ_3 = 0.008 μm. The same fitting for figure 6.19 (WSI with 5 wavelengths) are x_{c5} = 0.0072 μm and σ_5 = 0.0204 μm.

These statistics values show that the effective radius calculated using the WSI with 3 wavelengths underestimates the CIMEL effective radius in a 2.8% ($(x_{c3}/\bar{r}_e)*100$) and its deviation is lower than the standard deviation of the CIMEL data set ($\sigma_3 < \bar{\sigma}$), or we can also say that the standard deviation is about 8.6%. Using 5 wavelengths, the calculation of the effective radius overestimates the CIMEL effective radius in a 7.7% ($(x_{c5}/\bar{r}_e)*100$) and its deviation is again lower than the standard deviation ($\sigma_5 < \bar{\sigma}$) or, again, the standard deviation is about 22%.

Now, let us try to find in what cases there is a difference in the effective radii or, in other words, what factors influence the size distribution estimation for both instruments the CIMEL and the WSI. It seems to be clear, as shown in figure 6.17, that smaller values of AOD introduce a difference in the size distribution that does not happen for larger values. Figure 6.20

(using 3 wavelengths) and figure 6.21 (using 5 wavelengths) show that, for the whole data set, smaller values of AOD introduce more uncertainty in the effective radius estimation.

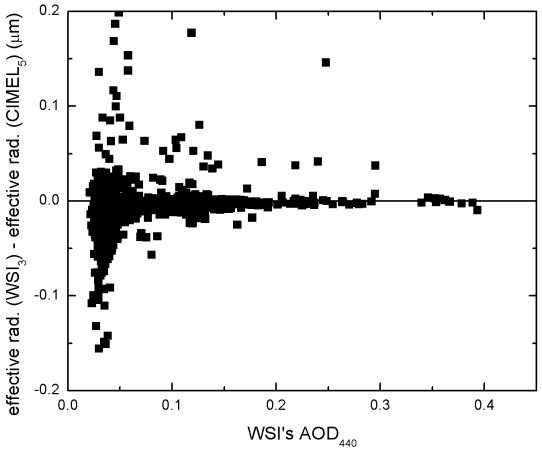

Figure 6.20. Difference of effective radius estimation (WSI – CIMEL) using 3 wavelengths versus AOD at 440 nm.

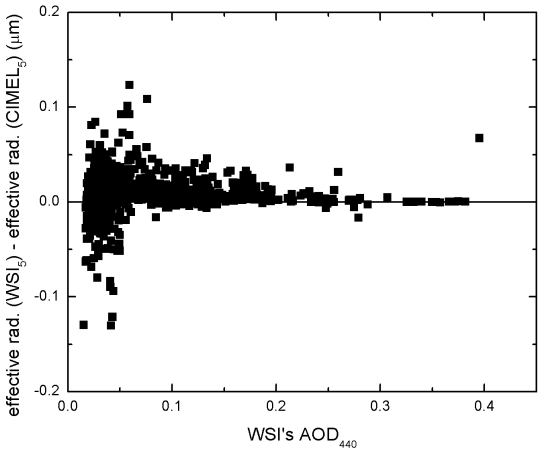

Figure 6.20. Difference of effective radius estimation (WSI – CIMEL) using 5 wavelengths versus AOD at 440 nm.

We saw that the error using 5 wavelengths is about 5% larger than using 3 wavelengths and, figure 6.21 shows that the reason is the error in the estimation of the Ångström α coefficient. The figure shows the difference of effective radius versus the difference of α coefficient.

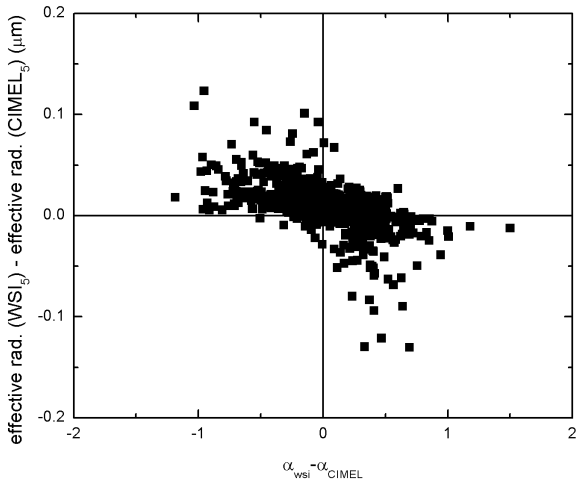

Figure 6.21. Difference of effective radius estimation (WSI – CIMEL) using 5 wavelengths versus difference of α coefficient.

The uncertainty in the effective radius is larger when there is a difference in the α coefficient. Moreover, when the α coefficient is underestimated, the effective radius is overestimated, and vice versa.

Summarizing, in all cases the effective radius of the size distributions estimated is inside the standard deviation of the CIMEL estimated effective radius (22%), and the mean value of

effective radius has a difference less than 8% respect to the CIMEL estimated effective radius.

7

Conclusions

This last chapter presents the concluding remarks. First of all, we present a brief summary of the sky imager itself. Then, the methodology for cloud detection and aerosol characterization are explained separately. Second section presents a discussion on the cloud detection algorithm and its results. Third section shows the discussion on the aerosol characterization for both instruments, the All-Sky Imager and the Whole Sky Imager splitting between the optical properties and the microphysical properties.

Finally, fourth section summarizes the future lines to follow.

7.1 The All-Sky Imager

We have succeeded in the endeavor of designing and deploying a sky imager. Starting from the election of an appropriate CCD sensor and lens, followed by the shadow system (a sun tracker), and the design of the environmental housing and the election of a temperature controller. Moreover, the system is fully automated, capturing images during daytime and storing them in the computer. The analysis of images is performed in real time, and also stored in the computer and available in a website also designed for the purpose of having the data accessible to the community.

7.2 Cloud cover characterization

The use of sky imagery offers better resolution in space and time than does human observation. The All-Sky Imager captures an image every 5 minutes every day of the year. On the other hand, human observers estimate cloud cover in oktas, or ranges of oktas as in METAR reports, with a degree of subjectivity. The analysis procedure of the images of the All-Sky Imager, the multilayer perceptron (MLP), includes subjectivity in the election of the training set and the classification of it, i.e., the human interaction in the process. Beyond this, the MLP always acts objectively according to the learning process and provides a good way to determine cloud cover with quite good resolution as demonstrated in the comparison with the METAR records. The apparent complexity of the algorithm provides the added value of cloud classification into two classes

(thin and opaque clouds). Another added value is spatial classification. The procedure provides as output an ASCII file including the spatial classification in oktas, the cloud class (thin or opaque), and the apparent Sun octant position, as well as the processed image. Such results are important for the characterization of cloud effects on UV radiation, since thin clouds that nearly obstruct the Sun can enhance UV radiation.

The error rate of the classifier is given in percent of pixels, but the final procedure classifies images. The error is always gathered in specific regions. Observing the image results, it is revealed that the circumsolar area is very difficult to classify. Currently, the MLP always classifies the brightness of the Sun as cloud, and this uncertainty is bigger in the case of dust events (or under large aerosol load). This also hinders the possibility of detecting solar obstruction by clouds, especially in our location where dust outbreaks are frequent. The ability of the human classifier to distinguish between thin clouds and sky or opaque clouds is also a source of error.

The usefulness of the genetic algorithm for parameter optimization is clearly demonstrated. The final prototype has 1/6 of the original number of required inputs, increasing the speed of the execution of the procedure for cloud cover estimation, and the performance of the MLP is also slightly increased. One of the most important conclusions we can extract from the results of the optimization algorithm is that the information required for cloud detection is in the red and blue channels, as in the red/blue ratio

threshold method, and the classification of thin and opaque clouds requires the use of the variance, which is a texture parameter.

The main problems in the design of the MLP are the election of the training set and its classification. This election affects the performance of the MLP drastically. It is important to select a wide variety of conditions and classify them properly. The use of this technique in other locations might require repeating the training process as well.

The main weaknesses of the MLP cloud classification of sky images are found in the circumsolar area and at cloud edges. The circumsolar area is important because of the UV enhancement effect, as stated above. The solution of the circumsolar area problem may be difficult because the brightness of that area nearly saturates the pixels and blinds the imager, making it impossible to see what is behind the brightness, especially during dust events. The problem at cloud edges includes bias by the human observer.

This methodology and specially the input selection algorithm using genetic algorithms could be used for a more complex cloud classification algorithm that includes all or some of the clouds *generas*. A cloud detection algorithm as the red/blue ratio or the methodology here explained could be combined with a cloud classification algorithm to provide a more complete characterization of the cloud cover.

7.3 Aerosol characterization

7.3.1 Optical properties

The All-Sky Imager and the Whole Sky Imager (WSI) have been tested for aerosol optical properties characterization. Both aerosol optical depth (AOD) and Ångström exponent have been estimated and compared with the results estimated with the sun photometer CIMEL CE318.

The All-Sky Imager is a non-calibrated system, but the linearity of the CCD-based systems allows relating the pixel counts of the imager with sky radiance and a neural network-based model estimates the values of AOD and Ångström exponent using the sky radiance at specific scattering angles in the principal plane. The models for AOD provide estimations that, according to the validation, are within the limits of nominal precision of AERONET (±0.01) in 52% of the cases for AOD-440 and 62% of the cases for AOD-670. In the case of the Ångström exponent, about 80% of the cases have deviations below 0.1 (limits of nominal precision of AERONET).

The neural network-based models are very sensitive to the training set. The data sets do not have many cases with high AOD or small Ångström exponent (coarse particles such as dust) so a larger data set with a wider range of values for AOD and Ångström exponent is required for a training that would yields to an applicable methodology.

This first approach is very promising and demonstrates the merits of the method, so the methodology was applied to a calibrated sky imager, the WSI, using a larger data set and a procedure to select the optimal scattering angles along the principal plane. Three neural network-based models have been created to estimate the value of the AOD at three different wavelengths using the radiance over the principal plane of the sky images. The correlation constants are close to unity and the number of cases within measurement error is very large. Only one scattering angle per channel has been used: 37°, 71° and 83° corresponding to the blue, red and NIR channel respectively. The three AOD models provide an estimation that, according to validation, is inside the nominal error of the AERONET (±0.01) in approximately 80% for the blue and red channels and 90% for the NIR channel. In all cases the models explain up to 92% of the variance of the experimental data. The coefficient of determination decreases when we estimate AOD at longer wavelengths. This can be caused by the difference between the central wavelength of the filter in the sky imager and the CIMEL. This difference is larger with longer wavelengths and, therefore, the overlap of the wavelength decreases and so the performance. Nevertheless, all estimations have a coefficient of determination over 0.92.

The estimation of the Ångström exponent has been performed in two ways. First, it has been calculated applying a linear fit as explained in section 6.1.3 using the AODs estimated with the neural network and secondly, it has been estimated with a

new neural network-based model using RBF networks. Inputs to this RBF network are the radiances in the same scattering angles used for the AOD models. The α estimation using the linear fit is affected by the cumulative error of all the AOD estimations. However, almost 50% of the data are inside the nominal error of the AERONET program for α calculation using the standard procedure in AERONET. The neural network-based model for estimation increases the explanation of the data to 63% and the data inside the nominal error is increased to 78%. The neural network process is complex but increases substantially the estimation. The neural network model forces the result to be the same as that estimation of α in the interval 440–870 nm.

Concerning the scattering angles selected with the greedy algorithm, these reveal that to estimate the AOD at 450 nm (blue) it is necessary to use an angle relatively close to the sun. The estimation of the AOD at 870 nm (NIR) requires an angle farther from the sun. At 675 nm the behavior can be catalogued as in between of the behavior presented in the other two wavelengths. The reduction of angles needed respect to the methodology applied to the All-Sky Imager can be explained by the character of the measurements since they are calibrated radiances while the previous work used pixel counts.

The results are promising in the sense that it seems to be feasible that a sky imager can estimate the AOD and the algorithm could be applied in the field. Furthermore, we believe that this model might be applied to different WSIs in different locations

without a new training process since all the WSIs have an absolute radiance calibration and this proposed model directly relates spectral radiances in fixed geometries with AOD and, thus the underlying statistics of the data is similar to that of the training set used in this work. Nevertheless, this validation with different WSI datasets in different location might be undertaken in the future. The two methods for the α estimation differ, however we consider that the linear fit procedure is simple and useful for the interpolation of AODs at different wavelengths.

7.3.2 Microphysical properties

A complete aerosol characterization requires estimating microphysical properties. We have estimated the size distribution of the atmospheric aerosol using an inversion code. Inputs to the inversion code are the AODs estimated in the optical properties section for the WSI. The WSI yielded better results than the All-Sky Imager, and more AODs are available (3 versus 2 for the All-Sky Imager). Also the α exponent allows estimating the AOD at different wavelengths.

In order to evaluate the size distribution in a large data set, we use the effective radius of the WSI retrieved size distribution and the effective radius of the CIMEL CE318 size distribution. The differences between both effective radii are small using 3 wavelengths of the WSI and also using 5 wavelengths. This reveals that the size distributions estimated with both instruments have a

similar behavior from the radiative point of view. It is interesting to note that the differences between both instruments are more noticeable when the AOD values are smaller. The uncertainty of the size distribution is greater when the AOD values are smaller.

It is also manifest that using 3 wavelengths provide better results than using 5 wavelengths. This means that the α coefficient estimated with the WSI introduces more error than using fewer wavelengths.

Concluding, we can say that these good results strengthen the results obtained for the optical properties. On one hand, the AODs estimated are good enough to provide realistic size distributions compared to the ones estimated with the CIMEL CE318 (2.8% of error in the mean effective radius) and the standard deviation of the whole data set is almost 3 times smaller than the standard deviation of the CIMEL CE318 estimated effective radius (8.6% compared to 22%). On the other hand, the α and β coefficients calculated using the linear fit provides fair estimation of AODs at different wavelengths since the size distributions obtained including those interpolated AODs slightly reduce the agreement of the size distribution comparison (about 5% more error than using only 3 wavelengths) and the standard deviation is about the same than the CIMEL CE318 estimated effective radius (22%).

The capabilities of sky imagers for aerosol characterization are demonstrated. Nevertheless the potential of these instruments go further. A calibrated sky imager provides the

sky radiance at every scattering angle in the sky dome, and the information over the almucantar or principal plane can be used to feed a more complex inversion code that also would provide other useful properties from the radiative perspective such as the single scattering albedo, the phase function or the asymmetry factor. In this sense, King's inversion code is robust as does not require too much, since we only need the AOD, the sources of error are smaller than a more complex code that also requires the sky radiance as an input. Preliminary tests revealed many difficulties in the convergency of the algorithms, but this is an open field for possible future investigations.

7.4 Future work

Here is a summary of the improvements and future work already noted in previous sections of this chapter.

The next logical step in the cloud cover characterization is the classification in different types of clouds. With the past experience, we can define new features from the sky images, specially texture features, that could be input to a new neural network with the idea of classifying all, or a subgroup of, cloud *generas*. The usefulness of the genetic algorithm could be use here again to optimally select the inputs.

Another problem related to cloud cover characterization is the circumsolar area. Treating this area

separately, and defining specific algorithms could improve the classification in this area.

Our system, the All-Sky Imager, has a partial geometric calibration and no absolute radiance calibration. This is another subject for improvement. In order to perform quality aerosol characterization with our system, these calibrations are required.

Finally, the next step in the aerosol microphysical properties, would be the use of a more complex inversion algorithm taking advantage of the sky radiance in order to obtain more properties of the aerosol (e.g single scattering albedo, phase function or asymmetry factor).

References

Alados-Arboledas, L, H. Lyamani and F.J. Olmo (2003). Aerosol size properties at Armilla, Granada (Spain), Quarterly Journal of the Royal Meteorological Society Vol. 129(590) pp. 1395-1413.

Alados, I, J.A. Mellado, F. Ramos and L. Alados-Arboledas (2004). Estimating UV erythemal irradiance by means of neural networks, Photochem. Photobiol. 80, 351–358.

Alados, I, M.A. Gomera, I. Foyo-Moreno and L. Alados-Arboledas (2007). Neural network for the estimation of UV erythemal irradiance using solar broadband irradiance, International Journal of climatology Vol. 27(13) pp. 1791-1799.

Albrecht, B. (1989). Aerosols, cloud microphysics and fractional cloudiness. Science, 245, 1227–1230.

Ångström, A. (1964). The parameters of atmospheric turbidity. Tellus 16, 64–75.

Anon. (1995). Guía Resumida del Clima en España 1961-1990, Ministerio de Obras Públicas, Transporte y Medio Ambiente, Dirección General del Instituto Nacional de Meteorología.

Bais, A.F., C.S. Zerefos, C. Meleti, I.C. Ziomas and K. Tourpali (1993). Spectral measurements of solar UVB radiation and its relations to total ozone, SO2 and clouds, J. Geophys. Res., 98(D3), 5199–5204.

Barber, D. and C.M. Bishop (1997). Esemble learning for multi-layer networks. In Michael I. Jordan, Michael J. Kearns, and Sara A. Solla, editors, Advances in Neural Information Processing Systems 10, NIPS*97, pages 395-401, Denver, Colorado, USA, Dec. 1-6, 1997, 1998. The MIT Press

Barry, R.G. and R.J. Chorley (2003). Atmosphere, Weather and Climate (8th edition). Routledge.

Bener, P. (1964), Investigation on the influence of clouds on the ultraviolet sky radiation. Contract AF 61(052)-618, Tech note 3. Davos-Platz, Switzerland.

Berwick, M. and D. Kesler (2005). Ultraviolet radiation exposure, vitamin D, and cancer, Photochemistry and photobiology Vol. 81(6), pp. 1261-1266.

Bishop, C. M. (1995). Neural networks for pattern recognition. Oxford University Press, Oxford.

Bohren, C and D.R. Huffman (1983). Absorption and Scattering of Small Particles (1st edition). John Wiley and Sons, New York

Borkowski, J., A.T. Chai, T. Mo and A.E.O. Green (1977). Cloud effects on middle ultraviolet global radiation. Acta Geophys. Polonica, vol.XXV, no.4, pp.287-301

Bremermann, H. J. (1962). Optimization through evolution and recombination. In M. C. Yovits, G. T. Jacobi and G. D.

Goldstein (Eds.). Self Organizing Systems, pp. 93. Spartan Books. Washington DC.

Calbó, J., D. Pagès, and J.A. González (2005). Empirical studies of cloud effects on UV radiation: A review. Rev. Geophys., 43, RG2002.

Chen, T. and M. Takagi (1994). Cloud segmentation using unsupervised clustering algorithm, 7th Australasian Remote Sensing Conference, Melbourne, Australia, pp. 101-108.

Chou, M.D. (1991). The derivation of cloud parameters from satellite-measured radiances for use in surface radiation calculations, J. Atmos . Sci. vol. 48(13) pp. 1549-1559.

Chylek, G.M., B. Johnson, P.A. Damiano, K.C. Taylor and P. Clement (1995). Biomass burning record and black carbon in the GISP-2 ice core, Geophys. Res. Lett. 22(2), 89-92.

Chylek, P., and J. Wong (1995). Effect of absorbing aerosols on global radiation budget. Geophys. Res. Lett., 22(8), 929–931.

Cormen, T.H., C.E. Leiserson and R.L. Rivest (2001). Introduction to algorithms. MIT Press, Cambridge, MA.

Curcio, J.A (1961). Evaluation of atmospheric aerosol particles size distribution from scattering measurements in the visible and infrared, J. Opt. Soc. Amer Vol. 51, pp. 548-551.

D'Almeida G.A., P. Koepke and E.P. Shettle (1991). Atmospheric aerosols. Global climatology and radiative characteristics. A. Deepak Publishing, Hampton.

Dubovik, O., B.N. Holben, T.F. Eck, A. Smirnov, Y.J. Kaufman, M.D. King, D. Tanré and I. Slutsker (2002). Variability of absorption and optical properties of key aerosol types observed in worldwide locations, J. Atmos. Sci. 59, 590-608.

Dubovik, O., A. Sinyuk, T. Lapyonok, B.N. Holben, M. Mishchenko, P. Yang, T.F. Eck, H. Volten, O. Muñoz, B. Veihelmann, W.J. van der Zande, J.F. Leon, M. Sorokin and I. Slutsker (2006). Application of spheroid models to account for aerosol particle nonsphericity in remote sensing of desert dust. Journal of Geophysical Research 111: Art. No. D11208

Ebert, E.E. (1992). Pattern recognition analysis of polar clouds during summer and winter, Int. J. Remote Sens. Vol. 13(1), pp. 97-109.

Echalar, F., A. Gaudichet, H. Cachier and P. Artaxo (1995). Aerosol emissions by tropical forest and savanna biomass burning: characteristics trace elements and fluxes, Geophys. Res. Lett. 22(22), 3039-3042.

Estelles, V. (2006). Caracterización de los aerosoles atmosféricos en valencia mediante fotometría solar. Tesis Doctoral, Universidad de Valencia.

Estupiñán, J.G., S. Raman, G.H. Crescenti, J.J. Streicher, and W.F. Barnard (1996). Effects of clouds and haze on UV-B radiation, J. Geophys. Res., 101(D11), 16,807–16,816.

Forgan, B.W. (1994). General method for calibrating sun photometers. App. Opt. 33(21): 4841-4850.

Forster, P., V. Ramaswamy, P. Artaxo, T. Berntsen, R. Betts, D.W. Fahey, J. Haywood, J. Lean, D.C. Lowe, G. Myhre, J. Nganga, R. Prinn, G. Raga, M. Schulz and R. Van Dorland, (2007). Changes in Atmospheric Constituents and in Radiative Forcing. In: Climate Change 2007: The Physical Science Basis. Contribution of Working Group I to the Fourth Assessment Report of the Intergovernmental Panel on Climate Change [Solomon, S., D. Qin, M. Manning, Z. Chen, M. Marquis, K.B. Averyt, M.Tignor and H.L. Miller (eds.)]. Cambridge University Press, Cambridge, United Kingdom and New York, NY, USA.

Frederick, J.E. and H.D. Steele (1995). The transmission of sunlight through cloudy skies: An analysis based on standard meteorological information. J. App. Meteorol. vol 34, pp. 2755-2761

Gil, J.E., A. Cazorla, F.J. Olmo and L. Alados-Arboledas (2005). Experimental set up to study the cloud radiative effects on UVB at Granada (Spain), in Proceedings of the European Geosciences Union General Assembly, A. K. Richter, ed. (EGU, 2005) Vol. 1, EGU05-A-00320, AS1.08.1WE2P-0059.

Godar, D.E. (2005). UV doses worldwide, Photochemistry and photobiology Vol. 81(4), pp. 736-749.

Goldberg, D.E. (1989). Genetic algorithms in search, optimization and machine lerning. Addison-Wesley. Reading, MA

Gonzalez H. and J.A. Ogren (1996). Sensitivity of retrieved aerosol properties to assumptions in the inversions of spectral optical depth, J. Atmos. Sci. 53, 3669-3685.

Gonzalez, R.C. and R.E. Woods (1992). Digital image processing (3rd edition), Addison Wesley.

Goodman, A.H. and A. Henderseon-Sellers (1988). Cloud detection and analysis: A review of recent progress, Atmos. Res. Vol. 21, pp. 203-228.

Grant, W.B. and M.F. Holick (2005). Benefits and requirements of vitamin D for optimal health: A review, Alternative Medicine Review Vol. 10(2), pp. 94-111.

Grassl, H. (1971). Determination of aerosol size distribution from spectral attenuation measurements, Appl. Opt. 10, 2434-2538.

Guerrero-Rascado, J.L. F.J. Olmo, I. Aviles-Rodriguez, F. Navas-Guzman, D. Perez-Ramirez, H. Lyamani, L. Alados-Arboledas (2009). Extreme Saharan dust event over the southern Iberian Peninsula in september 2007: active and

passive remote sensing from surface and satellite, Atmospheric chemistry and physics 9(21) pp. 8453-8469.

Gutiérrez, J.M., R. Cano, A. S. Cofiño and C. Sordo (2004). Redes Probabilísticas y neuronales en las Ciencias Atmosféricas, Ministerio de Medio Ambiente, Dirección General del Instituto Nacional de Meteorología.

Harnett, C.M. (1992). Effect of Cloud Cover on the Surface Radiation Budget. MA thesis, Geography Department, University of Canterbury, New Zealand

Haykin, S. (1994). Neural Networks. MacMillan, New York.

Haywood, J.M., and K.P. Shine (1995). The effect of anthropogenic sulfate and soot aerosol on the clear sky planetary radiation budget. Geophys. Res. Lett., 22(5), 603–606.

Haywood, J.M., and O. Boucher (2000). Estimates of the direct and indirect radiative forcing due to tropospheric aerosols: A review. Rev. Geophys., 38, 513–543.

Hegg D.A., R.J. Ferek and P.V. Hobbs (1993). Aerosol size distribution in the cloudy atmospheric boundary layer of the North Atlantic ocean. J. Geophys. Res., 98, 8841 - 8846.

Heintzenberg, H. Müller, H. Quenzel and E. Thomalla (1981). Information content of optical data with respect to aerosol properties: Numerical studies with a randomized

minimization-search-technique in inversion algorithm, App. Opt (20):1308-1315.

Herman, B.M., S.R. Browning and J.A. Reagan (1971). Determination of aerosol size distributions from lidar measurements, J. Atmos. Sci. Vol. 28, pp. 763-771.

Holben, B.N., T.F. Eck, I. Slutsker, D. Tanre, J.P. Buis, A. Setzer, E. Vermote,J.A. Reagan, Y.J. Kaufman, T. Nakajima, F. Lavenu, I. Jankowiak, A. Smirnov (1998). AERONET-A federated instrument network and data archive for aerosol characterization. Remote Sensing of Environment 66 (1), 1–16

Holben, B.N., D. Tanré, A. Smirnov, T.F. Eck, I. Slutsker, N. Abuhassan, W.W.Newcomb, J. Schafer, B. Chatenet, F. Lavanue, Y.J. Kaufman, J. Vande-Castle, A. Setzer, B. Markham, D. Clark, R. Frouin, R. Halthore, A. Karkieli, N.T. o'Neill, C. Pietras, R.T. Pinker, K. Voss and G. Zobordi (2001). An emerging ground-based aerosol climatology: Aerosol optical depth from AERONET, J. Geophys. Res. 106(D11):12067-12098.

Holland, J. H. (1962). Outline for a logical theory of adaptive systems. Journal of the Association of Computer Machinery. Vol. 9(3), pp. 297-314.

Horvath, H. (1998), Influence of atmospheric aerosols upon the global radiation balance. Atmospheric particles. R.M. Harrison and R. Van Grieken Eds., John Wiley & Sons Ltd.

Houghton, J.T., Y. Ding, D.J. Griggs, M. Noguer, P.J. van der Linden, X. Dai, K. Maskell, and C.A. Johnson, Eds. (2001). Climate Change 2001: The Scientific Basis. Cambridge University Press.

Howard, D. and M. Beale (2000). Neural Network Toolbox user's guide (version 4). The Mathworks Inc.

Iqbal, M. (1983). An introduction to solar radiation. Academic Press Canada.

Johnson, R.W., W.S. Hering, J.I. Gordon, B.W. Fitch and J.E. Shields (1980). Preliminary Analysis and Modeling Based Upon Project OPAQUE Profile and Surface Data. University of California, San Diego, Scripps Institution of Oceanography, Visibility Laboratory, SIO Ref. 80-5, AFGL-TR-0285, NTIS No. ADB-052-1721

Johnson, R.W., W.S. Hering and J.E. Shields (1989). Automated Visibility and Cloud Cover Measurements with a Solid State Imaging System. University of California, San Diego, Scripps Institution of Oceanography, Marine Physical Laboratory, SIO 89-7, GL-TR-89-0061, NTIS No. ADA216906

Junge, C.E. (1955). The size distribution and aging of natural aerosols as determined from electrical and optical data on the atmosphere, J. Meteor. Vol. 12, pp. 13-25.

Kasten, F. (1966). A new table and approximate formula for relative optical mass. Arch. Meteorol. Geophys. Bioclimatol. B14, 206-223.

Kasten, F and A.T. Young (1989). Revised optica air-mass tables and approximation formula, Applied Optics 28(22) pp. 4735-4738.

Kaufman, Y.J. (1993). Aerosol optical thickness and atmospheric path radiance, Journal of Geophysical Research-Atmospheres 98 (D2), 2677–2692.

Khanna, T. (1990). Foundations of neural networks. Addison-Wesley. New York

King, M.D., D.M. Byrne, B.M. Herman and J.A. Reagan (1978). Aerosol size distributions obtained by inversion of spectral optical depth measurements, J. Atmos Sci. 35 2.153-2.167.

Kokhanovsky, A.A. (2006). Cloud optics. Springer-Praxis, Chichester, UK.

Kondratyev, K.Y. (1999). Climatic effects of aerosols and clouds, Eds. Praxis. Pub. Chichester, UK.

Liebelt, P.B. (1967). An introduction to estimation theory, Addison-Wesley.

Lillesand, T.M. and R.W. Kiefer (1994). Remote Sensing and Image Interpretation (3rd edition), John Wiley and Sons.

Liou, K.N. (1992). Radiation and Cloud Processes in the Atmosphere. Oxford University Press.

Lippman, R. (1987). An introduction to computing with neural nets, IEEE ASSP Magazine. Vol. 2, 4-22.

Lohmann, U., and J. Feichter (2005) Global indirect aerosol effects: A review. Atmos. Chem. Phys., 5, 715–737.

Long, C.N. and J.J. De Luisi (1998). Development of an Automated Hemispheric Sky Imager for Cloud Fraction Retrievals, Proc. 10th Symp. on Meteorological Observations and Instrumentation, Phoenix Arizona, Jan.11-16,1998, pp.171-174

Long C.N., J.M. Sabburg, J. Calbó and D. Pagès (2006), Retrieving Cloud Characteristics from Ground-Based Daytime Color All-Sky Images. J. Atmos. Oce. Tech. vol. 23, pp. 633-652.

Lyamani, H, F.J. Olmo and L. Alados-Arboledas (2005). Saharan dust outbreak over southeastern Spain as detected by sun photometer, Atmospheric environment, Vol. 39(38) pp. 7276-7284.

Lyamani, H., F.J. Olmo, A. Alcántara and L. Alados-Arboledas (2006). Atmospheric aerosols during the 2003 heat wave in

southeastern Spain I: spectral optical depth, Atmos. Environ. 40, 6453–6464.

Martinez-Lozano J.A., M.P. Utrillas, R. Tena and V.E. Cachorro (1999). The parameterization of the atmospheric optical depth using the Angström power law, Sol. Energy 63, 303-311.

McKenzie, R.L., K.J. Paulin, G.E. Bodeker, J.B. Liley, and A.P. Sturman (1998), Clooud cover measured by satellite and from the ground: relationship to UV radiation at the surface. Int. J. Rem. Sens. Vol 19(15), pp. 2969-2985.

Michalewicz, Z. (1992). Genetic Algorithms + data structures = Evolution Programs. Srpinger-Verlag. Berlin.

Mie, G. (1908). Beiträge zur Optik trüber Medien, speziell kolloidaler Metallösungen. Annalen der Physik, 25(3):377–445.

Morys, M., F.M. Mims, S. Hagerup, S.E. Anderson, A. Baker, J. Kia and T. Walkup (2001). Design, calibration and performance of MICROTOPS II handheld ozone monitor and sun photometer. J. Geophys. Res., 106(D13):14.573-14.582

Olmo, F.J, A. Quirantes, A. Alcantara, H. Lyamani and L. Alados-Arboledas (2006). Preliminary results of a non-spherical aerosol method for the retrieval of the atmospheric aerosol optical properties, Journal of quantitative spectroscopy and radiative transfer, Vol 100(1-3) pp. 305-314

Olmo, F.J., A. Quirantes, V. Lara, H. Lyamani and L. Alados-Arboledas (2008). Aerosol optical properties assessed by an inversion method using the solar principal plane for non-spherical particles, Journal of quantitative spectroscopy and radiative transfer, Vol 109(8) pp.1504-1516

Parisi, A.V., J. Sabburg and M.G. Kimlin (2004). Scattered and filteres solar UV measurements, Kluwer Academic Publishers.

Park, J. and J.W. Sandberg (1991). Universal approximation using radial basis functions network. Neural Computation, 3, 246-257.

Penner, J.E., et al. (2001). Aerosols, their direct and indirect effects. In: Climate Change 2001: The Scientific Basis. Contribution of Working Group I to the Third Assessment Report of the Intergovernmental Panel on Climate Change [Houghton, J.T., et al. (eds.)]. Cambridge University Press, Cambridge, United Kingdom and New York, NY, USA, pp. 289–348.

Phillips D.L. (1962). A technique for the numerical solution of certain integral equations of the first kind, J. Assoc. Compt. 9, 84-97.

Platt, C.M., S.A. Young, A.I. Carswell, S.R. Pal, M.P. McCormick, D.M. Winker, M. DelGuasta, L. Stefanutti, W.L. Eberhard, M. Hardesty, P.H. Flamant, R. Valentin, B. Forgan, G.G. Gimmestad, H. Jager, S.S. Khmelevtsov, I. Kolev, B. Kaprieolev, D-r. Lu, K. Sassen, V.S. Shamanaev, O. Uchino,

Y. Mizuno, U. Wandinger, C. Weitkamp, A. Ansmann and C. Wooldridge (1994), The experimental cloud Lidar pilot study (ECLIPS) for cloud-radiation research. Bull. Am. Met. Soc. Vol 75(9), pp. 1635-1654

Poggio, T. and F. Girosi (1990). Networks for approximation and learning. Proc. IEEE 78 (9), 1481-1497.

Quenzel, H. (1970). Determination of size distribution of atmospheric aerosol particles from spectral solar radiation measurements, J. geophys. Res. Vol. 75, pp. 2915-2921.

Ramaswamy, V., et al. (2001). Radiative forcing of climate change. In: Climate Change 2001: The Scientific Basis. Contribution of Working Group I to the Third Assessment Report of the Intergovernmental Panel on Climate Change [Houghton, J.T., et al. (eds.)]. Cambridge University Press, Cambridge, United Kingdom and New York, NY, USA, pp. 349–416.

Riedmiller, M. and H. Braun (1993). A direct adaptive method for faster backpropagation learning: The RPROP algorithm, Proc of the IEEE Int. Conf. on Neural Networks, San Francisco.

Rogers, R.R. and M. K. Yau (1989). A Short Course in Cloud Physics, Pergamon.

Rollin, E.M (2000). An introduction to the use of sun-photometery for the atmospheric correction of airborne sensor data. Activities of the NERC equipment pool for field spectroscopy (EPFS) in support of the NERC Airborne remote Sensing

Facility, British geological survey, University of Southhampton.

Romanov, P. (1994). Cloud parameters and precipitation intensity analysis using AVHRR images classification scheme, 7th Australasian Remote Sensing Conference, Melbourne, Australia, pp. 109-115.

Rosenblatt, B. (1961). Principles of neurodynamics: Perceptrons and the theory of brain. Mechanisms. Spartan Press. Washington DC.

Rumerlhart, D.E., G.E. Hilton and R.J. Williams (1986). Learning internal representations by errors propagation. In pararell distributed processing: Exploitations in the microstructure of cognitron. Vol. 1. D.E. Rumelhart and J.L. MacClelland, Cap. 8. MIT Press.

Sabburg, J. (2000) Quantification of Cloud Around The Sun And Its Correlation With Global UV Measurement. PhD Thesis, Queensland University

Sabburg, J., and J. Wong (2000). The effect of clouds on enhancing UVB irradiance at the Earth's surface: A one year study, Geophys. Res. Lett., 27(20), 3337–3340.

Sabburg, J. M., A.V. Parisi, and M.G. Kimlin (2003). Enhanced spectral UV irradiance: A 1 year preliminary study, Atmos. Res., 66(4), 261–272.

Sabburg, J. M. and C.N. Long (2004). Improved sky imaging for studies of enhanced UV irradiance. Atmos. Chem. Phys. Discuss., 4, 6213-6238, 2004. EGU

Sánchez, C., F.J. Olmo and L. Alados-Arboledas (1998). Determination of aerosol optical thickness from measurements of spectral sky radiance. Journal of Aerosol Science 29 (10), 1199–1211.

Schafer, J.S., V.K. Saxena and J.J. De Luisi (1996). Observed influence of clouds on ultraviolet-B radiation. Geophysical Res. Letters, vol.23(19), pp.2625-2628

Schmid B., C. Mätzler, A. Heimo and N. Kämpfer (1997). Retrieval of optical depth and particle size distribution of tropospheric and stratospheric aerosols by means of sun photometry, IEEE Transactions on Geoscience and Remote Sensing 35(1): 172-182.

Seinfeld, J.H. and S.N. Pandis, (1998). Atmospheric Chemistry and Physics: From air pollution to climate change. John Wiley & Sons, Inc.

Shaw, G.E., J.A. Reagan and B.M. Herman (1973). Investigations of atmospheric extinction using direct solar radiation measurements made with a multiple wavelength radiometer, J. Appl. Meteor. Vol. 12, pp. 374-380.

Shaw, G.E. (1983). Sun photometry, Amer. Meteor. Soc. 64(1):4-10.

Shields, J.E., R.W. Johnson and T.L. Koehler (1993). Automated whole sky imaging systems for cloud field assessment. In: Proceedings of the Fourth Symposium on Global Change Studies. American Meteorological Society, Boston, MA

Shields, J.E., R.W. Johnson, M.E. Karr and J.L. Wertz (1998). Automated Day/Night Whole Sky Imager for field assessment of cloud cover distributions and radiance distributions. In: Proceedings of the 10th Symposium on Meteorological Observations and Instrumentations, Phoenix, AZ. American Meteorological Society, Boston, MA

Shifrin, K.S. (1995). Simple relationships for the Ångström parameter of disperse systems. Applied Optics 34 (21), 4480–4485.

Smirnov, A., B.N. Holben, T.F. Eck, O. Dubovik and I. Slutsker (2001). Cloud-screening and quality control algorithms for the AERONET database. Remote Sensing of Environment 73 (3), 337–349

Souza-Echer, M.P., E.B. Pereira, L.S. Bins.and M.A. R. Andrade (2006). A simple method for the assessment of the cloud cover state in high-latitude regions by a ground based digital camera, J. Atmos. Ocean. Technol. 23, 437–447.

Tegen, I., A.A. Lacis, and I. Fung (1996). The influence on climate forcing of mineral aerosols from disturbed soils. Nature, 380, 419–421.

Tou, J.T. and R.C. Gonzalez (1974). Pattern Recognition. Addison-Wesley.

Twomey S.A. (1963). On the numerical solution of Fredholm integral equations of the first kind by the inversion of the linear system produced by cuadrature, J. Assoc. Comut. 10, 97-101.

Twomey, S.A. (1977). The influence of pollution on the shortwave albedo of clouds. J. Atmos. Sci., 34, 1149–1152.

U.S. Standard Atmosphere (1976). U.S. Government Printing Office, Washington, D.C.

van de Hulst, H.C. (1957). Light scattering by small particles. Wiley.

Vergaz, R. (2001). Propiedades ópticas de los aerosols atmosféricos. Caracterización del área del Golfo de Cádiz. Tesis doctoral, Universidad de Valladolid.

Volz, F.E. (1974). Economical multispectral sun photometer for measurements of aerosol extinction from 0.44 □m to 1.6 □m and precipitable water, Appl. Opt. 13, 1732

Wang, P.H., M.P. McCormick, T.J. Swissler, M.T. Osborn, W.H. Fuller and G.K. Yue (1989). Inferrence of stratospheric aerosol composition and size distribution from SAGE II satellite measurements, J. Geophys. Res Lett. 94, 8435-8446.

Warren, S.G., C.J. Hahn, J. London, R.M. Chervin and R.L. Jenne (1986). Global distribution of total cloud cover and cloud

type amounts over land. NCAR Tech. Note, NCAR/TN-273+STR.

Warren, S.G., C.J. Hahn, J. London, R.M. Chervin and R.L. Jenne (1988). Global distribution of total cloud cover and cloud type amounts over the ocean. NCAR Tech. Note, NCAR/TN-317+STR.

Whitby, K.T and B. Cantrell (1976). Fine particles, in International Conference on Environmental Sensing and Assessment, Las Vegas, NV, IEEE.

Whitby, K.T. (1978). The physical characteristics of surfur aerosols. Atmos. Environ 12, 135-159.

Whitby, K.T. (1980). Aerosol formation in the urban plumes, Ann. N. Y. Acad. Sci 338, 258-275.

WMO (1983). Guide to Meteorological Practice, Publication No. 168, World Meteorological Organization.

WMO (1995). Manual on Codes, Publication No. 306, World Meteorological Organization.

Wooldridge, C. (1993). The development and evaluation of a digital whole-sky cloud monitoring system, PhD Thesis, Macquarie University

Wooldridge, C. and S. Hayman (1994). Cloud cover assessment grids for whole-sky images. Lighting Res. Technology, 26(1), pp.9-12

Yamato, G and M. Tanaka (1969). Determination of aerosol size distribution from spectral attenuation measurements, Appl. Opt. Vol. 8, pp. 447-453.

Yee, P.V. and S. Haykin (2001). Regularized Radial Basis Function Networks: Theory and Applications. Wiley, New York.

Related publications by the author

Papers in journals

P. Serrano-Ortiz, F. Domingo, **A. Cazorla**, A. Were, S. Cuezva, L. Villagarcía, L. Alados-Arboledas, A.S. Kowalski, *"Interannual CO2 balance of a sparse Mediterranean shrubland on a carbonaceous substrate,"* Journal of Geophysical Research (Biogeoscience) 114, G04015, doi:10.1029/2009JG000983 (2009).

A. Cazorla, J.E. Shields, M.E. Karr, A. Burden, F.J. Olmo and L. Alados-Arboledas, *"Determination of aerosol optical properties by a calibrated sky imager,"* Atmospheric Chemistry and Physics, 9 (17), 6417-6427 (2009).

A. Cazorla, J.E. Shields, M.E. Karr, A. Burden, F.J. Olmo and L. Alados-Arboledas, *"Calibrated sky imager for aerosol optical properties determination,"* Atmospheric Chemistry and Physics Discussion, 8 (6), 19989-20018 (2008).

F.J. Olmo, **A. Cazorla**, L. Alados-Arboledas, M.A. López-Álvarez, J. Hernández-Andrés and J.Romero, *"Retrieval of the optical depth by an all-sky CCD camera,"* Applied Optics, 47 (24), H182-H189 (2008).

M. A. López-Álvarez, J. Hernández-Andrés, J. Romero, F. J. Olmo, **A. Cazorla** and L. Alados-Arboledas, *"Using a trichromatic*

CCD camera for spectral skylight estimation," Applied Optics, 47 (24), H31-H38 (2008).

A. Cazorla, F.J. Olmo and L. Alados-Arboledas, *"Using a sky imager for aerosol characterization,"* Atmospheric Environment, 42 (11), 2739-2745 (2008).

A. Cazorla, F.J. Olmo, and L. Alados-Arboledas, *"Development of a sky imager for cloud cover assessment,"* Journal of the Optical Society of America A 25, 29-39 (2008).

Conference Proceedings

A. Cazorla, F.J. Olmo and L. Alados-Arboledas, *"Aerosol characterization with a calibrated sky camera,"* Tercera renunión de Ciencia y Tecnología de Aerosoles (RECTA) (Bilbao, Spain. June 2009).

A. Cazorla, R. Wagener, J.E. Shields, F.J. Olmo and L. Alados-Arboledas, *"Aerosol Characterization with a Calibrated CCD Sky Imager,"* Science Team Meeting (ARM) (Louisville (KY), USA. April 2009).

A. Cazorla, J.E. Shields, M.E. Karr, A. Burden, F.J. Olmo and L. Alados-Arboledas, *"Ground-based sky imagery for aerosol optical depth estimation,"* European Aerosol Conference (Thessaloniki, Greece. August 2008).

A. Cazorla, J.E. Shields, M.E. Karr, A. Burden, F.J. Olmo and L. Alados-Arboledas, *"Setting up a calibrated sky imager for*

aerosol optical properties estimation," Segunda renunión de Ciencia y Tecnología de Aerosoles (RECTA) (Torremolinos, Spain. June 2008).

L. Alados-Arboledas, J.L. Guerrero-Rascado, H. Lyamani, J.E.Gil, **A. Cazorla** and F.J. Olmo, *"Detection of May 2006 Saharan dust outbreak over Granada, Spain, by combination of active and passive remote sensing,"* IEEE International Geoscience and Remote Sensing Symposium IGARSS 2007, Sensing and Understanding Our Planet (Barcelona, Spain. July 2007).

F.J. Olmo, **A. Cazorla** and L. Alados-Arboledas, *Development of a sky imager for cloud cover and aerosol characterizacion,"* Primera renunión de Ciencia y tecnología de aerosoles (RECTA) (Madrid, Spain. July 2007).

L. Alados-Arboledas, J.L. Guerrero-Rascado, H. Lyamani, I. Foyo-Moreno, I. Alados, J.E. Gil, **A. Cazorla**, F. Navas-Guzmán and F.J. Olmo, *"Detection of the may 2006 saharan dust outbreak over Granada, Spain, by combination of active and pasive remote sensing,"* Primera renunión de Ciencia y tecnología de aerosoles (RECTA) (Madrid, Spain. July 2007).

M.A. López-Álvarez, J. Hernández-Andrés, J. Romero, F.J. Olmo, **A. Cazorla** and L. Alados-Arboledas, *"Taking advantage of a trichromatic CCD digital camera for spectral estimation,"* 9th International Meeting on Light and Color in Nature (Bozeman, MT, USA. June 2007).

F.J. Olmo, **A. Cazorla**, L. Alados-Arboledas, M.A. López-Álvarez, J. Hernández-Andrés and J. Romero, *"Using all-sky imager to obtain aerosol and cloud optical properties,"* 9th International Meeting on Light and Color in Nature (Bozeman, MO, USA. June 2007).

A. Cazorla, F.J. Olmo and L. Alados-Arboledas, *"Development of an All-Sky Imager for cloud classification,"* Proceeding of the 2nd International Symposium on Recent Advances in Quantitative Remote Sensing (Torrent, Valencia, Spain. September 2006.

L. Alados-Arboledas, J.L. Guerrero-Rascado, H. Lyamani, J.E. Gil, B. Ruiz, **A. Cazorla** and F.J. Olmo, *"Active and passive remote sensing of atmospheric aerosol over Granada, Spain,"* 7th International Aerosol Conference (St. Paul, MN, USA. September 2006).

A. Cazorla, F.J. Olmo and L. Alados-Arboledas, *"Using a sky imager for aerosol characterization,"* Procceding of the Conference on Visibility, Aerosols, and Atmospheric Optics (Vienna, Austria. September 2006).

A. Cazorla, F.J. Olmo and A. Alados-Arboledas, *"Estimación de la cubierta nubosa en imagines de cielo mediante el algoritmo KNN (Estimation of the cloud cover on sky images by means of the KNN algorithm),"* Remote Sensing. Advances on Earth Observation. Vol. 1, pp. 335-338 (Tenerife, Spain. September 2005).

A. Cazorla, F.J. Olmo and L. Alados-Arboledas, *"Determinación de la cubierta nubosa en imagines de cielo mediante un perceptrón multicapa (Determination of the cloud cover on sky images by means of a multilayer perceptron),"* Proceedings of SICO2005 (IEEE Computational Intelligence Society, SC) Vol. 17, pp. 27-30 (Granada, Spain. September 2005).

C. Plata, E. Valero, **A. Cazorla**, F.J. Olmo, L. Alados-Arboledas and J.L. Nieves, *"Identification of clouds and sky in digital images using a principal component analysis,"* AIC Colour '05 – 10th Congress of the International Colour Association. pp. 1689-1692 (Granada, Spain. May 2005).

J.E. Gil, **A. Cazorla**, F.J. Olmo and L. Alados-Arboledas, *"Experimental set up to study the cloud radiative effects on UVB at Granada (Spain),"* European Geoscience Union. General Assembly. Vol. I, pp. EGU05-A-00320; AS1.08.1WE2P-0059 (Vienna, Austria. April 2005).